Thesis Report

High Accuracy GNSS-based on-board Orbit Determination and Prediction Methods for Tracking Software in Satellite Laser Communications

Master Thesis MSc. Aerospace Engineering

Kipras Paliušis

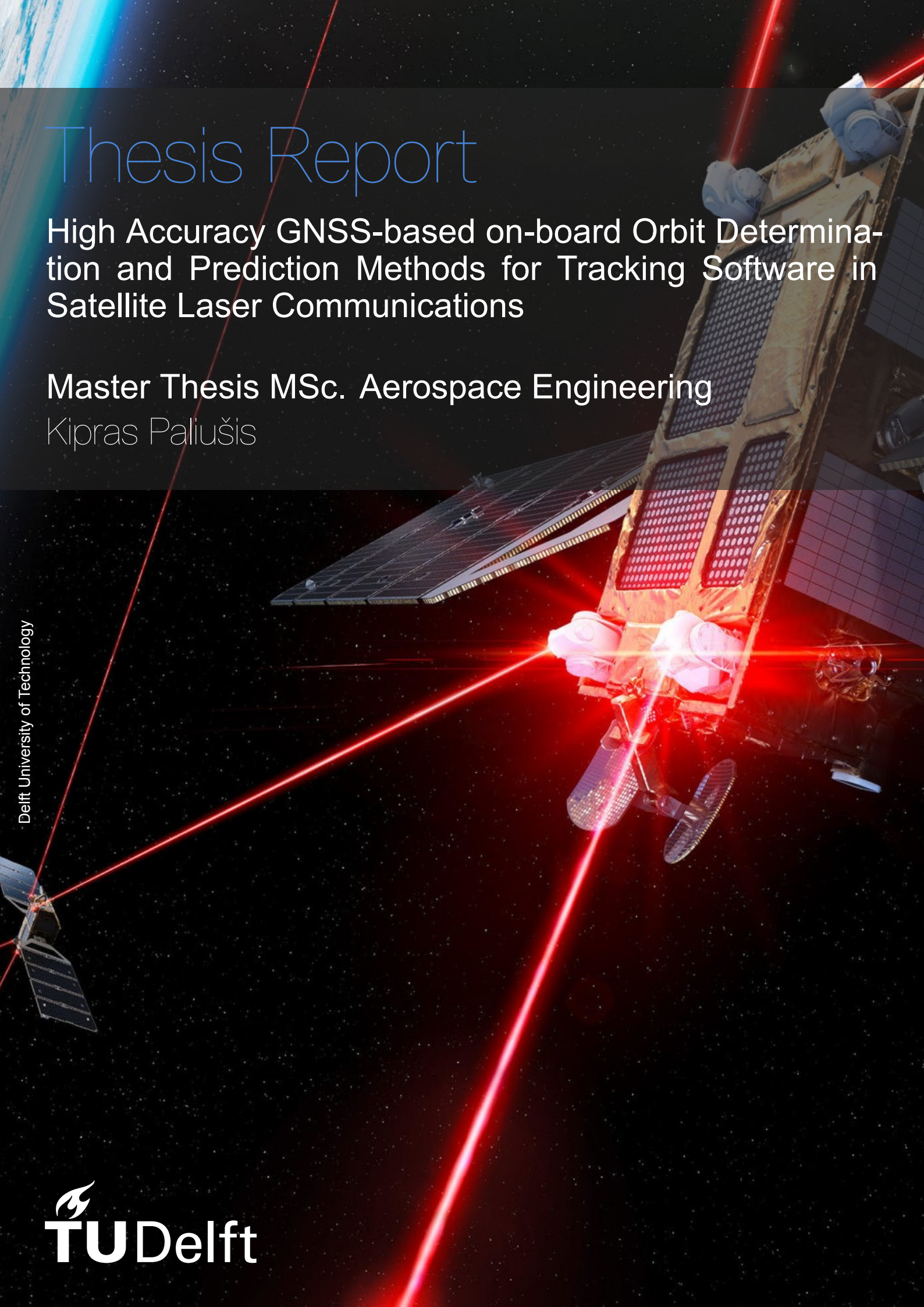

Delft University of Technology

TU Delft

Thesis Report

High Accuracy GNSS-based on-board Orbit Determination and Prediction Methods for Tracking Software in Satellite Laser Communications

by

Kipras Paliušis

to obtain the degree of Master of Science
at the Delft University of Technology,
to be defended publicly on Wednesday, March 22, 2023 at 9:30 AM.

Student number:	4456521	
Project duration:	May, 2022 – March, 2023	
Project Supervisors:	Dr. Bayajid Khan,	Mynaric, supervisor
	Dr. Jian Guo,	TU Delft, supervisor
Thesis committee:	Dr. Bayajid Khan,	Responsible Thesis Supervisor, Mynaric
	Dr. Jian Guo,	Chair, TU Delft
	Ir. Ron Noomen,	Examiner, TU Delft
	Dr. Sandra Verhagen,	Examiner, TU Delft

This thesis is confidential and cannot be made public until 22 March 2025

Cover: Laser Inter-satellite Links [23]

The thesis will be available at `http://repository.tudelft.nl/` after the embargo period.

TU Delft

Acknowledgements

Many thanks are in order. A combined thanks to all the great teachers I had in my early years back in Lithuania, as well as the lecturers, mentors and peers in Delft.

A special thanks goes to multiple people at Mynaric. Thanks to Luis Martin Navajas for opening the company door for me back in June of 2020 and support in the first months. Thanks to Fletcher Tollefson, for providing me a bridge from my initial internship to the work-student and thesis positions. Thanks to Mauro Calabria, for providing the tough support and push that I needed, as well as the opportunity to continue at Mynraic. A big big thanks to my daily supervisor Bayajid Khan for the huge amount of time and effort that he provided me throughout the past year. A final thanks to the upper management at Mynaric, and my TU Delft supervisor Jian Guo for enabling me to work on this graduation project.

Big thanks also go out to my fellow students-peers-closest friends: Yvonne, Miha, Lars and other Lars. I'm extremely glad that TU Delft has connected us. We have shared many great hikes, evenings at the beach, pineapples, dinners and laughs. I am proud of the friendships we have built and will continue to maintain for as long as we live. I look forward to seeing you all.

Another huge thanks to my partner Hana, who has been my biggest supporter during the last stages of my studies. You have been helpful in every way possible through the ups and downs of this thesis and I am extremely appreciative of that. I love you.

Final thanks go out to my family. Ačiū Mama, Tėti, Sese. Šiek tiek užtrukau, bet pagaliau baigiau!

Kipras Paliušis
Wessling, April-2023

Summary

Project Background Demands for bandwidth are ever increasing and free-space optical technology is expected to meet these needs [41]. Compared to radio frequency, laser communication is safer, does not occupy regulated frequency bands, requires less power and offers much higher data-rates. Satellite constellations are expected to provide global, high-speed, secure communications [41], but Laser Inter-satellite Links (LISL) remain difficult due to narrow beam divergence angles and fast relative velocities. For the Pointing, Tracking and Acquisition system to acquire a LISL within 1-2 minutes, it requires initial pointing knowledge, which is challenging to precisely determine on-board (OB) the satellite [20].

Mynaric develops Laser Communication Terminals (LCT) and are focused on aerospace applications. Mynaric was founded in 2009, as a spin-off of DLR's Institute of Navigation and Communication, which has worked on LCT's for 20 years. Separate branches of terminals include LCT's for ground communications, LCT's for aviation and for the space environment. Mynaric's LCT's for space applications are called CONDOR terminals and are specialized for LISL.

The project aims to analyse, develop, and evaluate OB GNSS-based orbit determination (OD) and prediction algorithms for Low and Medium Earth Orbit (LEO, MEO) satellite laser communication. To meet OB limitations and laser communication accuracy needs, the algorithms' computational load and contribution to the pointing uncertainty cone will be quantified. A baseline of 0.5 mrad PE contribution is set as a conservative threshold to evaluate whether the Orbit Prediction (OP) quality is sufficient.

Research Scope This research will be focused on improving the host and target satellite's pointing knowledge and quantifying its impact on the pointing UC for LISL in a LEO/MEO constellation. This will be done with 3 focuses in mind.

1. Analyzing the LISL variables in a LEO/MEO Satellite constellation and quantifying the expected available communication windows for terminals matching CONDOR Mk2 and Mk3 viewing limitations.
2. Implementing and testing Novel Kalman Filters (KF), improving the Preprocessing Extended Kalman Filter, quantifying expectations for GNSS-OD performance in the LEO/MEO Satellite Constellation.
3. Evaluating performance of GNSS-based OD-OP algorithms in various link case scenarios and testing their applicability for Satellite Laser communication.

Simulated LEO/MEO Constellation The orbital scenarios will be dictated by specific LISL cases. These were determined by simulating a LEO-MEO satellite constellation in TUDAT and defining several link cases, representative of increasingly challenging link dynamics. The constellation parameters are based on previous link analyses and expected use cases- to provide global communication capabilities, include MEO satellites and cover the most populated Earth regions.

Table 1: Orbital parameters of the circular Laser communication Satellite Constellation.

Constellation	h [km]	i [deg]	Nr. Planes [-]	Sat/Plane [-]	Nr. Total sat. [-]
LEO near-polar	1000	89	13	14	182
LEO med. Incl.	1000	53	13	14	182
MEO	13892	0	1	5	5

Link Availability Implementing the pointing limitations and slant range limits of CONDOR Mk2 as LCT1 and Mk3 as LCT2, it was determined how many links can potentially be established by the terminals of each satellite. Over 2 hours, on a LEO Polar satellite, LCT1 would have a maximum of 227 links with LEO Polar satellites (mostly in the 10-15 minute region), 240 with LEO Inclined (mostly 5-10

minute long) and 9 with MEO Satellites (10-15 minute or 60 minute links). In the same orbital conditions, LCT2 has 294 links available to LEO Polar satellites (mostly 10-20 minute), 327 to LEO Inclined (mostly 10-25 minute) and 9 to MEO satellites (40+ minutes). This showed that the wider angular coverage of LCT2 enables both more and longer links from a LEO Polar Host.

The same analysis on a LEO Inclined and a MEO host was made for both terminals. Using LCT1, it showed 154 links to LEO Inclined (1-15 minutes), 233 to LEO Polar (mostly 1-15 minute long) and 8 to MEO satellites (30- minutes). More links were again seen for LCT2 - 227 to LEO Inclined, 327 to LEO Polar and 9 to MEO links, with 5 minute longer link windows than LCT1. For MEO, LCT1 did not cover the required pointing angles and did not have any available link windows. In contrast, LCT2 indicates over 700 possible links with LEO Inclined and Polar hosts over an 8 hour window with mostly long windows (60+ minutes), where Earth occultation was the main limitation. 2 links were detected to MEO targets, namely the nearest leader and follower in the MEO plane.

Table 2: Overview of the 6 selected link cases to be used to benchmark the OD-OP algorithms.

Link nr.	Length [min]	Host	Target	Max AE Rate [deg/s]	Max. Link Dist. [km]	Min. Link Dist. [km]
1	60	MEO	MEO	0	24000	24000
2	60	MEO	LEO I	2	23000	13000
3	60	LEO P	MEO	0.3	22500	13000
4	60	LEO P	LEO P	0	3500	3500
5	20	LEO P	LEO I	4	7000	50
6	60	LEO I	LEO I	0.4	3300	100

As shown above, six link cases were selected for the subsequent algorithm implementation. 3 were chosen to cover links with MEO satellites and 3 between satellites in LEO. MEO links to each shell were chosen- a co-planar link to a MEO follower representing the easiest linking conditions in terms of PE due to prediction errors and slightly more challenging links to LEO Inclined and Polar satellites flying directly under the MEO satellite. The LEO link cases were also chosen to vary the link conditions difficulty. The easiest LEO link case was the co-planar LEO Polar satellite with constant distance and pointing angles. The 5th LEO Polar-Inclined case was among the most difficult links, as the satellites fly in opposite directions and have an extremely close approach. The sixth case included a cross-plane link of LEO Inclined satellites, which also represented difficult link conditions due to high angular rates, varying link distance and cross-track link direction.

4 Prediction window lengths were selected to evaluate the OD-OP algorithms. First, a 100 second window for the minimum link acquisition time requirement. The remaining windows were 10, 30 and 60 minutes, covering most of LEO and MEO cases, respectively.

GNSS-OD Performance 4 KF formulations were implemented and tested with the single-frequency L1 pseudorange measurements of GRACE-FO, CHAMP and Jason-3 satellites. Using elevation-based measurements selection, the filters showed varying performances. The novel Single-propagation Unscented Kalman and Preprocessing Extended Kalman Filters (SPUKF and PEKF, respectively) performed similarly worse than the basic Extended Kalman Filter (EKF) and the Unscented Kalman Filter (UKF). Using CHAMP data, the EKF indicated 3D RMS OD errors around 40 m and the remaining filters around 100 m. For Grace-FO data, EKF performed at around a 10 m accuracy, while the remaining filters had accuracies below 25 m. Using Jason-3 data, all 4 filters performed at a similar 50 m accuracy. Although this showed that the Novel SPUKF and PEKF perform competitively with the standard EKF, their added complexity and computational load indicate that EKF is the recommended choice.

An Improved PEKF was implemented, which utilized a higher efficiency Newton-Raphson Predictor-Corrector (NRPC), leading to the NRPC-PEKF. The original PEKF used Newton-Raphson method in the Preprocessing block. After comparison, the NRM-PEKF and NRPC-PEKF performed identically in terms of accuracy. Additionally, it was found the the NRPC provided the same solutions as the original NRM, while in rare occasions requiring more computations. It is also more complex and therefore, it was concluded that the NRPC-PEKF shows no benefits over the NRM-PEKF in GNSS-OD.

GNSS-OD-OP Analysis 3 OD-OP algorithms were defined to be evaluated in each link case with different initial OD errors and OP methods. These were 1) Kinematic Algorithm (KA)- using only kinematic methods for OD and quadratic extrapolation for OP; 2) Basic-Dynamic Algorithm (BDA), using pseudorange-based OD methods and basic J2 propagation, and 3) Complex-Dynamic Algorithm (CDA), using carrier-phase OD methods and complex dynamic orbit propagation. The Initial OD errors for each algorithm are shown below. For KA and BDA, the observed errors using Kinematic-OD and an EKF with Jason-3 satellite data was chosen. The CDA initial errors were selected from literature for the PROBA-2 satellite's flight experience.

Table 3: State Errors for each Orbit Determination algorithm, showing the mean and standard deviation.

OD Algorithm	**Kinematic SPP**	**PR-based EKF**	**CP-based EKF**
Radial Pos. Error [m]	11.0+/-46.0	6.5+/-33.6	0.5+/-0.5
Along-track Pos. Error [m]	-5.9+/-27.0	-4.1+/-28.2	0.3+/-1.2
Cross-track Pos. Error [m]	0.7+/-32.0	-2.2+/-25.0	0.0+/-0.3
Radial Vel. Error [m/s]	0.0040+/-5.80	0.0230+/-2.51	-0.0030+/-0.0009
Along-track Vel. Error [m/s]	0.2000+/-6.90	0.0130+/-2.86	-0.0001+/-0.0006
Cross-track Vel. Error [m/s]	-0.0004+/-12.80	0.0030+/-2.49	0.0001+/-0.0004

Short predictions for all 3 algorithms were done with predictions starting throughout different times of the link window and evaluating the PE contribution after 100 s. The CDA showed minimum PE contributions, peaking at 5 μrad for the LEO Polar-LEO Inclined link. The KA and BDA performed similarly, contributing below 100 μrad for the 3 MEO link cases. For LEO link cases, supported the LEO Polar link case with contributions below 200 μrad. The LEO Polar- Inclined and cross-plane LEO Inclined link PE contributions exceeded the 0.5 mrad threshold whenever the link distance was below 3500 km. At larger link distances, the PE contributions were 100-200 μrad.

Results for longer predictions are shown below. Again the CDA's impact on PE was found to be well below the threshold of 0.5 mrad for link cases and windows. The BDA now outperformed the KA, as the extrapolation-based predictions diverge severely for longer windows. For MEO cases, the KA could still support a 10 minute window for Co-planar MEO satellites. The BDA could support all MEO cases up to 10 minutes. Neither of the two could support any LEO link cases, although the BDA's impact was at least 2 factors smaller than the KA's at 10 minutes.

Table 4: 99.7th percentile of the maximum PE [μrad] for the 10/30/60 min. predictions.

t pred.	**Copl. MEO - MEO**			**Inter-orb. MEO - LEO I**			**Inter-orb. LEO P - MEO**		
[min]	**KA**	**BDA**	**CDA**	**KA**	**BDA**	**CDA**	**KA**	**BDA**	**CDA**
10	400	300	0.2	7500	400	0.2	5400	400	0.2
30	9700	900	0.4	148100	2000	1.1	400500	1900	1.1
60	64000	1800	0.9	2153500	2500	1.2	1457400	3700	1.2
t pred.	**Copl. LEO P - LEO P**			**Inter-shell LEO P - LEO I**			**Intra-shell LEO I - LEO I**		
[min]	**KA**	**BDA**	**CDA**	**KA**	**BDA**	**CDA**	**KA**	**BDA**	**CDA**
10	31600	2200	1.2	1590800	43300	21.3	5100	2800	3
30	154200	7800	3.1	1590800	43300	21.3	24100	15500	6.3
60	1038300	14500	4.6	-	-	-	2330800	127900	39.9

It was therefore concluded that with the considered OD performance, CDA can provide accurate coarse pointing knowledge, while the KA and BDA can perform well in short-term predictions.

For future research, it was recommended to analyze the impact of different numerical integrators, state representations and the impact of simplified rotation/ephemeris models. Also, as only pseudorange-based models were implemented during this research, it is recommended to also implement a carrier-phase based OD algorithm to test whether its performance is in-line with the expectations in literature. The benefit of having the analyzed CDA for OD-OP is immense, as long-term predictions could be made with minimal PE contributions. However, in order to cope with CP-based OD issues such as cycle-slips, a robust real-time method to determine the quality of an OD solution would be needed.

Contents

Nomenclature

Abbreviations

Abbreviation	Definition
BDA	Basic Dynamic Algorithm
BF	Body-fixed
CDA	Complex Dynamic Algorithm
CL	Computational Load
CP	Carrier Phase
CPA	Coarse Pointing Assembly
DD	Double-Difference
DF	Dual Frequency
DM	Dynamical Models
DOD	Dynamic Orbit Determination
DORIS	Doppler Orbitography and Radiopositioning Integrated by Satellite
DSST	Draper Semi-analytical Satellite Theory
ECEF	Earth-Centered Earth Fixed
ECI	Earth-Centered Inertial
EGM	Earth Gravity field Model
EKF	Extended Kalman Filter
EOM	Equations of Motion
EOP	Earth Observation Parameters
FOV	Field of View
FPA	Fine Pointing Assembly
GDOP	Geometric Dilution of Precision
GEO	Geostationary Earth Orbit
GS	Ground Station
GNSS	Global Navigation Satellite System
GP	General Perturbation
GPS	Global Positioning System
GRAPHIC	Group And Phase Ionospheric Correction
IAU	International Astronomical Union
IC	Initial Condition
IERS	International Earth Rotation Services
ITCF	International Celestial Reference Frame
ITRF	International Terrestrial Reference Frame
KA	Kinematic Algorithm
KF	Kalman Filter
LCT	Laser Communication Terminal
LF	LCT frame
LEO	Low Earth Orbit
LISL	Laser Inter-satellite Link
LOS	Line of Sight
MEO	Medium Eearth Orbit
MJD	Modified Julian Date
ML	Machine Learning
NRM	Newton-Raphson Method
NRPC	Newton-Raphson Predictor-Corrector

Abbreviation	Definition
OB	On-board
OBC	On-board Computer
OD	Orbit Determination
OD-OP	Orbit Determination and Orbit Prediction
OP	Orbit Prediction
OSA	Optical System Assembly
PAA	Point Ahead Angle
PAT	Pointing Acquisition and Tracking
PEKF	Preprocessing Extended Kalman Filter
PR	Pseudorange
PRN	Pseudorandom Noise
RDOD	Reduced Dynamic Orbit Determination
RF	Radio Frequency
RK	Runge-Kutta
RQ	Research Question
RMS	Root Mean Square
SF	Single-Frequency
SGP4	Simplified General Perturbations 4
SLR	Satellite Laser Ranging
SP	Special Perturbation
SPP	Single Point Positioning
SPUKF	Single Propagation Unscented Kalman Filter
SRP	Solar Radiation Pressure
SST	Semianalytical Satellite Theory
STM	State Transition Matrix
SV	Space Vehicle
SVM	Support Vector Machine
TLE	Two-line Element
TUDAT	TU Delft Astrodynamic Toolbox
UC	Uncertainty Cone
UKF	Unscented Kalman Filter
ZD	Zero-Difference

Symbols

Symbol	Definition	Unit
$\boldsymbol{a}$	Acceleration	[m/s^2]
$\boldsymbol{a_e}$	Empirical accelerations	[m/s^2]
$\boldsymbol{a}_{pert}$	Perturbing acceleration terms	[m/s^2]
$\boldsymbol{a}_{pmg}$	Earth spherical acceleration term	[m/s^2]
$\boldsymbol{A}$	Pseudo-ambiguity Vector	[-]
A_D	Effective area exposed to aerodynamic drag	[m^2]
A_{SRP}	Effective area exposed to solar radiation	[m^2]
A_1, A_2	Unmodulated L1 and L2 carrier wave amplitude	[-]
$\boldsymbol{AE}$	Azimuth and Elevation	[deg]
b_{xi}, b_{yi}, b_{zi}	Direction cosines	[-]
B	Unknown number of Carrier Phase Cycles	[m]
$\boldsymbol{B}$	Vector of Unknown number of Carrier Phase Cycles	[m]
c	Speed of light	[m/s]
C_D	Drag Coefficient	[-]
C_R	Radiation Pressure Coefficient	[-]
d	Geometrical distance	[m]
d_r	Receiver specific group delay	[s]

Symbol	Definition	Unit
d^s	Navigation satellite specific group delay	[s]
d_I	Ionospheric delay	[m]
d_T	Tropospheric delay	[m]
dt_r	GNSS receiver clock error	[s]
$d\hat{t}_r$	GNSS receiver true clock error	[s]
dt^s	Navigation satellite clock error	[s]
DC	Navigation message	[-]
$f()$	State derivative function	[-]
f_0	Fundamental GPS signal frequency	[MHz]
f_1, f_2	L1 and L2 carrier frequency	[MHz]
h	Altitude	[km]
$h()$	Observation model	[-]
$\boldsymbol{H}$	Observation Sensitivity Matrix	[-]
i	Inclination	[deg]
$\boldsymbol{I}$	Identity Matrix	[-]
J	Zonal Earth Gravity terms	[-]
$J()$	Jacobian Matrix	[-]
$\boldsymbol{K}$	Kalman gain Matrix	[-]
$\boldsymbol{L}()$	Loss function	[-]
$L1, L2$	L1 and L2 Modulated Carrier Wave Signal	[-]
n_d	Number of days	[d]
n_{hr}	Number of hours	[h]
n_{min}	Number of minutes	[min]
n_{mo}	Number of months	[mo]
n_{LS}	Number of Leap Seconds	[s]
n_s	Number of seconds	[s]
n_{yr}	Number of years	[yr]
m	Mass	[kg]
m_e	Empirical Acceleration Damping Term	[-]
$\hat{\boldsymbol{n}}$	Surface normal Vector	[-]
$\boldsymbol{N}$	Nutation Rotation Matrix	[-]
p_T	Loop transient errors	[m]
$\boldsymbol{P}$	Precession Rotation Matrix	[-]
$\boldsymbol{P}_a$	Augmented Covariance Matrix	[-]
$\boldsymbol{P}_{d,o}$	Legendre polynomial	[-]
$\boldsymbol{P}_{XW}$	Cross Covariance Matrix	[-]
$\boldsymbol{P}^-$	Predicted Covariance Matrix	[-]
$\boldsymbol{P}^+$	Corrected Covariance Matrix	[-]
PC	Precision Code	[-]
q	Earth dynamic parameters	[-]
$\boldsymbol{Q}$	Error Covariance Matrix	[-]
$\boldsymbol{r}$	Cartesian Position	$[m]$
$\hat{\boldsymbol{r}}$	True satellite position	[m]
$\boldsymbol{r}_h$	Host Satellite Cartesian Position	[m]
$\boldsymbol{r}_{pred}$	Predicted Cartesian Position	[m]
$\boldsymbol{r}_t$	Target Satellite Cartesian Position	[m]
$\dot{\boldsymbol{r}}$	Cartesian Velocity	[m/s]
$\ddot{\boldsymbol{r}}$	Satellite Cartesian acceleration	[m/s^2]
$\boldsymbol{R}$	Covariance of measurement errors	[-]
R_E	Mean Earth Radius	[m]
$\boldsymbol{ROT}$	Rotation Matrix	[-]
$\boldsymbol{ROT}_{\mathbf{1/2/3}}$	Rotation matrices around principal axes	[-]
$\boldsymbol{s}$	Sought numerical solution	[-]
$\hat{\boldsymbol{s}}$	Predicted numerical solution	[-]

Symbol	Definition	Unit
$\boldsymbol{S}$	Sensitivity Matrix	[-]
$\boldsymbol{S}_{CR}, \boldsymbol{S}_{CD}, \boldsymbol{S}_{\boldsymbol{a}}$	Sensitivity to SRP, drag and $\boldsymbol{a}_e$	[-]
t	Time	[s]
t_{JD}	Julian Date	[d]
t_{MJD}	Modified Julian Date	[d]
t_{TAI}	Universal Atomic Time	[date]
t_{TGPS}	GPS Time	[date]
$t_{TGPS,s}$	GPS Time in second format	[s]
t_{TT}	Terrestrial Time	[date]
T_{UT1}	Julian Centuries since 2000-1-1.5 at current UT1	[centuries]
U	Earth Potential Terms	[m^2/s^2]
t_{UTC}	Coordinates Universal Time	[date]
t_{UT1}	Universal Time	[date]
v	Measurement errors	[-]
$\boldsymbol{W}$	Process Noise	[-]
WC	Encryption Code	[-]
x, y, z	Cartesian position components	[m]
$\dot{x}, \dot{y}, \dot{z}$	Cartesian velocity components	[m/s]
$\ddot{x}, \ddot{y}, \ddot{z}$	Cartesian acceleration components	[m/s^2]
x_p, y_p	Earth's polar motion angles	["]
$\boldsymbol{X}$	Filter State	[-]
$\boldsymbol{X}_a$	Augmented Filter State	[-]
$\dot{\boldsymbol{X}}$	Filter State Derivative	[-]
$\boldsymbol{X}^+$	Corrected State	[-]
$\boldsymbol{X}^-$	Predicted State	[-]
Y	Singular Measurement	[m]
$\boldsymbol{Y}$	Measurement Vector	[m]
Y_{C1L1}	C/A and L1 pseudorange Measurement combination	[m]
$Y_{C/A}$	C/A pseudorange Measurement	[m]
Y_{L1}, Y_{L2}	L1 and L2 pseudorange measurement	[m]
Y_{L12}	L1 and L2 pseudorange measurement combination	[m]
Y_{P1}, Y_{P2}	P1 and P2 pseudorange Measurement	[m]
Y_{P12}	P1 and P2 pseudorange Measurement combination	[m]
z_k	Predicted measurement for navigation satellite k	[m]
β	Reference angle	[rad]
δ	Change in value	[-]
Δ	Step in value	[-]
ϵ	Unmodelled errors	[m]
ϵ_{mp}	Multipath errors	[m]
ϵ_n	Tracking noise errors	[m]
$\boldsymbol{\theta}$	Attitude	[rad]
θ_{ERA}	Earth Rotation Angle	[rad]
θ_{GMST}	Greenwich Mean Sidereal Time rotation	[rad]
μ_E	Earth Gravitational Parameter	[m^3/s^2]
$\boldsymbol{\Pi}$	Polar motion Matrix	[-]
ρ_{atm}	Atmospheric density	[kg/m^3]
τ	Correlation time	[s]
$\boldsymbol{\Phi}$	Complete transition Matrix	[-]
$\boldsymbol{\Phi}_r$	State transition Matrix	[-]
ω_E	Earth rotational velocity	[rad/s]
$\boldsymbol{\omega_E}$	Earth rotational velocity Vector	[rad/s]
$\boldsymbol{\Omega}$	Sidereal time rotation Matrix	[-]

Subscripts	Definition
$central$	Central body
d	Degree of Spherical Harmonic terms
$drag$	Aerodynamic drag
E	Earth
$GNSS$	Navigation satellite
h	Host Satellite
i	Tracked navigation satellite index
int	Truncation to integer value
j	Iteration number.
k	Discrete value at time-step k
o	Order of Spherical Harmonic terms
$pert$	Perturbing
pmg	Point-mass Gravity
$pred$	Predicted
r	GNSS receiver
rel	Relative
R, d	Diffuse reflection term
R, s	Specular reflection term
s	Sigma point
sun	Pointing towards the Sun
SRP	Solar Radiation Pressure
t	Target Satellite
0	Initialized value
$3rd$	Third body

Superscripts	Definition
BF	Body-fixed
$ECEF$	Earth-centered Earth-Fixed
ECI	Earth-centered Inertial
LCT	Laser Communication Terminal
s	Navigation Satellite
$*$	Computed value when using Broadcast ephemeris

1 Introduction

The goals for this introductory chapter are explaining the importance of Satellite Laser communication, necessity of relative navigation knowledge and where this research fits in the industrial and academic fields. This is done by first providing background of the project in section 1.1. Subsequently, previous laser communication missions and communication satellite constellations and the constellation used for this research are documented in section 1.2. Afterwards, attention is be brought to orbit determination and prediction options in section 1.3, where the analysed methods are defined. The research aims and their importance are discussed in section 1.4, where the central research questions are listed. Finally, the outline of the entire report is presented in section 1.5.

1.1. Project Background

In subsection 1.1.1, the benefits and potential applications of laser communications are introduced. In subsection 1.1.2, the importance of Pointing, Acquisition and Tracking schemes are mentioned. Finally, the background of Mynaric and its developed and manufactured laser communication terminals are documented in subsection 1.1.3.

1.1.1. Laser Communication Benefits

Laser communication provides various benefits over typical Radio Frequency (RF) communication. Compared to RF, optical communication requires considerably less power, does not occupy regulated frequency bands, provides much higher data rates, has lower risk of jamming and are much safer due to having a beam width of around 10 urad [50]. With the demand for bandwidth continuously increasing, RF communication systems have the inherit issue of restricted and limited spectrum usage, whereas optical communication does not have frequency usage restrictions. Additionally, optical frequencies can be reused, which is made possible by the small beam divergence of communication laser beams [20]. Due to all the aforementioned benefits, free-space optical technology is expected to meet the ever increasing bandwidth needs [41].

Optical links can be further utilized for space applications. Specific use cases include relay of high-resolution Earth observation data or providing global internet connectivity. Laser Inter-satellite Links (LISL) can be used for communication between individual satellites or entire satellite constellations. Links are also possible from space to aircraft or UAV's. The potential optical link categories are shown in Figure 1.1. These technologies can provide connectivity to commercial aircraft, enable high-speed communication between satellites, enable capabilities to downlink higher volumes of Earth Observation. Finally, providing global communication would connect all- urban, rural and areas that cannot be reached by radio-towers, even providing maritime connectivity.

1.1.2. Pointing, Acquisition and Tracking

Although LISL have extremely favourable qualities, they also require significant efforts. Optical beamwidth for long-range communication is in the range of 10-30 urad. In contrast, Pointing Errors (PE) due to platform motion, Point-ahead angles, imperfect initial relative position and attitude knowledge are in the mrad range- over 100 times larger than the beam divergence. Thus, a Pointing, Acquisition and

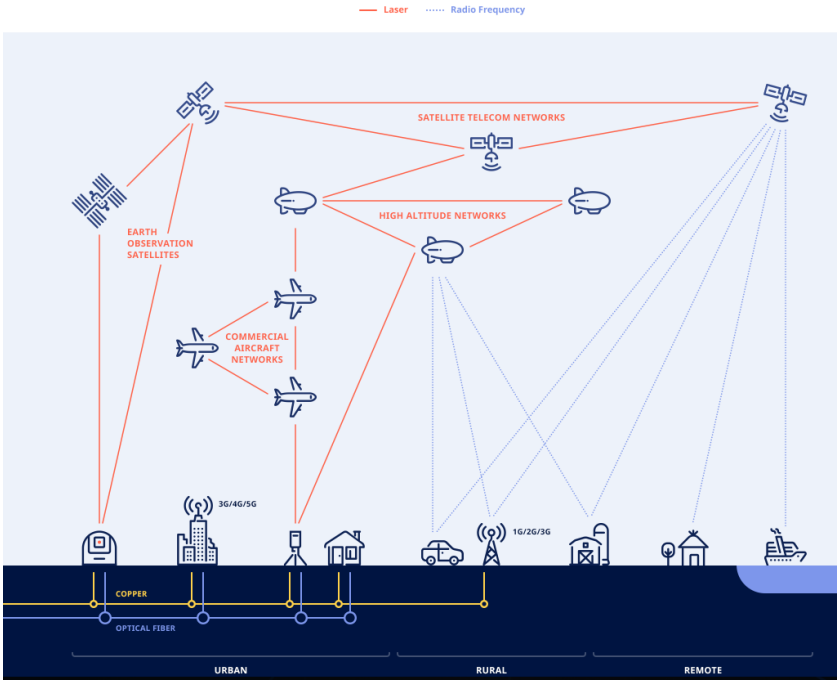

Figure 1.1: System architecture diagram of the Mynaric laser communication network. [43]

Tracking (PAT) system is critical to compensate for these PE and systematically acquire, and maintain a LISL [20].

In order to reduce the PE from mrad to sub-urad levels, the PAT system first performs an acquisition scan of the initial Uncertainty Cone (UC), searching for the receiving beacon, then links the beams, switches to narrow beam communication and maintains alignment. At this point, communication can be initialized and tracking follows.

A critical goal is to minimize the link acquisition time and maximize acquisition success rates, leading to overall more communication time. Link acquisition by itself is a key technology for satellite laser communication. However, this will not be looked into during this thesis, as in general- the bigger the initial Pointing UC is, the more time and lower success rates for link acquisition can be expected. Therefore, the thesis instead will be focused on minimizing a specific UC contribution.

Among these UC contributions is the relative Line of Sight (LOS) vector error. The LOS depends on the relative position knowledge between the host and target satellites, as well as the host's attitude. While the attitude knowledge is provided by common attitude sensors, position information is challenging to quickly and accurately determine for the host satellite [20].

While there is no hard limit on the total UC to enable link acquisition, a general threshold shall be setup. In previous missions, experimental and simulation tests have indicated various results. In [58] it is mentioned that the SILEX Laser Communication Terminal (LCT) on-board the ARTEMIS satellite spirally scanned a 1.7 mrad pointing UC with a wide beacon laser and succeeded in most of the attempted LISL with the SPOT-4 satellite. [76] indicated that using numerical simulations, spatial acquisition could be established with an average of 10s for a 1-mrad UC. Considering the LOS error, it is only one of many UC components. Therefore, a more conservative threshold will be set-up of 0.5 mrad to accommodate for other PE contributions.

1.1.3. Mynaric CONDOR Terminals

Mynaric develops LCT which are specifically focused on free-space optical communication in aerospace applications. Mynaric was founded in 2009, as a spin-off of DLR's Institute of Navigation and Communication, which has worked on LCT's for 20+ years. Since then, Mynaric has demonstrated high-speed links in air-air, air-ground and ground-ground scenarios. Now, some of Mynaric's goals include developing and manufacturing LCT's for large satellite constellations in LEO [41] and providing LCT's for LEO-MEO relay links [23].

Mynaric's LCT's for space applications are called CONDOR terminals and are specialized for LISL. An overview of the 1st-generation CONDOR Mk1 LCT can be seen in Figure 1.2. CONDOR Mk1 was designed for a link distance <4500 km in LEO and providing data rates of 10 Gbps. Its Optical System Assembly (OSA) consisted of [41]:

- Coarse Pointing Assembly (CPA) - consisting of a steerable mirror and responsible for establishing steady pointing toward the target satellite. It provides large angular motions to cope with the link dynamics for initial open loop pointing and acquisition.
- Telescope Assembly - an afocal telescope, tasked with magnifying or reducing the received/outgoing beam diameter to achieve the required optical quality of the laser.
- Transmitting (Tx)/Receiving (Rx) Optics - containing an inner optical subsystem, which collimates the Tx beam, stabilizes/separates the Tx/Rx beams, actuates the Point-Ahead Angle (PAA) of the Tx beam, tracks error feedback measurements, etc.

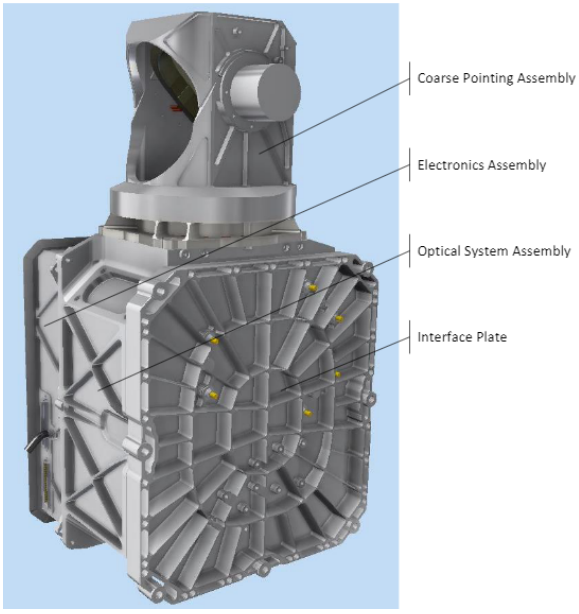

Figure 1.2: CONDOR Mk1 system overview [41]

The 2nd and 3rd generation LCT's- CONDOR Mk2 and CONDOR Mk3 can be seen in Figure 1.3. CONDOR Mk2 was built to establish intra-plane and cross-plane LISL in LEO, supporting distances up to 5000 km. Meanwhile, CONDOR Mk3 supports link distances over 10000 km, thus enabling links to MEO. In CONDOR's case, satellite laser communication is split into 2 pointing procedures- coarse and fine pointing. The CPA covers the large field of range due to the satellite link dynamics and compensates for the target satellite's attitude actuators. It leads to a small enough pointing uncertainty cone, such that the Fine Pointing Assembly (FPA) can detect the target beacon and establish a link.

A diagram of the coarse pointing knowledge flow and its key algorithms can be seen in Figure 1.4. The entire system here is split into 3 components- the CONDOR LCT, Host Satellite Platform and the Ground Segment. The initial pointing knowledge processing steps are as follows:

- Orbit Determination. The GLoban Navigation Satellite System (GNSS) receiver provides discrete pseudorange/carrier phase measurements $\boldsymbol{y}_k$, which are processed by the Orbit Determination (OD) algorithm to determine the host satellite position $\boldsymbol{x}_h$ at time t_k
- Orbit Prediction. The OP algorithm receives the determined host satellite position $\boldsymbol{x}_h$ at time t_k and the uplinked target satellite position $\boldsymbol{x}_t$ at time t_T. Both of the positions are propagated for the communication time window t, resulting in the predicted target $\boldsymbol{x}_{t,pred}(t)$ and host $\boldsymbol{x}_{h,pred}(t)$ positions.
- Relative Pointing Calculation. The Cartesian host and target satellite coordinates are converted to a relative LOS vector, which goes through transformations to the horizontal vehicle-carried reference frame. Using the host satellite's attitude information $\boldsymbol{\theta}_h(t)$, the body-fixed frame LOS is

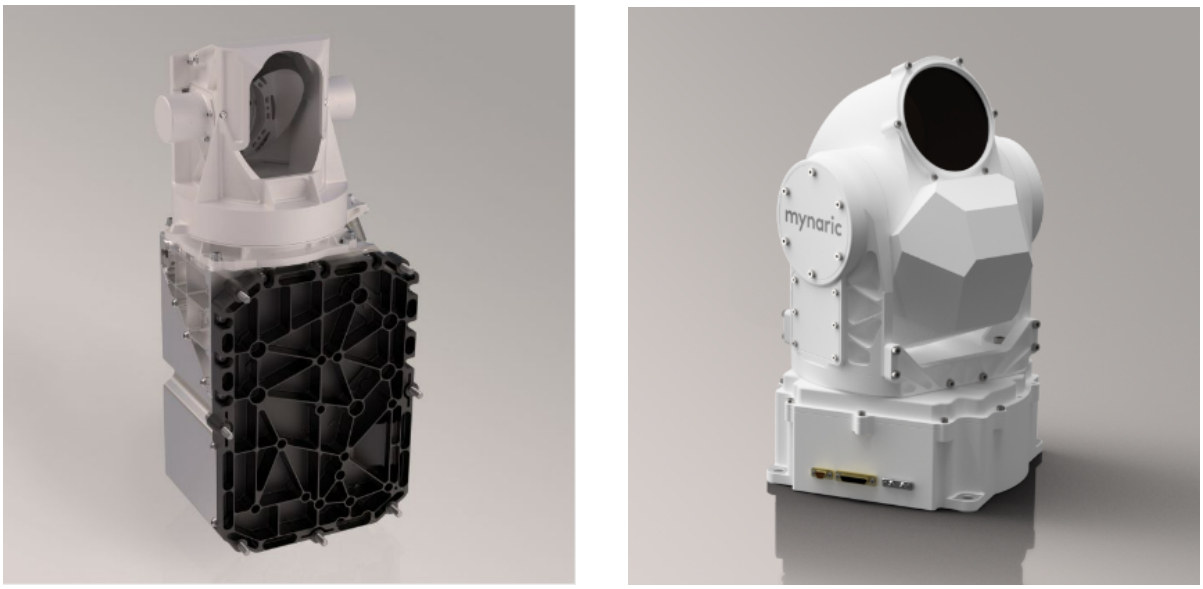

(a) CONDOR Mk2 [24].

(b) CONDOR Mk3 [25].

Figure 1.3: Optical System Assemblies of Mynaric's 2nd and 3rd generation Space LCTs.

computed, which can then be converted to the terminal frame. This leads to the pointing vector representation in Azimuth/Elevation angles for the prediction window $\boldsymbol{\theta}_{pred}(t)$.

- The Coarse Pointing Assembly points the Tx/Rx optics towards the the target satellite, providing the pointing at an accuracy of $\boldsymbol{\theta}_{coarse}(t)$, which leads to the Initial Uncertainty Cone to be scanned by the Pointing Acquisition and Tracking system.

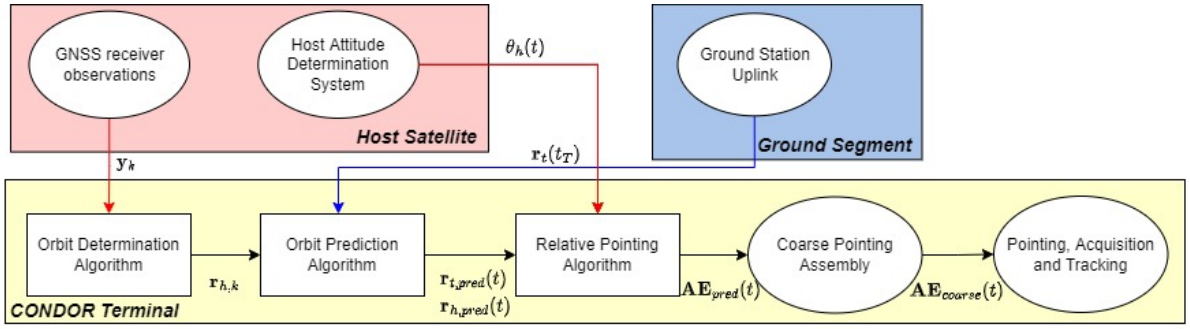

Figure 1.4: Initial Coarse Pointing knowledge components and the relevant algorithms.

This thesis will be contribute to Mynaric's goals by improving the host and target satellite's pointing knowledge and quantifying its impact on the UC. This will be done by analysing the initial OD and subsequent OP. The analysis will be done in the context of LEO and MEO satellite LISL with the pointing limitations of CONDOR Mk2 and Mk3, evaluating the resulting UC in various link cases and communication windows lengths. In the future, the results will be used as guidelines for the software to be used on Mynaric's LCTs.

1.2. Satellite Laser Communication

In this section, the state of the art in satellite laser communication will be presented and the constellation to be analyzed in this report will be defined. First, past laser communication satellites will be documented in subsection 1.2.1. Subsequently, in subsection 1.2.2. Finally, the chosen LEO/MEO constellation parameters will be presented in subsection 1.2.3.

1.2.1. Past Laser Communication Satellites

Optical communication between satellites began in late 20th century, in various link cases. In 1980s, an experimental demonstration, as described by [52], a LISL was established from LEO to Geostationary Orbit (GEO) and vice-versa between the French Earth observation SPOT-4 AND European telecommunication ARTEMIS satellites [12]. GEO-ground links were established by the Japanese OICETS in 2006, as described by [27]. In LEO, LISL were established in 2008 between the TerraSAR-X and NFIRE satellites, while [19] describes the ground-LEO uplink to NFIRE in 2010. In 2013, NASA's LLCD program established Lunar-ground links [42]. LEO-ground downlinks were done in 2014, on SOCRATES [8]. European Data Relay System (EDRS) established GEO-ground downlinks in 2016 using TESAT's second generation LCT [49]. In 2017, LEO-ground downlinks were established by on a cubesat by NASA's OCSD program [54]. [32] mentions the microsatellite RISESAT, which established LEO-ground downlinks in 2019. DLR's OSIRIS program is developing LEO-ground LCT's for small satellites [13]. The upcoming CLICK mission aims at demonstrating full-duplex LISL in addition to downlinks from cubesats in LEO [56]. Despite LISL being demonstrated between ground, the Moon, LEO and GEO, none have yet been done in MEO.

1.2.2. Planned Laser Communication Constellations

An overview of currently planned communication satellite constellation shells can be seen in Table 1.1. Of the listed constellations, Amazon's Kuiper plans to utilize Ka-band without specifying if they intend to utilize ISL. Telesat will operate in the Ku-band and will utilize intra and cross-plane ISL. Both OneWeb and SpaceX will utilize Ku-band. OneWeb does not intend to utilize ISL from the start of operations, while SpaceX's Starlink plans to utilize LISL.

It can be seen that the constellations mainly target the highly populated area coverage. The majority of the satellites will be in inclined orbital planes. While all the shells of Kuiper are inclined, the other constellations have smaller numbers of satellites in near-polar orbits to provide coverage to the less populated areas.

Table 1.1: Orbital Parameters of Communication Satellite Constellations, according to their FCC filings

Constellation	h [km]	i [deg]	Nr. Planes [-]	Sat/Plane [-]	Nr. Total sat. [-]
SpaceX's Starlink [60]	550	53	72	22	4408
	540	53.2	72	22	
	570	70	36	20	
	560	97.6	6	58	
	560	97.6	4	43	
Telesat [65]	1015	98.98	27	13	1671
	1325	50.88	40	33	
OneWeb [45]	1200	87.9	36	49	6372
	1200	40	32	72	
	1200	55	32	72	
Amazon's Kuiper [63]	630	51.9	34	34	3236
	610	42	36	36	
	590	33	28	28	

1.2.3. Chosen Constellation

The constellation used in the link analysis will consist of two LEO and a single equatorial MEO shell. A thorough constellation design will not be performed in this research. Firstly, it is outside of the chosen scope. Furthermore, Mynaric aim to deliver the LCT as a payload module, but are not involved with the LEO/MEO satellite platform or constellation design. Nevertheless, a choice must still be made on the basic constellation structure, as this will dictate the LISL dynamics. The constellation shells are summarized in Table 1.2.

This constellation will be simulated for 24 hours using TUDAT. The constellation choice is loosely based on expected use cases, previously analyzed orbital scenarios and historical constellation design choices. The argumentation is as follows:

- The LEO shell altitudes are chosen to match fitting orbital scenarios for Laser Communication.

Table 1.2: Orbital parameters of the selected Laser communication Satellite Constellation. All considered shells are in circular orbits.

Constellation	h [km]	i [deg]	Nr. Pl. [-]	Sat/Pl. [-]	Nr. tot. sat. [-]	T [hr]
LEO near-polar	1000	89	13	14	182	1.75
LEO med. Incl.	1000	53	13	14	182	1.75
MEO	13892	0	1	5	5	7.97

- The adjacent orbital plane spacing within a single LEO shell was chosen to provide cross-plane link opportunities. This means the maximum distance does not exceed 4000 km. With 13 planes per shell, the cross-plane distance at the equator is roughly 3520 km. This leaves an additional margin for maximum link distance increase due to the satellite relative phasing.
- The intra-orbit spacing for the LEO shells is roughly 3300 km with 14 satellites per plane at the chosen altitude. This is well within the maximum link distance supported by the CONDOR Mk2.
- Two LEO shells were chosen- near-polar and medium inclination. The medium inclination shell is a common use case, as this inclination is inexpensive in terms of ΔV needed for the launch and covers the most populated regions of Earth. The near-polar orbit was added to add coverage to the high latitude and polar regions, in addition to being a desired inclination for maximum coverage in observation missions [36]. The two shells combined will provide global coverage and will be sufficient to quantify the challenging fast-dynamic cross-plane LEO link cases.
- The MEO shell was chosen rather loosely- simply to provide challenging LEO-MEO, LISL cases. It was intentionally chosen not to have small relative velocities w.r.t. Earth's surface, as MEO-ground links are not a link case of interest for the CONDOR terminals.

1.3. Orbit Determination and Prediction Background

In this section, a brief overview of orbit determination and prediction methods is provided. This is done in subsection 1.3.1 and subsection 1.3.2, respectively. In subsection 1.3.3, it is explained which of those methods will be analyzed in this report.

1.3.1. Overview of Orbit Determination Methods

OD can be done on-ground and uplinked to the satellite or performed entirely on-board. Ground-based tracking systems include the French Doppler Orbitography and Radiopositioning Integrated by Satellite (DORIS) [74], the Satellite Laser Ranging (SLR) system [46] and the Two-line Element (TLE) tracking data provided by the US Space Surveillance Network. However, these methods depend on Ground Stations (GS) and generally have a poor latency, which leads to increasingly degraded OD accuracy before new measurements are available. In contrast, On-board (OB) Global Navigation Satellite System (GNSS) receivers can provide continuous measurements and can be processed on-board, delivering orbit solutions minutes or seconds after observations are made [71]. Therefore, only on-board GNSS-based OD methods will be considered.

Using Global Positioning System (GPS) data for OD has been done in the 1990s by JPL and GSFC, where the GEODE navigation software was developed. Using pseudorange measurements, EUVE OD was accurate to 10 m RMS, and TOPEX/POSEIDON- 7.8 m, as documented by [17]. The German Aerospace Center (DLR) developed the PHOENIX-XNS receiver, equipped with an integrated RTOD software for LEO satellites, which operated on X-SAT and PROBA-2 mini-satellites, as described by [14] and [39]. Utilizing an Extended Kalman filter (EKF), a high-fidelity reduced dynamic (RD) orbit model and using a linear combination of GPS 1 C/A code and carrier phase (CP) measurements, it provided an OD accuracy of 1 m [35]. [38] presented a prototype algorithm, compatible with current OB processors, using Group and Phase Ionospheric Correction (GRAPHIC) measurements, an EKF and a careful trade-off of the Dynmical Model (DM) achieving an OD accuracy of 0.4-0.6 m, using broadcast ephemerides.

Methods other than the EKF also show promise in GNSS-based OD. [70] points out the EKF uses first-order linearization of the nonlinear system, which can introduce large errors in the true posterior mean and covariance of the transformed state distribution, leading to sub-optimal performance/divergence of the filter, thus proposing using the Unscented Kalman Filter (UKF), which was first formulated

by [28] and uses nonlinear propagation. [29] stated that in GPS navigation, the EKF issues are relevant. [9] applied the UKF in GPS-based OB OD of CHAMP and KOMPTSAT-2, achieving more stable and accurate OD than the EKF. [51] compared the UKF and EKF and found the UKF converges faster and is less likely to diverge for low-fidelity DM, which is relevant for computationally limited OB OD methods. [5] investigated Single Propagation UKF (SPUKF), where only the sigma point representing the a-posteriori mean state vector was propagated. Compared to an UKF, the SPUKF was 92.6% faster with a similar accuracy. Another modification to the classical EKF OD was investigated by [3], who added a preprocessing block to the EKF. First resolving the pseudorange measurements into a coarse position solution using the multivariate Newton-Raphson Method (NRM). It can be used for EKF initialization and as the measurement, for an overall simpler filter formulation. Compared to a typical EKF, the Preprocessing-EKF (PEKF) lead to a slightly increased OD accuracy, but the run-time increased by 50%.

1.3.2. Overview of Orbit Prediction Methods

An exact number of orbit prediction schemes is difficult to establish, as these algorithms can differ both in fundamental formulation ways and in very minor modifications. Fortunately, in general, Orbit Prediction methods can be summarized into 3 distinct categories [68]:

1. **General Perturbation** (GP) methods, where the orbit is calculated analytically. These methods are generally computationally light but are limited in their achievable accuracy. They require analytical approximations of the considered accelerations, are generally formulated in element space (Keplerian, Equinoctial), They require the considered perturbations to be separated in terms of long and short periodic, and secular terms [6] and are usually expressed in series expansions. The most commonly used implementation is the Simplified General Perturbations 4 (SGP4) orbit propagator, based on modified Brouwer's theory [7], which includes different perturbing accelerations based on the orbital period. SGP4 is the currently used theory to maintain the NORAD catalogue.
2. **Special Perturbation** (SP) methods, which numerically integrate the EOM. These techniques are generally computationally much heavier, but can also produce very accurate results compared to GP methods. SP require accurate modelling of the perturbing effects, which allow to express them as perturbing accelerations in the EOM. Provided with initial conditions, the EOM can then be numerically integrated to the next step. Therefore, SP techniques not only suffer from limited physical model accuracy, but also contain Truncation Errors (TE)- due to the limited order of the numerical integrator and Rounding Errors (RE) due to the limited numerical representation, Nevertheless, these techniques are often used to derive the ”truth” trajectories in analyses.
3. **Semianalytical Sattelite Theory** (SST) techniques, which combine the features of GP and SP, leading to a mix between their accuracy and efficiency. While the fast-varying elements are expressed with analytical approximations, numerical integrators are used for the slow varying elements.

Significant effort in OP research has been aimed towards utilizing Machine Learning (ML) techniques. There is a lack of knowledge of the space/time variation of Earth gravity, atmospheric drag, solar radiation pressure and the space object's initial state [47], which limits the accuracy of physics-based OP methods. In contrast, ML presents different modelling capabilities, as they are based on large amounts of data. In [47], the potential of ML applied to OP was analyzed by simulating LEO satellite truth orbits and GS measurements. First, the orbit was predicted with a reduced dynamic method and then corrected with the Support Vector Machine (SVM) method. It was shown that from the simulated tracking data, SVM can indeed learn the underlying unmodelled orbit pattern. In [55], it was proposed to improve the Simplified General Perturbations 4 (SGP4) model using Lost Short-Term Memory (LSTM). OP accuracy was also improved by training a SVM with TLE data [48], showing potential in using these methods for collision avoidance.

1.3.3. Chosen Approaches

While many options are available for both OD and OP, only a limited number of techniques can be analyzed further. Therefore, multiple OD and a single OP technique will be selected based on their applicability to LISL.

For the GNSS-OD portion, only Single Frequency (SF) measurement-based approaches will be analyzed. SF receivers are low-cost and consume less energy than Dual Frequency receivers [61], thus only techniques using SF GNSS measurements will be considered.

Regarding OD algorithm formulations, multiple candidates will be considered. The typical EKF will be implemented, as it is the industry standard and is relatively easy to implement and tune [36]. The UKF was found to diverge less with simplified Dynamical Model (DM), making it another promising option. Of the novel filter formulations, SPUKF and PEKF can be highlighted. SPUKF was shown to perform as a computationally lighter UKF. PEKF, although having a higher Computational Load (CL) than EKF, indicated more accurate performance and had other favourable qualities like availability of coarse solutions and self-initialization.

Regarding orbit prediction, many options will be discarded and only SP techniques will be considered. ML techniques will not be analyzed in this report, as they are computationally heavy, require large amounts of data and are not yet flight proven. Therefore, they are not well suited for on-board satellite navigation purposes.

Analytical/GP and semi-analytical (SST) OP methods can be beneficial in some cases, but they will are‘ excluded from the scope due to their poor applicability to laser communication. Analytical OP, although commonly used, generally does not provide sufficient accuracy, requires additional reference frame transformations and loses some of its CL advantages when higher sampling rates and shorter prediction windows are needed. This also means that widely used TLE-based approaches are poorly applicable here. Semi-analytical methods do provide promising CL and OP accuracy, but are not openly available and non-proprietary versions are difficult to obtain [57].

In contrast, SP/numerical propagation methods are favourable for LISL. Their precision and CL can be relatively straightforwardly altered by choosing DM simplifications and neglecting perturbations. Therefore, they can be made as computationally-light and as precise as necessary for LISL.

1.4. Scope of the Research

In subsection 1.4.1, the aims and scope of the research is defined. Subsequently, the Central Research questions and their sub-questions are listed in subsection 1.4.2.

1.4.1. Aims of the Research

This research will be focused on improving the host and target satellite's pointing knowledge and quantifying its impact on the pointing UC for LISL. This will be done by analysing the host's initial OB GNSS-based OD and subsequent target and host OP, while considering the attitude data to be known perfectly.

The aims of this research will be academic, while being tailored to provide analysis relevant to Mynaric's CONDOR terminals Mk2 and Mk3. Academically, the goals will be to cover research gaps in GNSS-based OB OD by improving an existing OD method and comparing it to other common OD methods. Additionally, recently developed GNSS-based OD methods will be tested with flight data for the first time. Furthermore, the GNSS-based OD and subsequent OP methods' will be evaluated in terms of their impact on the PE. The analysis will be done in the context of LEO and MEO satellite LISL, evaluating the resulting pointing UC in various link cases and communication windows lengths.

In order to apply the algorithms to a laser communication satellite constellation, the link geometry must be known. This will require the simulation of a LEO/MEO satellite constellation. Doing so will allow to evaluate the communication window lengths, expected pointing angle ranges and their rates. Knowing the communication window lengths will be used to determine the most relevant prediction window lengths for the OP methods. Additionally, knowing the pointing angles and rates for various LISL types, increasingly challenging link cases can be determined to benchmark the OD-OP algorithm performance and their impact on each scenario.

To evaluate the applicability of each OD-OP algorithm, its PE contribution will be compared to a constant threshold. The total PE budget has many sources, such as spacecraft body-pointing errors, micro-vibrations, point-ahead errors, thermal deformations, launch-induced shift [56] and thus the coarse pointing error is just one of the contributors. Therefore, a conservative threshold of 0.5 mrad is considered for both terminals.

Orbital simulations will be carried out using TU Delft Astrodynamic Toolbox (TUDAT) software [22].

TUDAT provides the necessary freedom (various dynamical models, numerical integrators, propagated body settings, acceleration formulations) to setup the various-precision orbit simulations for this report. Additionally, it is a free verified tool.

GNSS-OD algorithms and all necessary blocks will be implemented using base python libraries. These include multiple Kalman Filters (KF), the kinematic OD methods as well as specific blocks required for GNSS data processing. Those include reading and processing RINEX files and converting GNSS broadcast ephemerides into navigation vehicle orbits.

After analysing and determining the recommended OD and OP software, at some point it will be implemented and thus needs to consider OB Computer (OBC) needs. Although it is not required to provide the actual software to be used on-board, a blueprint for this software module will be delivered. This imposes two requirements: first, the OD/OP software shall be independent of any external libraries, secondly, the OD/OP methods shall be compatible with currently available OBC. This means, that the CL of the chosen methods must be on the same or lower CL than previously used OD/OP algorithms that have flight experience.

The GPS modules to be used for Mynaric's CONDOR terminals are not known. Therefore, when testing the methods, publicly available GPS receiver and representative satellite data will be used. This includes data from CHAMP, GRACE-FO and Jason-3 missions.

1.4.2. Research Questions

Broad central Research Questions (RQ) and the subsequent narrower sub-questions were set up to cover each aspect of the thesis. Once the sub-questions are answered, in combination will provide an answer to each central question.

The first question covers the link geometry and communication windows for each terminal configuration in the analyzed LEO/MEO constellation. An aim is to quantify the critical communication windows which determine the LOS prediction time length and to select a number of occurring link cases which capture the scope of easy-difficult link conditions in the LEO-MEO constellation. The communication windows and link cases will be used to benchmark the integrated OD-OP algorithm performance in RQ3.

The second question is aimed at covering some gaps in GNSS-based OD and determining the optimum algorithm for on-board use. Novel KF with promising accuracy/CL qualities - PEKF and SPUKF will be implemented and for the first time tested with GNSS receiver measurements collected on the CHAMP, Jason-3 and GRACE-FO missions. Their accuracy will also be quantified with sparser measurements update rates. In addition, typical GNSS-OD methods will be implemented and their performance will be quantified and compared to the novel filters to provide initial OD errors for the subsequent OP. Finally, an attempt will be made to improve the original PEKF using NRM by implementing a NRPC-PEKF and testing whether the higher efficiency numerical method compensates for the added CL of the original PEKF.

The third central question interfaces the outcomes from the first two RQ with subsequent OP algorithms to evaluate the overall PE contribution of these algorithms in LISL use cases. These OD-OP algorithms will use increasingly complex OD options and OP methods, ranging from fully kinematic to complex-dynamic. LISL cases quantified in RQ1 will be used to quantify the PE contribution of each OD-OP algorithm for the critical communication windows. Furthermore, the OD-OP algorithm performance will be evaluated for link-acquisition purposes, analyzing the maximum PE contribution depending on the link conditions. Conclusions regarding the applicability of each OD-OP algorithm for each link case will be made while regarding the 0.5 mrad maximum PE contribution threshold.

1. What Laser Inter-satellite link properties occur in a combined LEO/MEO satellite constellation?
   (a) What are the available communication window time distributions for the intra-orbit, inter-orbit and inter-shell in LEO-LEO, MEO-MEO, LEO-MEO and MEO-LEO links?
   (b) What are the critical communication time cut-offs in terms of available communication windows?
   (c) What are the ranges and rates of azimuth, elevation and link distance for the intra-orbit, inter-orbit and inter-shell in LEO-LEO, MEO-MEO, LEO-MEO and MEO-LEO links?
   (d) How many links of each type can be established by satellites in LEO and MEO to each orbital plane per orbital revolution?

2. Which Kalman Filter formulations are optimal for the initial GNSS-based on-board orbit determination in satellite constellations?
   (a) What errors are the expected RSW position and velocity errors for on-board kinematic and reduced-dynamic SF pseudorange based GNSS-OD methods?
   (b) What errors are the expected RSW position and velocity errors for on-board reduced-dynamic SF carrier-phase based GNSS-OD methods?
   (c) How do novel pseudorange-based NRM-PEKF and SPUKF perform with flight data compared to typical EKF and UKF formulations in terms of OD accuracy?
   (d) How do novel pseudorange-based NRM-PEKF and SPUKF perform with increasingly sparse measurement updates rates in terms of OD accuracy?
   (e) Does the performance of the NRM-PEKF algorithm, documented by [3] improve when using a higher efficiency NRPC root finding method in terms of OD accuracy or CL?
3. What is the performance of integrated OD-OP scheme for LISL in the combined LEO-MEO satellite constellation?
   (a) What is the PE contribution for increasingly complex integrated OD-OP algorithms in the LEO/MEO constellation during the critical communication windows?
   (b) What is the PE contribution for each OD-OP algorithm for the 100 second link-acquisition window throughout the available link communication window?
   (c) How long can each integrated OD-OP algorithm support each type of link LISL without exceeding the maximum allowed PE contribution threshold?

1.5. Report outline

The report is structured as follows. Having already introduced the project background and the scope of this research, the theory that will be applied in the technical work is documented in chapter 2. The chosen constellation is simulated in chapter 3, where the potential LISL and their pointing variables are quantified. Subsequently, multiple GNSS-based orbit determination methods are implemented and tested in chapter 4, where conclusions regarding the novel filter performance and the expected OD errors in satellite laser communication constellations are made. Finally, the OD algorithms are interfaced with the subsequent orbit prediction and they are benchmarked in chosen link cases in terms of their Pointing Error contributions in chapter 5. The main conclusions and further recommendations can be found in chapter 6.

2

Theoretical Background

In this chapter, the theoretical background behind the research are presented. Time systems are introduced in section 2.1, followed by relevant reference frames in section 2.2. Link geometry calculation is described in section 2.3, followed by GNSS background in section 2.4. Then, specifics of astrodynamic acceleration modelling are documented in section 2.5. Finally, the formulations for chosen GNSS-OD methods are explained in section 2.6

2.1. Time Systems

Time is fundamental in many branches of science, but it is especially critical in astrodynamics, due to how fast the objects are moving. Four time scales can be distinguished [68]:

1. Sidereal time, which is related to Earth's rotation around the Sun. It is defined by successful transits of distant starts over a local meridian.
2. Solar time, which is also related to Earth's rotation around the Sun. It is defined by successful transits of the Sun over a local meridian.
3. Dynamical time, which is based on the motion of bodies. Having a mathematical description of the motion of a body, by observing the motion from one point to another, it can be deduced how much time has elapsed.
4. Atomic time, which is based on specific quantum transitions of electrons in a cesium-133 atom, allowing to define a second as a fixed number of cycles.

Several distinguished realizations of the mentioned time systems are relevant and will be used in this project. GNSS broadcast ephemerides refer to GPS weeks and seconds, while precise orbit solutions refer to Julian Days since a specific epoch. Furthermore, TUDAT uses seconds since the J2000 epoch and therefore consistent conversions to a common time system need to be applied in order to have comparable results. The definitions and the relations of relevant time scales and systems are explained below.

TAI - International Atomic Time It is based on an atomic clock and is related to Terrestrial Time (TT) by adding a fixed 32.184 seconds as follows:

$$t_{TT} = t_{TAI} + 32.184 \tag{2.1}$$

TGPS - GPS time GPS time also works on the atomic time scale. Its origin is the same of Coordinated Universal Time (UTC) at 1980 January 6 00:00:00 UTC. It is ahead of of UTC by the number of leap seconds n_{LS}, added since 1980:

$$t_{TGPS} = t_{UTC} + n_{LS} \tag{2.2}$$

It is invariant, just like atomic time and exactly 19 seconds behind TAI, as the UTC time-scale was back in 1980, January 6th.

The GPS time system is often used in second format since the start of the epoch $t_{TGPS,s}$. This format is utilized to process GPS measurements or the GPS broadcast ephemerides. $t_{TGPS,s}$ is defined as number of seconds since the 0th GPS epoch 1980, January 6, 00:00:00 UTC [68]:

$$t_{TGPS,s} = t_{TGPS} - t_{TGPS,0} \tag{2.3}$$

where $t_{TGPS,s}$ is the number of seconds between the reference date in GPS t_{TGPS} and the 0th GPS time epoch $t_{TGPS,0}$.

In 1972, the UTC time was set to be 10 seconds behind atomic time TAI. The leap seconds added since then increase the gap and in 2022, UTC is 37 seconds behind TAI.

GMST - Greenwich Mean Sidereal Time θ_{GMST} represents the angle between the mean vernal equinox of date and the Greenwich Meridian. θ_{GMST} can be expressed for a general time of day using:

$$\theta_{GMST} = 67310.54841 + (876000 + 8640184.812866)T_{UT1} + 0.093104T_{UT1}^2 - 6.2 \cdot 10^{-6}T_{UT1}^3 \tag{2.4}$$

Where T_{UT1} are the Julian centuries since 2000, January 1, 12:00:00 at the current UT1 time.

$$T_{UT1} = \frac{t_{JD,UT1} - 2451545}{36525} \tag{2.5}$$

Julian Date Julian Date (JD) is measured in days since January 1, 4713 B.C., 12:00. It generally implies being based on UT1. When provided a date in the format yr:mo:d, h:min:s is calculated using:

$$t_{JD} = 367 - \left(\frac{7(n_{yr} + (\frac{n_{mo}+9}{12})_{int}}{4}\right)_{int} + \left(\frac{275n_{mo}}{9}\right)_{int} + n_d + 1721013.5 + \frac{\frac{n_s/60+n_{min}}{60} + n_{hr}}{24} \tag{2.6}$$

where t_{JD} is the Julian date, subscript int refers to integer truncation of the float number, and n_{yr}, n_{mo}, n_d are the integer values for number of years, months and days of the reference date. Similarly, n_{hr}, n_{min}, n_s are integer values for hours, minutes and seconds of the reference time.

Another used form is the Modified Julian Date (MJD), expressed as:

$$t_{MJD} = t_{JD} - 2400000.5 \tag{2.7}$$

some commonly used Julian date epochs are as follows:

Table 2.1: Commonly used Julian Dates and their respective epochs and dates [68].

Epoch	Julian Date	Date, time system
0th GPS Epoch	2444244.5	January 6, 1980, 00:00:00, UTC
J2000	2451545.0	January 1, 2000, 12:00:00, TT
J1900	2415021.0	January 1, 1900, 12:00:00, UT1

UT - Universal Time Universal time aims to achieve a constant average solar day length of 24 hours. However, the length of one second is not constant, as it depends on the apparent movement of the Sun and Earth's rotation, The offset between UT1 and TAI is published by the International Earth Rotation Services (IERS) in Bulletin B.

2.2. Reference Frames

In this section, the relevant reference frames and transformations between them will be documented. All of the used reference frames are cartesian, right-handed frames.

2.2.1. Vehicle-carried Frames

RSW - Radial, Along-track, Cross-track Frame

The RSW frame aligned with the orbital track and the NTW frame aligned with the velocity vector are shown in Figure 2.1. Although both of these frames coincide with the satellite's orbital position, they do differ slightly. The RSW frame has its R axis aligned with the geocentric position vector, S is normal to the radial vector and generally not exactly coinciding with the velocity vector. In contrast, the NTW system has its T axis parallel to the velocity vector and is therefore not aligned with the radius vector [68]. The subsequent frames will be expressed with respect to the RSW frame.

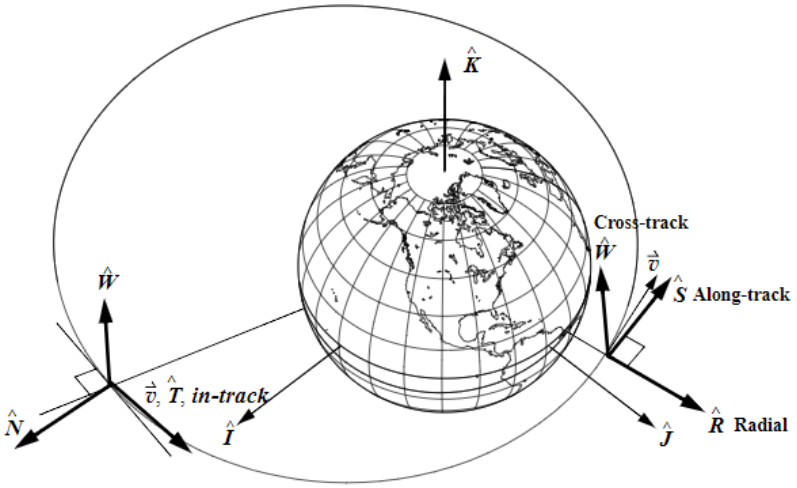

Figure 2.1: [68] RSW and NTW frames.

LF - Laser Communication Terminal Frame

The implementation of the LCT frame (LF) in 4 separate orientations with respect to the satellite's body and the RSW frame are shown in the left of Figure 2.2. It is important to note, that it is assumed that the satellite's body-frame coincides with the RSW frame. Thus, in the simulation, the terminals are effectively on the Earth-facing side of the satellite.

Each LCT frame is very similar and only differ in minor translational and rotational terms. The rotation varies for the X/Y axes with respect to the satellite's flight direction, with frames LF1 and LF3 having the X axes parallel to the flight direction and LF2/4 - perpendicular to the flight direction. The translational terms depend on the satellite's bus dimensions and exact placement of each terminal. In this case, it was assumed that they are symmetrically spaced out in each corner of the Earth-facing side of a 3-unit cubesat.

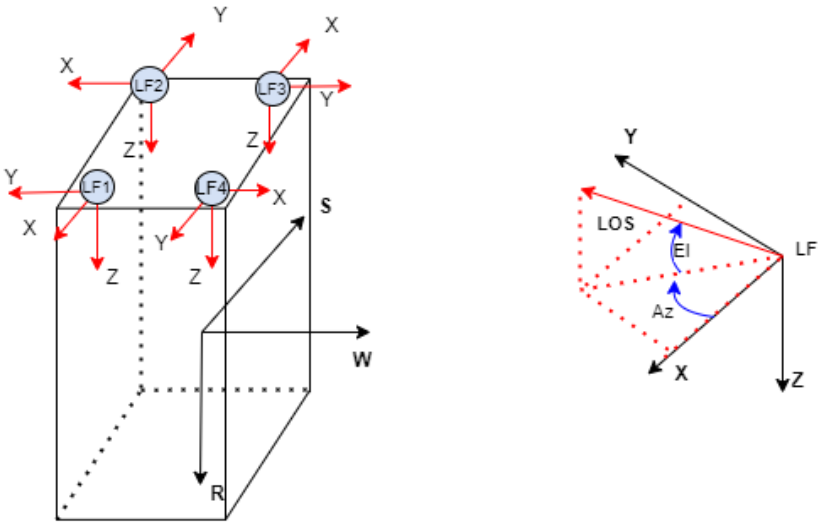

Figure 2.2: (left) LCT frames 1-4 shown on a cubesat bus with the RSW frame coinciding with its geometrical center, (right) Azimuth and Elevation angle conventions for a LOS in the LCT frame.

2.2.2. Earth-Centered Frames

ECI- J2000

The first frame to define is the International Celestial Reference frame (ICRF). An Inertial frame is generally most convenient to formulate the Equations of Motion (EOM) and determining the positions of other bodies, such as Sun or the Moon.

The Earth-Centered Inertial (ECI) reference frame is an ICRF defined at the center of Earth. As shown in Figure 2.3, the axis I point towards the Vernal equinox, J is rotated 90 degrees East and K goes through the North pole, while the origin is at the center of Earth, A very commonly used realization of the ECI is the *J2000*, which is an Earth-Centered (quasi) Inertial reference frame at 2000, January 1, 12:00:00. It is based on the IAU-76 system, where the motion of the equinox and equator are modelled with the IAU-1976 Procession model and the IAU-1980 Theory of Nutation. J2000 will subsequently be referred to as ECI.

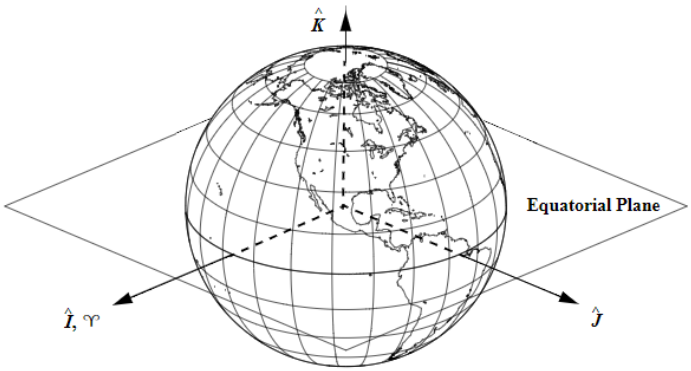

Figure 2.3: Axes of the Earth Centered Inertial reference frames [68].

ECEF- WGS84

The International Terrestrial Reference Frame (ITRF) is another geocentric coordinate system, that rotates with Earth. It is commonly referred to as the ECEF coordinate frame. The ITRF is most convenient when computing the Earth gravitational attraction or processing GPS satellite ephemerides. However, when formulating EOM in ITRF, additional accelerations must be considered due to the rotating nature of the frame. Namely, these are the Coriolis and Centrifugal accelerations.

A commonly used realisation is the World Geodetic System *WGS-84*, which is used by GPS [36] and matches to the ITRF within a few centimeters. ECEF will be used to refer to *WGS-84*.

Conversions between the ECI and ECEF frames require the use of Earth Observation Parameters (EOP), provided by the IERS. Namely, these models are needed:

- Precession, describing the secular change in Earth's rotation axis and equinox, mainly caused by Luni-solar torques
- Nutation, which describes the short-term periodic variation of the equator and the vernal equinox, mainly caused by Luni-solar torques
- Sidereal Time, related to Universal Time and describing Earth's rotation about its axis
- Polar Motion. The coordinates of Earth's pole relative to the IERS reference pole.

2.2.3. Frame Transformation

ECEF to ECI

Basic Rotations The rotations by an angle β around the 3 principal axes are listed below:

$$ROT_1(\beta) = \begin{bmatrix} 1 & 0 & 0 \\ 0 & cos(\beta) & -sin(\beta) \\ 0 & sin(\beta) & cos(\beta) \end{bmatrix} \tag{2.8}$$

$$ROT_2(\beta) = \begin{bmatrix} cos(\beta) & 0 & sin(\beta) \\ 0 & 1 & 0 \\ -sin(\beta) & 0 & cos(\beta) \end{bmatrix} \tag{2.9}$$

$$ROT_3(\beta) = \begin{bmatrix} cos(\beta) & -sin(\beta) & 0 \\ sin(\beta) & cos(\beta) & 0 \\ 0 & 0 & 1 \end{bmatrix} \tag{2.10}$$

Transformation Background Multiple effects must be taken into account to convert from ECEF to ECI. Besides Earth's rotation, the effects of gravitational forces from other planets have an impact on Earth's orientation. The gravitational attraction of the Sun and the Moon on Earth's equatorial bulge lead to a very small torque on Earth, causing smooth long period wobbling of Earth, which is referred to as luni-solar precession. An additional torque on the bulge from the Moon causes nutations- small oscillations in Earth's rotation axis, causing monthly variations. All of these effects cause variations in the orientation of Earth's rotations axis, ecliptic plane, which also leads to motion of the equinox [68].

These effects are taken into account when transforming from ECEF to ECI by using multiple rotations. The complete transformation is:

$$\boldsymbol{r}^{ECI} = PN(t)\Omega(t)\Pi(t)\boldsymbol{r}^{ECEF} \tag{2.11}$$

where PN is the matrix product of the Precession and Nutation matrices, Ω is the sidereal-rotation matrix of date and Π is the Polar Motion rotation matrix of date. The transformation follows the International Astronomical Union (IAU)-2000 theory.

Precession and Nutation The PN matrix is used to relate the Celestial Intermediate Pole (axis of Earth's rotation, normal to the true equator) to the ECI [68]. It is expressed as:

$$PN = \begin{bmatrix} 1 - a_P X_P^2 & -a_P X_P Y_P & X_P \\ -a_P X_P Y_P & 1 - a_P Y_P^2 & Y \\ -X_P & -Y_P & 1 - a_P(X_P^2 + Y_P^2) \end{bmatrix} ROT_3(s_N) \tag{2.12}$$

where $a = 0.5 + 1/8(X_P^2 + Y_P^2)$ and X_P, Y_P are the y and x coordinates of the Celestial Intermediate Pole w.r.t. ECI. Lengthy expressions are used to calculate X_P, Y_P, s_N requiring Terrestrial Time, Mean anomalies, Heliocentric longitudes, right ascensions of the ascending nodes, mean elongation, from the Sun and the Moon, expressed in [68]. Additional corrections include the free-core Nutation and time dependent effects (available as part of EOP).

Sidereal Time Rotation The sidereal time rotation uses the Earth rotation angle θ_{ERA}:

$$\Omega(t) = ROT_3(-\theta_{ERA}) \tag{2.13}$$

where θ_{ERA} is the Earth Rotation Angle, calculated as a function of the Julian Centuries since 2000 of UT1 time:

$$\theta_{ERA} = 2\pi(0.7790572732640 + 1.00273781191135448(JD(UT_1) - 2451645)) \tag{2.14}$$

Polar Motion Rotation The Polar Motion (PM) rotation accounts for the movement of Earth's rotation axis w.r.t. Earth's crust. To account for this rotation, angles are needed from EOP, which are published by the International IERS. The displacements x_p and y_p are given in arc seconds.

Additionally in IAU-2006/2000 conventions, it is needed to take into account the instantaneous prime meridian locator s'. The complete PM rotation is:

$$\Pi(t) = ROT_3(-s')ROT_2(x_p)ROT_1(y_p) \tag{2.15}$$

where s' is the aforementioned prime meridian locator, which is found using average values for Chandler and annual wobble [68] and can be calculated using TT:

$$s' = -0.000047\text{"}TT \tag{2.16}$$

Impact on Accelerations in ECEF
When expressing accelerations in a rotating reference frame, it is important to consider the effects of the rotation vector on the acceleration terms. Additional terms introduced when a rotating frame is used are as follows [68]:

$$\ddot{\boldsymbol{r}}_{ECEF} = \ddot{\boldsymbol{r}}_{ECI} - \dot{\boldsymbol{\omega}}_E \times \boldsymbol{r}_{ECEF} - 2\boldsymbol{\omega}_E \times \dot{\boldsymbol{r}}_{ECEF} - \boldsymbol{\omega}_E \times (\boldsymbol{\omega}_E \times \boldsymbol{r}_{ECEF}) \tag{2.17}$$

where the first term is the acceleration in an inertial frame, second is the tangential acceleration due to the changing rotation rate (and is 0 for circular orbits), the third is the Coriolis acceleration and the final is the centripetal acceleration [68]. Here, $\boldsymbol{\omega}_E$ is the rotation rate vector of ECEF w.r.t. ECI, $\ddot{\boldsymbol{r}}_{ECI}$ is the acceleration in ECI.

It is not necessary to rigorously evaluate the ECI-ECEF transformation and its time derivative and instead it is sufficient to consider a simplified expression for the Coriolis and centripetal accelerations. An approximate rotation vector can be used, along with the Polar Motion rotation of the Z axis, which improves the modelling accuracy of the Coriolis force by one order of magnitude [38]. The rotation vector is expressed as:

$$\boldsymbol{\omega}_E \approx \Pi(t) \begin{pmatrix} 0 \\ 0 \\ \omega_E \end{pmatrix} \tag{2.18}$$

where ω_E is a scalar Earth rotational velocity, equal to 7.292115e-5 rad/s.

2.3. Link Geometry Calculations

Earth occultation condition computations are documented in subsection 2.3.1. Subsequently, conversion of satellite positions to pointing angles are described in subsection 2.3.2.

2.3.1. Link Visibility Conditions

The link distances or viewing angles supported by the terminal are not always the limiting visibility factor- Earth Occultation can also prevent links. To determine whether two satellites are visible to each other, several angles must be established in the satellites' relative geometry. These are visualized in Figure 2.4 [73]. Namely, these angles are:

- ρ_h - Earth's angular radius as seen from the higher-orbit satellite.
- ρ_l - Earth's angular radius as seen from the lower-orbit satellite.
- λ_0 and λ_h - Earth central angles at occultation and transit edges.

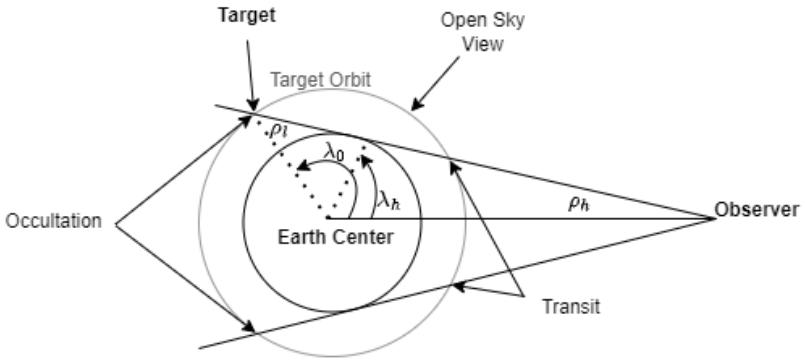

Figure 2.4: Geometry and relevant angles between the LEO and MEO satellites to determine if occultation occurs [73].

The occultation conditions can be derived from multiple points of view. As seen from the higher spacecraft, occultation occurs if:

$$\eta_h < \rho_h \qquad \text{and} \qquad ||\boldsymbol{\rho}|| > ||\boldsymbol{r}|| cos\rho_h \tag{2.19}$$

where η_h is the angle between the nadir vector and the line of sight $\boldsymbol{\rho}$ between the LEO and MEO satellites from the MEO satellite's point of view. From the LEO satellite's point of view, occultation conditions are:

$$\eta_l < \rho_l \tag{2.20}$$

where η_l is the angle between the nadir vector and the line of sight $\boldsymbol{\rho}$ between the LEO and MEO satellites from the LEO satellite's point of view. Conversely, the condition for link availability becomes the opposite condition, that the relative nadir-LOS angle is more or equal to Earth's angular radius:

$$\eta_l \geq \rho_l \tag{2.21}$$

These angles can be computed using the satellite position vectors in an Earth-centered frame and the orbital parameters. Earth's angular radius from a LEO or MEO satellite is calculated using:

$$\rho_h = sin^{-1}\left(\frac{R_E + R_{atm}}{||\boldsymbol{r}_h||}\right) \tag{2.22}$$

where R_E is Earth's radius and R_{atm} is the altitude up to which the atmospheric distortion hinders LISL. $||\boldsymbol{r}_h||$ refers to the higher satellite's orbital radius.

Meanwhile, the angles η_h or η_l are calculated using their Earth-centered position vectors and the dot product rule:

$$\eta_h = cos^{-1}\left(\frac{\boldsymbol{r}_h \cdot \boldsymbol{\rho}_{lh}}{||\boldsymbol{r}_h|| \cdot ||\boldsymbol{\rho}_{lh}||}\right) = cos^{-1}\left(\frac{\boldsymbol{r}_h \cdot (\boldsymbol{r}_h - \boldsymbol{r}_l)}{||\boldsymbol{r}_h|| \cdot ||(\boldsymbol{r}_h - \boldsymbol{r}_l)||}\right) \tag{2.23}$$

analogously, from the lower satellite:

$$\eta_l = cos^{-1}\left(\frac{\boldsymbol{r}_l \cdot \boldsymbol{\rho}_{hl}}{||\boldsymbol{r}_l|| \cdot ||\boldsymbol{\rho}_{hl}||}\right) = cos^{-1}\left(\frac{\boldsymbol{r}_l \cdot (\boldsymbol{r}_l - \boldsymbol{r}_h)}{||\boldsymbol{r}_l|| \cdot ||(\boldsymbol{r}_l - \boldsymbol{r}_h)||}\right) \tag{2.24}$$

2.3.2. Pointing Angle Computations

The Terminal pointing angles are computed by using the host/target satellites' cartesian positions and host satellites attitude. For this analysis, the start point is set at Host and Target position knowledge in the ECI reference frame. These are converted into a LOS by subtracting the target and host position vectors:

$$\boldsymbol{LOS}_{ECI} = \boldsymbol{r}_t - \boldsymbol{r}_h \tag{2.25}$$

The LOS in ECI is then rotated to the satellite body-frame, which in this case is assumed to coincide with the RSW reference frame. The LOS in RSW is calculated by using the rotation matrix from ECI to RSW:

$$\boldsymbol{LOS}_{RSW} = \boldsymbol{ROT}^{RSW/ECI}\boldsymbol{LOS}_{ECI} \tag{2.26}$$

where the rotation matrix $\boldsymbol{ROT}^{RSW/ECI}$ is calculated using the RSW unit vectors expressed in ECI[68]:

$$\boldsymbol{ROT}^{RSW/ECI} = \begin{bmatrix} \hat{R} \\ \hat{S} \\ \hat{W} \end{bmatrix} \tag{2.27}$$

where $\hat{R}$, $\hat{S}$, $\hat{W}$ are the unit vectors in the Radial, Along-track and Cross-track directions. They are calculated using host position and velocity unit vectors via the vector formulation:

$$\hat{R} = \hat{\boldsymbol{r}}_{h,ECI} \tag{2.28}$$

$$\hat{W} = \hat{\boldsymbol{r}}_{h,ECI} \times \hat{\boldsymbol{v}}_{h,ECI} \tag{2.29}$$

$$\hat{S} = \hat{W} \times \hat{R} \tag{2.30}$$

If spacecraft attitude was considered, then $\boldsymbol{ROT}^{BF/ECI}$ would relate ECI and satellite BF reference frames. In this case, the LOS in RSW is assumed to be equivalent to BF.

The Pointing angles of azimuth and elevation are then calculated by converting LCT cartesian components to Azimuth and Elevation $\boldsymbol{AE}$:

$$\boldsymbol{AE} = \begin{bmatrix} arctan2\left(-z_{BF}, y_{BF}\right) \\ arcsin\left(\frac{x_{BF}}{||\boldsymbol{LOS}||}\right) \end{bmatrix} \tag{2.31}$$

where $arctan2$ is the arctan that outputs angles in a 360 degree range and $||\boldsymbol{LOS}||$ is the l-2 norm of the LOS, which effectively is the slant range.

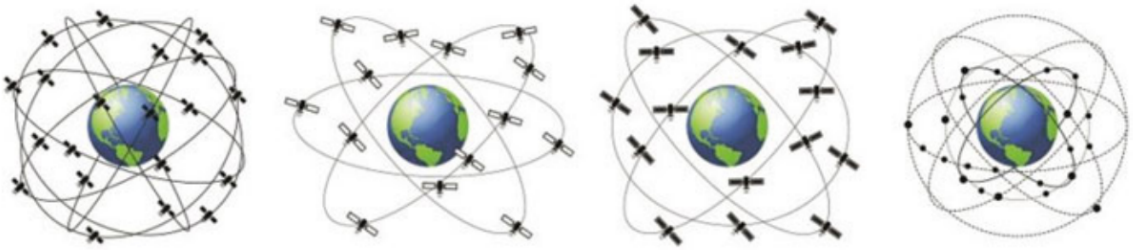

Figure 2.5: Visualization of GNSS Constellations - GPS, Galileo, GLONASS and BeiDou, respectively [44]

2.4. GNSS Background

In this section, some background regarding GNSS constellations and signals is documented in subsection 2.4.1 and subsection 2.4.2, respectively. Then, basics of GNSS-based orbit determination is documented in subsection 2.4.3.

2.4.1. GNSS Constellations

A Global Navigation Satellite System is a constellation of satellites in Medium, Geosynchronous or Geostationary orbits that transmit ranging measurements for navigation purposes. Currently there are multiple operational or near-operational GNSS. Global Positioning System (GPS) is a GNSS operated by the United States, consisting of 24 satellites in Medium Earth Orbit (MEO), which was the first fully operational GNSS. The second one was GLONASS, developed by the Russian federation, currently also consisting of 24 satellites. Galileo- the European global navigation satellite system was designed based on the same physical principles as GPS, GLONASS and other GNSS, where high-precision clocks in orbit are used as a source for radio signal based ranging measurements. BeiDou is the Chinese satellite navigation [66], with three generations of satellites launched between 2000 and 2020.

Although BeiDou provided limited coverage starting in 2000, since then its second and third-generation systems BDS-2 in 2012 and BDS-3 in 2020 has improved it both in coverage and performance. Since 2019, the BeiDou system provides free Precise Point Positioning (PPP) services in dm-level precision [72].

The shells of the GNSS constellations are visualized in Figure 2.5. Their orbital parameters are summarized in Table 2.2, Consistently, each GNSS plane is medium-inclined to provide optimum coverage for the most densely populated regions.

Table 2.2: General characteristics of each GNSS Constellation [44].

GNSS	h [km]	Orbital Period [hr:min]	i [deg]	Nr. Planes [-]
GPS	20200	11:58	55	6
GLONASS	23222	14	56	3
Galileo	19100	11:15	64.8	3
BeiDou	38300; 21500	-	55	6

2.4.2. GNSS Signals

GNSS signals are electromagnetic waves in the radio frequency spectrum. GPS satellites have oscillators on board which generate the fundamental frequency f_0. The carrier signals in the L-band are generated by integer multiplication of f_0. The carrier waves are between 1.2 and 1.6 GHz (L-band), which results in wavelengths of 19-25 cm. Signals are generally provided in SF or DF which allows to compensate ionospheric delays.

The data is encoded in values of +1 and -1, which represents the binary values 0 and 1. Biphase modulation is used, where the carrier wave phase shifts by 180° as the code changes values between +1 and -1, which is shown in Figure 2.6 [21]. The components of the general GPS satellite signals are as follows:

- **Carriers L1 and L2**, transmitted at frequencies $154 f_0$ (1575.42 MHz) and $120 f_0$ (1227.6 MHz).

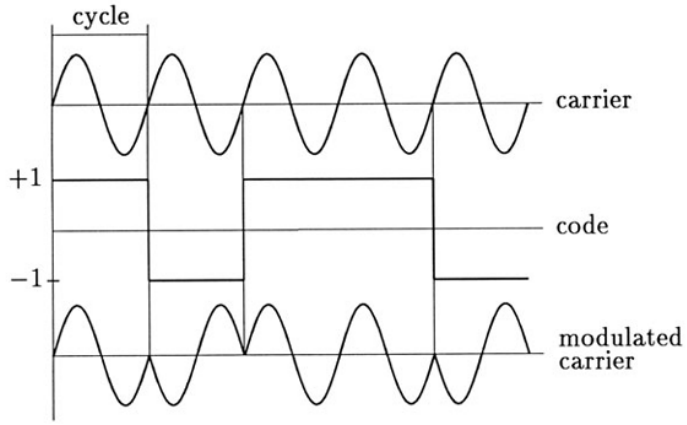

Figure 2.6: Visualization of biphase modulation of carrier wave [21]

- **W-code**, transmitted at $f_0/20$ (0.5115 MHz). This is the encryption code. The modulo 2 sum of P-code and W-code results in the Y-code. This is done to deny access to the P-code to unauthorized users.
- **Precision/protected P-code**, transmitted at f_0. Modulated on both L1 and L2. It is encrypted to the Y-code and is only accessible when the secret conversion algorithm is available.
- **Coarse-Acquisition C/A-code**, transmitted at $f_0/10$ (1.023 MHz). Modulated on L1 using phase quadrature technique with the P-code. This code is available for civilian uses.
- **Navigation message**, transmitted at $f_0/204600$ (50e-6 MHz). The message contains information about satellite health, clock, orbit, and other correction data.

The modulated carriers are represented by Equation 2.32 and Equation 2.33 [21]:

$$L1(t) = A_1 PC(t) WC(t) DC(t) cos(f_1 t) + a_1 C/A(t) DC(t) sin(f_1 t) \tag{2.32}$$

$$L2(t) = A_2 PC(t) WC(t) DC(t) cos(f_2 t) \tag{2.33}$$

where the unmodulated carriers are denoted as $L_i(t) = aicos(f_i t)$ and the sequences of the P-code, C/A-code, W-code and navigation messages are $PC(t)$, $C/A(t)$, $WC(t)$ and $DC(t)$ respectively.

The C/A-code and P-code are characterized by a Pseudorandom Noise (PRN) sequence. These sequences are different for each satellite and has a higher bitrate than the messages. The receivers require the PRN code to access the message data.

By now, a wider range of carrier frequencies are utilized. GPS also offers L5 at 1176.46 MHz. Galileo provides signals at E1, E5a, E5b and E6, also within the L-band of frequencies. The same is true for GLONASS, which has its L-band signals labelled as G1-G3 and BeiDou with B1-B3 [44].

The complete pseudorange is modelled as:

$$Y = d - c(dt_r - dt^s) + d_I + d_T + c(d_r + d^s) + p_T + \epsilon_{mp} + \epsilon_n \tag{2.34}$$

where d is the geometric distance between receiver antenna and transmitting antenna at transmission epoch, dt^s and dt_r are the GNSS satellite and receiver clock errors w.r.t. a reference time system, d_I and d_T are ionospheric and tropospheric delays, while d_r and d^s are receiver and satellite specific group delays. The remaining terms p_T, ϵ_{mp} and ϵ_n are loop transient errors, multipath errors and tracking noise [66].

It is important to mention that when processed in a rotating reference frame (eg. ECEF), the pseudorange observation equation changes due to the frame rotation that occurs during the signal travel time, which affects the geometrical distance d between the Navigation satellite and the receiver. While in ECI, the geometrical distance is simply:

$$d = ||\boldsymbol{r}_r(t_r) - \boldsymbol{r}^s(t_s)|| \tag{2.35}$$

where t_r and t^s correspond to signal receiving time and signal transmission time. When the receiver and transmitting space vehicle's positions are in ECEF, the geometrical distance then includes the Sagnac term:

$$d = ||\boldsymbol{r}_r(t_r) - \boldsymbol{r}^s(t_s)|| + \frac{\omega_e}{c}\left(x^s y_r - y^s x_r\right) \tag{2.36}$$

where ω_e is the scalar Earth rotational velocity term and x; y are the receiver's or GNSS Space Vehicle (SV) cartesian position components in ECEF.

The Carrier Phase is modelled as:

$$L = B + d - c(dt_r - dt^s) - d_I + d_T + c(d_r + d^s) + p_{T'} + \epsilon_{mp'} + \epsilon_{n'} \tag{2.37}$$

which is similar to Equation 2.34, except the Ionospheric delay is now subtracted and the Carrier Phase (CP) ambiguity B is added As previously mentioned, the ionospheric delays can be countered by considering linear combinations of the basic measurements, such as [38]:

$$Y_{P12} = 2.54Y_{P1} - 1.54Y_{P2} \tag{2.38}$$

$$Y_{L12} = 2.54Y_{L1} - 1.54Y_{L2} \tag{2.39}$$

where Equation 2.38 combined dual-frequency pseudorange measurements and Equation 2.39 combined the L1/L2 CP. Both of these combinations required DF GPS measurements. In contrast, Group And Phase Ionospheric Correction (GRAPHIC) requires only Single-Frequency (SF) measurements and is shown in Equation 2.40 [69]:

$$Y_{C1L1} = \frac{Y_{C/A} + Y_{L1}}{2} \tag{2.40}$$

2.4.3. GNSS-based OD Method Basics

A key step in recursive orbit estimation process is the prediction step. An accurate prediction in turn requires a precise dynamical model that can describe the satellite motion. However, if GPS-based techniques are used, approaches that do not require dynamical models are also an option [62]. Generally, 3 OD approaches can be identified:

1. Kinematic approaches, where the orbit is described using only geometry and no forces are taken into account. Zero-difference (ZD) kinematic OD requires highly accurate GNSS satellite and clock products, but in turn is simple and reliable. In contrast, Double-difference (DD) kinematic OD is independent of the accurate GNSS products, but requires estimating the DD ambiguity parameters, thus requiring to process large numbers of observations.
2. Dynamic approach, where the orbit is propagated by modelling all relevant forces. Similarly as in the kinematic approaches, ZD and DD methods can be applied. The ZD dynamic OD also requires the highly accurate products, while DD dynamic OD does not require the precise products, but the DD ambiguities and orbital parameters do need to be estimated.
3. Reduced Dynamic approach, where the forces taken into account are limited and environment models are truncated in order to ease the computational loads.

In Dynamic and Reduced Dynamic OD (DOD, RDOD), the approaches rely on Dynamical Models (DM), meaning the orbit solution shown in Equation 2.41 is required [62]:

$$\ddot{\boldsymbol{r}} = -\mu_E \frac{\boldsymbol{r}}{r^3} + \boldsymbol{a}_p(t, \boldsymbol{r}, \dot{\boldsymbol{r}}, q) = \boldsymbol{a}_{pmg} + \boldsymbol{a}_{pert} \tag{2.41}$$

where

- $\boldsymbol{r}$ is the satellite position
- $\dot{\boldsymbol{r}}$ is the satellite velocity
- $\ddot{\boldsymbol{r}}$ is the satellite acceleration
- t is the dynamic time
- μ_E is Earth's gravitational parameter
- $\boldsymbol{a}_{pmg}$ is the central body point-mass gravitational acceleration
- $\boldsymbol{a}_{pert}$ are perturbing acceleration terms

- q are dynamical Earth orbit parameters

The Equations of Motion (EOM) are then integrated numerically in order to obtain the orbital position and velocity.

In circumstances such as on-board applications, computational resources are limited and therefore the dynamical model must be simplified, which leads to the RDOD approach. In this case, the simplified dynamical model is usually combined with GNSS measurements using a recursive filter, such as the Extended Kalman Filter. In this case, tuning of the process and measurement noise becomes a key issue for accurate OD [34]. Additionally, the unmodelled or truncated acceleration terms can be compensated by estimating empirical accelerations as part of the state vector, which can improve the overall accuracy.

An example of this approach is using the following perturbing accelerations: a time-constant, Earth Gravity Model (EGM) 2008 with truncated terms, analytical point mass gravity attractions from Sun and Moon, a simplified Cannonball solar radiation pressure, a drag coefficient with a random walk process and three empirical accelerations [15]. The empirical accelerations are used to compensate for the ignored and simplified perturbing accelerations.

2.5. Dynamical Models

In this section, the relevant perturbing accelerations will be briefly presented. As mentioned in the previous section, the accelerations acting on a satellite can be split into the central body gravitation term $\boldsymbol{a}_{pmg}$ and perturbing accelerations $\boldsymbol{a}_{pert}$. The perturbing accelerations can be further split into several components, which are shown in Equation 2.42 [68]:

$$\ddot{\boldsymbol{r}} = \boldsymbol{a}_{pmg} + \boldsymbol{a}_{pert} = \boldsymbol{a}_{pmg} + \boldsymbol{a}_{nonspherical} + \boldsymbol{a}_{drag} + \boldsymbol{a}_{SRP} + \sum_{i}^{N} \boldsymbol{a}_{3rd,i} + \boldsymbol{a}_{other} \tag{2.42}$$

where $\boldsymbol{a}_{nonspherical}$ refers to the non-spherical central body gravitation terms, $\boldsymbol{a}_{drag}$ is the aerodynamic drag, $\boldsymbol{a}_{SRP}$ is the Solar Radiation Pressure (SRP), $\sum_i^N \boldsymbol{a}_{3rd,i}$ are the point mass gravitation terms from the 3rd bodies and $\boldsymbol{a}_{other}$ refers to the remaining acceleration terms, which are small enough to be neglected, such as 3rd body non-spherical terms, relativistic effects, Earth radiation pressure, etc.

First, the entire central body gravitation will be described in subsection 2.5.1, followed by other perturbing terms: aerodynamic drag in subsection 2.5.2, solar radiation pressure in subsection 2.5.3 and third body gravitational accelerations in subsection 2.5.4

2.5.1. Central Body gravitation

The central body gravitation term consists of the spherical point-mass gravity and the non-spherical terms. The combined effect is often expressed as a gravitational potential *U*:

$$\boldsymbol{a}_{central} = \boldsymbol{a}_{pmg} + \boldsymbol{a}_{nonspherical} = -\frac{\delta U}{\delta \boldsymbol{r}} \tag{2.43}$$

The general central body potential is split into 3 terms:

$$U = U_0 + U_1 + U_2 \tag{2.44}$$

where U is the complete potential, U_0 is the potential leading to the point mass gravitational acceleration, U_1 is the perturbing acceleration characterized by the terms J_d and U_2 is the perturbing potential due to sectoral and tesseral harmonic terms, which are characterized by coefficients $C_{d,o}$ and $S_{d,o}$. The

potential terms are as follows [68]:

$$U_0 = -\frac{\mu_E}{r}$$
$$U_1 = \frac{\mu_E}{r}\sum_{d=2}^{\infty} J_d \left(\frac{R_E}{r}\right) P_{d,0} sin(\phi)$$
$$U_2 = -\frac{\mu_E}{r}\sum_{d=2}^{\infty}\sum_{o=1}^{d} \left(\frac{R_E}{r}\right)^d P_{d,o}(sin(\phi))(C_{d,o}cos(o\lambda) + S_{d,o}sin(o\lambda)) \tag{2.45}$$

here, $P_{d,o}$ are the Legendre polynomials, defined as:

$$P_{d,o}(n) = \frac{(1-n^2)^{o/2}}{2^d!}\frac{d^{d+o}}{dn^{d+o}}(n^2-1)^d \tag{2.46}$$

in this case, the indices d, o refer to the degree and order of the of the gravitational potential terms. The most basic non-spherical gravity field model that can be used includes degree/order terms up to 2/0, which essentially only includes the J_2 term, which accounts for the oblateness of Earth.

2.5.2. Aerodynamic Drag

Mainly relevant at lower altitudes of LEO, the aerodynamic drag acts opposite to the velocity vector. Approximating the satellite as a flat place with surface area A_c, the aerodynamic drag in ECI frame is expressed as [68]:

$$\boldsymbol{a}_{drag}^{ECI} = \frac{1}{2}\left(\frac{C_D A_D}{m}\right)\rho_{atm}||\dot{\boldsymbol{r}}_{rel}^{ECI}||\dot{\boldsymbol{r}}_{rel}^{ECI} \tag{2.47}$$

where $\dot{\boldsymbol{r}}_{rel}^{ECI}$ is the relative velocity of the cross-sectional area of the flat plate with respect to the fluid:

$$\dot{\boldsymbol{r}}_{rel}^{ECI} \approx \dot{\boldsymbol{r}}^{ECI} - \boldsymbol{\omega}_E^{ECI} \times \boldsymbol{r}^{ECI} \tag{2.48}$$

ρ_{atm} is the atmospheric density, C_D is the drag coefficient of the satellite, A_D is the effective surface area, $\boldsymbol{\omega}_E$ is Earth's rotational velocity and m is the mass. In general, it is very challenging to accurately calculate the drag acting on satellite. The effective surface-area depends on the satellite attitude, drag coefficient depends on the flow regime and satellite geometry and the atmospheric density, which is dependant on solar and geomagnetic activity and very difficult to predict.

2.5.3. Solar Radiation Pressure

The Solar Radiation Pressure (SRP) occurs due to the photons transferring momentum to the objects they interact with. When interacting with an object modelled as a flat plate, the SRP acceleration is as follows [68]:

$$\boldsymbol{a}_{SRP} = -\frac{pA_{SRP}}{m}(\hat{\boldsymbol{r}}_{sun}\cdot\hat{\boldsymbol{n}})\left[\left(\frac{2}{3}C_{R,d} + 2C_{R,s}(\hat{\boldsymbol{r}}_{sun}\cdot\hat{\boldsymbol{n}})\right)\hat{\boldsymbol{n}} + (1-C_{R,s})\hat{\boldsymbol{r}}_{sun}\right] \tag{2.49}$$

where C_R refer to coefficients of reflectivity- $C_{R,d}$ due to diffuse reflection and $C_{R,s}$ due to specular reflection. A_{SRP} is the effective SRP area, p is the solar radiation pressure, $\hat{\boldsymbol{r}}_s$ and $\hat{\boldsymbol{n}}$ are unit vectors, former pointing from the spacecraft to the Sun and the latter is the unit normal vector to the illuminated surface.

2.5.4. 3rd Body Gravitation

To take into account the gravitational acceleration from other bodies, a different expression is used than the central body. The accelerations due to each 3rd body (such as Moon or the Sun) is as follows [68]:

$$\boldsymbol{a}_{3rd} = \mu_{3rd}\left(\frac{\boldsymbol{r}_{3rd}-\boldsymbol{r}}{||\boldsymbol{r}_{3rd}-\boldsymbol{r}||} - \frac{\boldsymbol{r}_{3rd}}{||\boldsymbol{r}_{3rd}||^3}\right) \tag{2.50}$$

where $\boldsymbol{r}$ is the distance from the propagated body to the 3rd body, $\boldsymbol{r}_{3rd}$ is the distance from the 3rd body to Earth and μ_{3rd} is the gravitational parameter of the 3rd body.

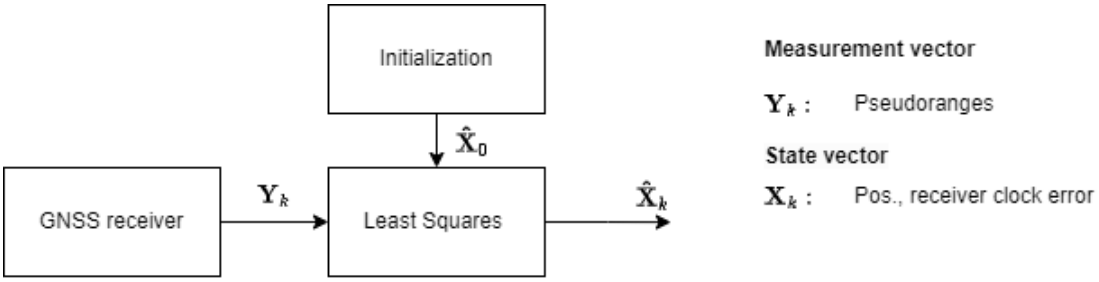

Figure 2.7: General architecture for Single Point Positioning, highlighting the inputs and outputs.

2.6. GNSS-based Orbit Determination

In this section, theoretical formulations of the considered GNSS-based OD are documented. First the most basic kinematic option of Single Point Positioning is shown in subsection 2.6.1. Subsequently two Extended Kalman Filters, using Pseudoranges and Carrier-phase measurements are introduced in subsection 2.6.2 and subsection 2.6.3. Then, after introducing the Unscented Kalman Filter in subsection 2.6.4, the novel Single Propagation Unscented Kalman Filter and the Preprocessing Extended Kalman Filter are described in subsection 2.6.5 and subsection 2.6.6. Finally, a modification to the Preprocessing Extended Kalman filter is proposed in subsection 2.6.7.

2.6.1. Kinematic Single Point Positioning

The kinematic Single Point Positioning (SPP) algorithm is visualized in Figure 2.7. Its benefits are simplicity and ability to provide a position solution without the need to model orbital dynamics and general independence of previous solutions. However, this comes at a cost of accuracy when compared to RDOD options.

This technique can provide a solution once links with 4 navigation satellites are established. The method is based on a least squares estimator to output the position and receiver clock error [30]. It utilizes the basic pseudorange measurement model:

$$Y_i = d_i + cdt_r = |\boldsymbol{r}_i^s - \boldsymbol{r}| + c(dt_r - dt_i^s) \tag{2.51}$$

where Y_i is the pseudorange measurement at a discrete time-step and $\boldsymbol{r}_i^s$ the broadcast position from the ith navigation satellite, dt_r is the receiver clock error and $\boldsymbol{r}$ is the host satellite position.

Using the pseudorange measurements from 4 separate GPS satellites allows to setup the system of equations:

$$\begin{aligned}
Y_1 &= \sqrt{(x_1^s - x)^2 + (y_1^s - y)^2 + (z_1^s - z)^2} + c(dt_r - dt_1^s) \\
Y_2 &= \sqrt{(x_2^s - x)^2 + (y_2^s - y)^2 + (z_2^s - z)^2} + c(dt_r - dt_2^s) \\
Y_3 &= \sqrt{(x_3^s - x)^2 + (y_3^s - y)^2 + (z_3^s - z)^2} + c(dt_r - dt_3^s) \\
Y_4 &= \sqrt{(x_4^s - x)^2 + (y_4^s - y)^2 + (z_4^s - z)^2} + c(dt_r - dt_4^s)
\end{aligned} \tag{2.52}$$

considering that the estimated host position differs from the real position by a small offset:

$$\Delta \boldsymbol{r} = \boldsymbol{r} - \hat{\boldsymbol{r}} \tag{2.53}$$

$$\Delta dt_r = dt_r - \hat{dt_r} \tag{2.54}$$

can be used to linearize and express the pseudorange displacement for the ith navigation satellite:

$$\Delta Y_i = \hat{Y}_i - Y_i = b_{xi}\Delta x + b_{yi}\Delta y + b_{zi}\Delta z - c\Delta dt_r \tag{2.55}$$

where b_{xi}, b_{yi}, b_{zi} are the direction cosines between the host position estimate and the ith navigation satellite. They are expressed as:

$$\begin{aligned} b_{xi} &= \frac{x_i^s - x}{\hat{d}_i} \\ b_{yi} &= \frac{y_i^s - y}{\hat{d}_i} \\ b_{zi} &= \frac{z_i^s - z}{\hat{d}_i} \end{aligned} \tag{2.56}$$

where $\hat{d}_i$ is the current geometrical distance estimate between the navigation satellite and the host satellite.

The system of equations can then be put into matrix form:

$$\Delta \boldsymbol{Y} = \begin{bmatrix} \Delta Y_1 \\ \Delta Y_2 \\ \Delta Y_3 \\ \Delta Y_4 \end{bmatrix} \qquad \Delta \boldsymbol{r} = \begin{bmatrix} \Delta r_1 \\ \Delta r_2 \\ \Delta r_3 \\ -c\Delta dt_r \end{bmatrix} \qquad \Delta \boldsymbol{Y} = H \Delta \boldsymbol{r} \tag{2.57}$$

where H is the observation matrix

$$H = \begin{bmatrix} b_{x1} & b_{y1} & b_{z1} & 1 \\ b_{x2} & b_{y2} & b_{z2} & 1 \\ b_{x3} & b_{y3} & b_{z3} & 1 \\ b_{x4} & b_{y4} & b_{z4} & 1 \end{bmatrix} \tag{2.58}$$

With more than 4 tracked satellites, the problem becomes over-determined. Therefore, the Least Squares method is used to find the solution to minimize the loss function:

$$J(\Delta \boldsymbol{r}) = (\Delta \boldsymbol{Y} - H \Delta \boldsymbol{r})^T (\Delta \boldsymbol{Y} - H \Delta \boldsymbol{r}) \tag{2.59}$$

with the derivative, the expression for the position correction is obtained:

$$\Delta \boldsymbol{r}_0 = (H^T H)^{-1} H^T \Delta \boldsymbol{Y} \tag{2.60}$$

which leads to the position and receiver clock estimate updates:

$$\boldsymbol{r}_j = \boldsymbol{r}_{j-1} - \Delta \boldsymbol{r}_j \tag{2.61}$$

$$dt_{r,j} = dt_{r,j-1} - \Delta dt_{r,j} \tag{2.62}$$

During the procedure, the Navigation satellite-receiver geometry can be inspected, which indicates the quality of the processed position and clock delay solutions. This is done by computing the Geometric Dilution of Precision (GDOP), which is calculated using the $(H^T H)^{-1}$ Matrix product. This is done by taking the square root of the sum of the diagonal entries of $(H^T H)^{-1}$.

A high GDOP indicates that the navigation satellites are spread in a small space, leading to a lower quality solution. In contrast, a low GDOP indicates that the tracked GNSS satellites are spread widely over the receiver's Field of View (FOV), leading to better solutions. In [33], a threshold of 30 was used for the GDOP.

The entire SPP algorithm procedure is as follows:

1. Estimating GNSS satellite positions at the current epoch from the broadcast ephemeris.
2. Compute $\Delta \boldsymbol{Y}$ between the measured and modelled pseudorange with Equation 2.51 and Equation 2.55 from the previous host satellite position estimate.
3. Compute H matrix
4. Compute $\Delta \boldsymbol{r}$
5. Update $\boldsymbol{r}$ and dt_r
6. Iterate from step 2 with new values of $\boldsymbol{r}$ and dt_r until convergence is reached.

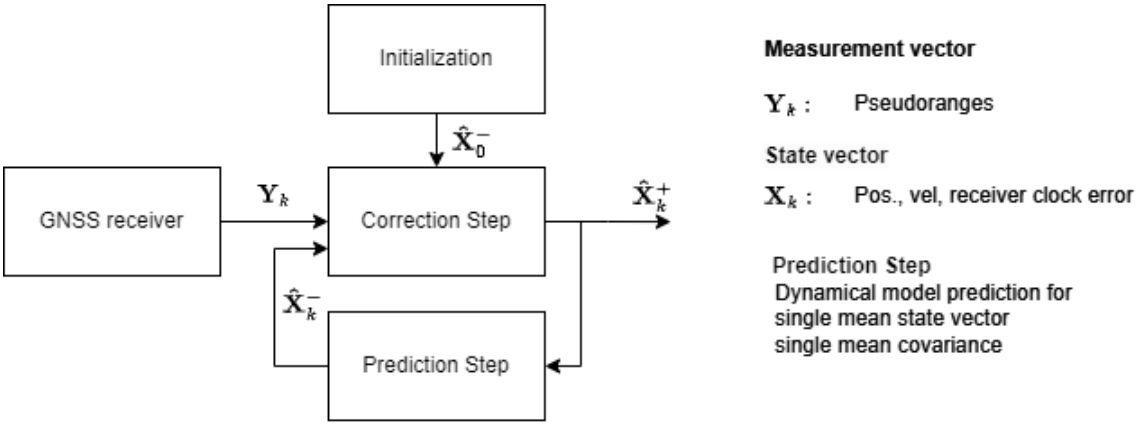

Figure 2.8: General architecture for Extended Kalman Filter utilizing Pseudoranges, highlighting the inputs and outputs.

2.6.2. Extended Kalman Filter using Pseudoranges

The Pseudorange-based Extended Kalman Filter algorithm is visualized in Figure 2.8. Compared to the Kinematic SPP, it includes an additional Prediction Step which utilizes dynamical knowledge of the system, thus adding complexity. It also requires initialization and generally takes a number of iterations until it converges to optimal performance. Finally, it requires tuning of noise matrices, but it does provide an improved precision over the SPP method.

For an in-depth derivation of the EKF, the reader is referred to chapter 10 of [68]. The original KF formulation relies on the differences between the reference and estimated state being small enough to neglect any non-linearities in the system dynamics. The EKF avoids this restriction.

For a nonlinear discrete-time dynamic system with discrete-time measurements and no user inputs, the state derivative is [10]:

$$\dot{\boldsymbol{X}}_k = f(\boldsymbol{X}_k) + w_k,\ w_k \sim N(0, \boldsymbol{Q}_k) \tag{2.63}$$

$$\boldsymbol{Y}_k = h(\boldsymbol{X}_k) + v_k,\ v_k \sim N(0, \boldsymbol{R}_k) \tag{2.64}$$

where $\dot{\boldsymbol{X}}_k$ is the system state, $\dot{\boldsymbol{X}}_k$ is the state time derivative, $\boldsymbol{Y}_k$ is the noisy measurement vector. The process noise is w_k and v_k is the measurement noise, both modelled as zero-mean Gaussian white-noise processes. The process and measurement noise are assumed to be uncorrelated and the errors are uncorrelated forward/backward in time.

The filter involves a prediction and an update step. The state is propagated using the modelled dynamics with the current estimate: The EKF requires F and H matrices, which are the partial derivatives of $f(\boldsymbol{X}_k)$ and $h(\boldsymbol{X}_k)$. The discrete F_k can be obtained by truncating the Taylor series expansion of the continuous time $F(t)$:

$$H_k = \frac{\delta h}{\delta \boldsymbol{X}}(\boldsymbol{X}_k^-) \tag{2.65}$$

$$F_k = I + F(t)(t_s) \tag{2.66}$$

Which is used to predict the covariance matrix

$$\boldsymbol{P}_k^- = F_k \boldsymbol{P}_k^+ F_k^T + Q \tag{2.67}$$

while the state prediction can be performed using the state transition matrix F_k or by utilizing the dynamical model and numerical integration:

$$\hat{\boldsymbol{X}}_k^- = \hat{\boldsymbol{X}}_{k-1}^+ + \int_{t_{k-1}}^{t_k} f(\hat{\boldsymbol{X}}_{k-1}^+)dt \approx \hat{\boldsymbol{X}}_{k-1}^+ + \Delta t f(\hat{\boldsymbol{X}}_{k-1}^+) \tag{2.68}$$

The measurement update steps are as follows. First, the Kalman gain $\boldsymbol{K}^k$ is computed:

$$\boldsymbol{K}^k = \boldsymbol{P}_k^- H_k^T (R^{-1} + H_k \boldsymbol{P}_k^- H_k^T)^{-1} \tag{2.69}$$

which is used for the updated state estimate:

$$\hat{\boldsymbol{X}}_k^+ = \hat{\boldsymbol{X}}_k^- + \boldsymbol{K}^k [\boldsymbol{Y}_k - h(\hat{\boldsymbol{X}}_k^-)] \tag{2.70}$$

and state covariance matrix:

$$\boldsymbol{P}_k^+ = [I - \boldsymbol{K}^k H_k(\hat{\boldsymbol{X}}_k^-)]\boldsymbol{P}_k^- \tag{2.71}$$

where $\boldsymbol{P}_k^+$ is the corrected "a posteriori" error covariance, while $\boldsymbol{P}_k^-$ was the predicted "a priori" error covariance.

Once the filter is initialized with estimates of $\boldsymbol{P}_0^+$, $\hat{\boldsymbol{X}}_0^+$, it can be recursively updated for incoming measurements.

The state vector is defined as:

$$\boldsymbol{X} = [\boldsymbol{r}, \dot{\boldsymbol{r}}, cdt_r]^T \tag{2.72}$$

where $\dot{r}$ is the cartesian velocity. A simplified observation function for pseudoranges is used:

$$\boldsymbol{Y} = |\boldsymbol{r}^s - \boldsymbol{r}| - c(dt_r - dt^s) + \epsilon = d - c(dt - dt^s) + \epsilon = h(\boldsymbol{X}_K) \tag{2.73}$$

The Jacobian F of the dynamical model is required for the filter formulation. Its continuous-time form is defined as:

$$F(t) = \frac{\delta f(X_k)}{\delta X_k} = \begin{bmatrix} \frac{\delta \dot{x}}{\delta x} & \frac{\delta \dot{x}}{\delta y} & \frac{\delta \dot{x}}{\delta z} & \frac{\delta \dot{x}}{\delta \dot{x}} & \frac{\delta \dot{x}}{\delta \dot{y}} & \frac{\delta \dot{x}}{\delta \dot{z}} \\ \frac{\delta \dot{y}}{\delta x} & \frac{\delta \dot{y}}{\delta y} & \frac{\delta \dot{y}}{\delta z} & \frac{\delta \dot{y}}{\delta \dot{x}} & \frac{\delta \dot{y}}{\delta \dot{y}} & \frac{\delta \dot{y}}{\delta \dot{z}} \\ \frac{\delta \dot{z}}{\delta x} & \frac{\delta \dot{z}}{\delta y} & \frac{\delta \dot{z}}{\delta z} & \frac{\delta \dot{z}}{\delta \dot{x}} & \frac{\delta \dot{z}}{\delta \dot{y}} & \frac{\delta \dot{z}}{\delta \dot{z}} \\ \frac{\delta \ddot{x}}{\delta x} & \frac{\delta \ddot{x}}{\delta y} & \frac{\delta \ddot{x}}{\delta z} & \frac{\delta \ddot{x}}{\delta \dot{x}} & \frac{\delta \ddot{x}}{\delta \dot{y}} & \frac{\delta \ddot{x}}{\delta \dot{z}} \\ \frac{\delta \ddot{y}}{\delta x} & \frac{\delta \ddot{y}}{\delta y} & \frac{\delta \ddot{y}}{\delta z} & \frac{\delta \ddot{y}}{\delta \dot{x}} & \frac{\delta \ddot{y}}{\delta \dot{y}} & \frac{\delta \ddot{y}}{\delta \dot{z}} \\ \frac{\delta \ddot{z}}{\delta x} & \frac{\delta \ddot{z}}{\delta y} & \frac{\delta \ddot{z}}{\delta z} & \frac{\delta \ddot{z}}{\delta \dot{x}} & \frac{\delta \ddot{z}}{\delta \dot{y}} & \frac{\delta \ddot{z}}{\delta \dot{z}} \end{bmatrix} = \begin{bmatrix} \frac{\delta \dot{\boldsymbol{r}}}{\delta \boldsymbol{r}} & \frac{\delta \dot{\boldsymbol{r}}}{\delta \dot{\boldsymbol{r}}} \\ \frac{\delta \ddot{\boldsymbol{r}}}{\delta \boldsymbol{r}} & \frac{\delta \ddot{\boldsymbol{r}}}{\delta \dot{\boldsymbol{r}}} \end{bmatrix} \tag{2.74}$$

in which, the following entries can be simplified:

$$\begin{gathered} \frac{\delta \dot{x}}{\delta \dot{x}} = \frac{\delta \dot{y}}{\delta \dot{y}} = \frac{\delta \dot{z}}{\delta \dot{z}} = 1 \\ \frac{\delta \dot{x}}{\delta x} = \frac{\delta \dot{x}}{\delta y} = \frac{\delta \dot{x}}{\delta z} = \frac{\delta \dot{x}}{\delta \dot{y}} = \frac{\delta \dot{x}}{\delta \dot{z}} = 0 \\ \frac{\delta \dot{y}}{\delta x} = \frac{\delta \dot{y}}{\delta y} = \frac{\delta \dot{y}}{\delta z} = \frac{\delta \dot{y}}{\delta \dot{x}} = \frac{\delta \dot{y}}{\delta \dot{z}} = 0 \\ \frac{\delta \dot{z}}{\delta x} = \frac{\delta \dot{z}}{\delta y} = \frac{\delta \dot{z}}{\delta z} = \frac{\delta \dot{z}}{\delta \dot{x}} = \frac{\delta \dot{z}}{\delta \dot{y}} = 0 \end{gathered} \tag{2.75}$$

meaning F can be expressed as:

$$F(t) = \begin{bmatrix} 0_{3\times3} & I_{3\times3} \\ \frac{\delta \ddot{\boldsymbol{r}}}{\delta \boldsymbol{r}} & 0_{3\times3} \end{bmatrix} \tag{2.76}$$

which leads to the discrete state transition matrix $\boldsymbol{\Phi}_r$ by using a matrix exponential:

$$\boldsymbol{\Phi}_r = e^{F\Delta t} \tag{2.77}$$

the observation matrix H with 4 tracking channels is:

$$H_k = \frac{\delta h}{\delta X_k} = \begin{bmatrix} \frac{\delta Y_1}{\delta x} & \frac{\delta Y_1}{\delta y} & \frac{\delta Y_1}{\delta z} & \frac{\delta Y_1}{\delta \dot{x}} & \frac{\delta Y_1}{\delta \dot{y}} & \frac{\delta Y_1}{\delta \dot{z}} & \frac{\delta Y_1}{\delta cdt_r} \\ \frac{\delta Y_2}{\delta x} & \frac{\delta Y_2}{\delta y} & \frac{\delta Y_2}{\delta z} & \frac{\delta Y_2}{\delta \dot{x}} & \frac{\delta Y_2}{\delta \dot{y}} & \frac{\delta Y_2}{\delta \dot{z}} & \frac{\delta Y_2}{\delta cdt_r} \\ \frac{\delta Y_3}{\delta x} & \frac{\delta Y_3}{\delta y} & \frac{\delta Y_3}{\delta z} & \frac{\delta Y_3}{\delta \dot{x}} & \frac{\delta Y_3}{\delta \dot{y}} & \frac{\delta Y_3}{\delta \dot{z}} & \frac{\delta Y_3}{\delta cdt_r} \\ \frac{\delta Y_4}{\delta x} & \frac{\delta Y_4}{\delta y} & \frac{\delta Y_4}{\delta z} & \frac{\delta Y_4}{\delta \dot{x}} & \frac{\delta Y_4}{\delta \dot{y}} & \frac{\delta Y_4}{\delta \dot{z}} & \frac{\delta Y_4}{\delta cdt_r} \end{bmatrix}_{x=x_k^-} \tag{2.78}$$

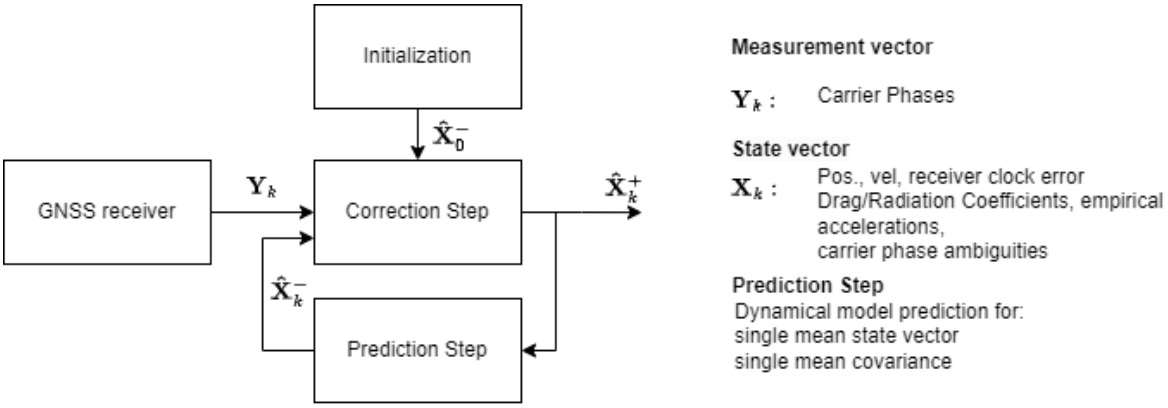

Figure 2.9: General architecture for Extended Kalman Filter utilizing Carrier Phases, highlighting the inputs and outputs.

where

$$\begin{aligned}
\frac{\delta Y_i}{\delta x} &= \frac{x - x_i^s}{\sqrt{(x - x_i^s)^2 + (y - y_i^s)^2 + (z - z_i^s)^2}} \\
\frac{\delta Y_i}{\delta y} &= \frac{y - y_i^s}{\sqrt{(x - x_i^s)^2 + (y - y_i^s)^2 + (z - z_i^s)^2}} \\
\frac{\delta Y_i}{\delta z} &= \frac{z - z_i^s}{\sqrt{(x - x_i^s)^2 + (y - y_i^s)^2 + (z - z_i^s)^2}} \\
\frac{\delta Y_i}{\delta \dot{x}} &= \frac{\delta Y_i}{\delta \dot{y}} = \frac{\delta Y_i}{\delta \dot{z}} = 0 \\
\frac{\delta Y_i}{\delta c dt_r} &= -1
\end{aligned} \tag{2.79}$$

2.6.3. Extended Kalman Filter using Carrier Phases

An EKF utilizing CP measurements is shown in Figure 2.9. While the utilized blocks do not differ from its PR-based formulation shown in Figure 2.9, a stark contrast can be seen in its state vector. In order to utilize CP, which are far more precise than Pseudorange measurements, the correct estimation of various parameters are needed and this in turn requires a broader dynamical model.

The CP-based EKF formulation is a combined approach, based on the documentation of the on-board OD filter in [38] and the novel improvement of using the pseudo-ambiguity parameter in [71].

Using Carrier-Phase measurements, the observation equation is similar to Equation 2.73 but includes the additional CP-ambiguity parameter:

$$Y = d - c(dt - dt^s) + B + \epsilon \tag{2.80}$$

As described in [71], although B is constant in theory, it is problematic to estimate when using broadcast ephemeris, as the satellite clock and computed orbit errors are at meter-level. Therefore, the alternative approach is recommended by first considering a breakdown of the geometrical distance and satellite clock errors.

The geometrical distance and satellite clock errors can be expressed with Equation 2.81 and Equation 2.82, respectively:

$$d_i = d_i^* + \delta d_i \tag{2.81}$$

$$dt_i = dt_i^* + \delta dt_i \tag{2.82}$$

where d_i is the geometrical distance from the receiver to the i^{th} navigation satellite, d_i^* refers to the geometrical distance calculated when using the broadcast ephemeris and δd_i is the errors in the LOS due to broadcast ephemeris errors. Similarly, dt_i is the clock error of the i^{th} satellite, dt_i^* is the clock

offset calculated with broadcast ephemerides and δdt_i is the error of the broadcast ephemeris clock offset. Substituting these parameters into Equation 2.37 leads to:

$$Y = d^* + \delta d - c(dt - dt^* - \delta dt^s) + B + \epsilon \tag{2.83}$$

As it is difficult to estimate the pseudo-ambiguity in presence of the broadcast ephemeris errors, the pseudo-ambiguity parameter is defined:

$$A = B + \delta d + \delta dt^s \tag{2.84}$$

Thus, the state vector is defined as:

$$\boldsymbol{X} = [\boldsymbol{r}, \dot{\boldsymbol{r}}, C_R, C_D, \boldsymbol{a}_e, cdt_r, \boldsymbol{A}]^T \tag{2.85}$$

Compared to Equation 2.72, it contains the following additional states: SRP coefficient C_R, Drag coefficient C_D, empirical accelerations in the radial, along and cross-track directions $\boldsymbol{a}_e$ and the Pseudo-ambiguity parameters $\boldsymbol{A}$ for the tracked navigation satellites.

The complete transition matrix is defined as:

$$\boldsymbol{\Phi} = \frac{\delta \boldsymbol{X}_k}{\delta \boldsymbol{X}_{k-1}} = \begin{pmatrix} \boldsymbol{\Phi}_r & \boldsymbol{S}_{C_R} & \boldsymbol{S}_{C_D} & \boldsymbol{S}_{\boldsymbol{a}} & 0 & 0 \\ 0 & 1 & 0 & 0 & 0 & 0 \\ 0 & 0 & 1 & 0 & 0 & 0 \\ 0 & 0 & 0 & m_e \times \boldsymbol{I}_{3\times 3} & 0 & 0 \\ 0 & 0 & 0 & 0 & 1 & 0 \\ 0 & 0 & 0 & 0 & 0 & \boldsymbol{I}_{n\times n} \end{pmatrix} \tag{2.86}$$

where $\boldsymbol{\Phi}_r$ is the State Transition Matrix (STM), previously shown in Equation 2.77, $\boldsymbol{S}_{C_R}$, $\boldsymbol{S}_{C_D}$, $\boldsymbol{S}_{\boldsymbol{a}}$ are the sensitivity matrices and m_e is the exponential damping factor:

$$m_{e,k} = e^{-|t_k - t_{k-1}|/\tau} \tag{2.87}$$

where τ is the correlation time,

The sensitivity matrices are defined as:

$$\boldsymbol{S}_{(C_R, C_D, \boldsymbol{a})} = \frac{\delta(\boldsymbol{r}, \dot{\boldsymbol{r}})_k}{\delta(C_R, C_D, \boldsymbol{a})_{k-1}} \tag{2.88}$$

and are computed numerically.

The observation Jacobian H is similar to that of the pseudorange model in Equation 2.78, with additional entries due to the augmented state vector. The i^{th} row of observation matrix Jacobian is:

$$H_{k,i} = \frac{\delta h_i}{\delta X_k} = \begin{bmatrix} \frac{\delta Y_i}{\delta \boldsymbol{r}} & \frac{\delta Y_i}{\delta \dot{\boldsymbol{r}}} & \frac{\delta Y_i}{\delta C_R} & \frac{\delta Y_i}{\delta C_D} & \frac{\delta Y_i}{\delta \boldsymbol{a}} & \frac{\delta Y_i}{\delta \boldsymbol{A}} \end{bmatrix} \tag{2.89}$$

where the newly introduced partial derivatives are

$$\begin{aligned} \frac{\delta Y_i}{\delta C_R} &= 0 \\ \frac{\delta Y_i}{\delta C_D} &= 0 \\ \frac{\delta Y_i}{\delta \boldsymbol{a}} &= \boldsymbol{0} \end{aligned} \tag{2.90}$$

and

$$\frac{\delta \boldsymbol{Y}}{\delta \boldsymbol{A}} = \boldsymbol{I} \tag{2.91}$$

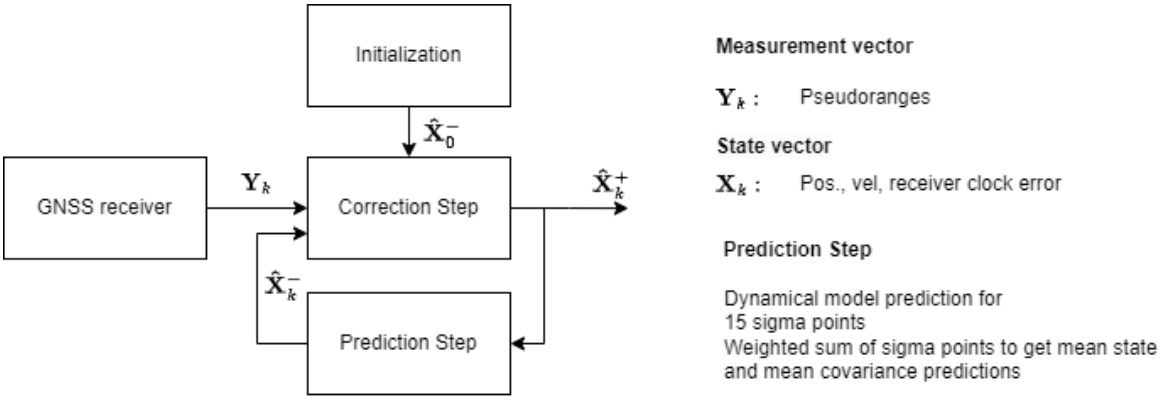

Figure 2.10: General architecture for Unscented Kalman Filter utilizing Pseudoranges, highlighting the inputs and outputs.

2.6.4. Unscented Kalman Filter

A general Unscented Kalman Filter (UKF) formulation architecture is shown in Figure 2.10. While the formulation and state vector does not differ from a pseudorange-based EKF, its key difference is in the prediction and correction step. Rather than predicting based on a single mean state estimate, the UKF makes many separate predictions of sigma points and uses a weighted sum of these points to compute the mean state prediction. When propagating the sigma points through the nonlinear system, the posterior mean and covariance are captured accurately to a 2nd order Taylor-series expansion [9], [28]. The UKF also requires no explicit derivations of the Jacobian or Hessian matrices.

An n-dimensional state vector is approximated using $2n+1$ weighted sigma points χ_i with weights W_i. For an n $\times$ 1 state vector, n $\times$ n covariance and n $\times$ n process noise matrix, the sigma points are computed according to:

$$\chi_{0,k} = \hat{\boldsymbol{X}}_k \tag{2.92}$$

$$\chi_{i,k} = \chi_{0,k} + \Delta\chi_{i,k} \tag{2.93}$$

where $\Delta\chi_{i,k}$ is calculated using Equation 2.94

$$\Delta\chi_{i,k} = \begin{cases} +\left(\sqrt{(n+\lambda)(\hat{\boldsymbol{P}}_k + \boldsymbol{Q}_k)}\right)_i & \text{for } i = 1, ..., n \\ -\left(\sqrt{(n+\lambda)(\hat{\boldsymbol{P}}_k + \boldsymbol{Q}_k)}\right)_{i-n} & \text{for } i = n+1, ..., 2n \end{cases} \tag{2.94}$$

where $\hat{\boldsymbol{x}}_k$ is the mean of the state vector, *i* refers to the column of χ_k and $\lambda = \alpha^2(n+\kappa) - n$ are composite scaling parameters, which determines the scaling of χ_k around $\hat{\boldsymbol{x}}_k$. κ is a secondary scaling parameter and provides an additional degree of freedom to tune the higher-order moments. The transformed sigma vectors are propagated through the nonlinear function:

$$\chi_{i,k+1} = f\left(\chi_{i,k}, k\right) \tag{2.95}$$

The predicted state $\hat{\boldsymbol{X}}_{k+1}^-$ and covariance $\boldsymbol{P}_{k+1}^-$ are computed using the weighted sample mean and covariance of the posterior sigma point vectors:

$$\hat{\boldsymbol{X}}_{k+1}^- = \sum_{i=0}^{2n} W_i^m \chi_{i,k+1} \tag{2.96}$$

$$\boldsymbol{P}_{k+1}^- = \sum_{i=0}^{2n} W_i^c \left(\chi_{i,k+1} - \hat{\boldsymbol{X}}_{k+1}^-\right)\left(\chi_{i,k+1} - \hat{\boldsymbol{X}}_{k+1}^-\right)^T \tag{2.97}$$

$$W_0^m = \frac{\lambda}{n+\lambda} \tag{2.98}$$

$$W_0^c = \frac{\lambda}{n+\lambda} + (1 - \alpha^2 + \beta) \tag{2.99}$$

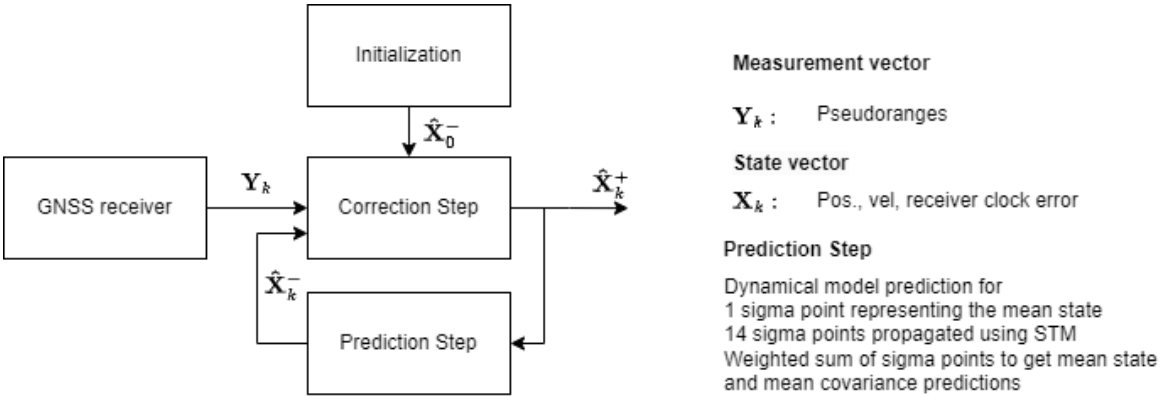

Figure 2.11: General architecture for Single Propagation Unscented Kalman Filter utilizing Pseudoranges, highlighting the inputs and outputs.

$$W_i^m = W_i^c = \frac{1}{2(n+\lambda)} \text{ for } i = 1, ..., 2n \tag{2.100}$$

where W_i^m and W_i^c are the weights for the mean and the covariance associated with the ith sigma point, respectively. β is used to add weighting to the initial sigma point for covariance calculation for higher-order moments. 2 is used for Gaussian distributions.

$\lambda = \alpha^2(n+\kappa) - n$ The observation vector $\hat{\boldsymbol{Y}}_{k+1}^-$ and innovation covariance $\boldsymbol{P}_{k+1}^{yy}$ are predicted in a similar fashion:

$$z_{i,k+1} = h(\chi_{i,k+1}, k+1) \tag{2.101}$$

$$\hat{\boldsymbol{Y}}_{k+1}^- = \sum_{i=0}^{2n} W_i^m z_{i,k+1} \tag{2.102}$$

$$\boldsymbol{P}_{k+1}^{yy} = \sum_{i=0}^{2n} W_i^c \left(z_{i,k+1} - \hat{\boldsymbol{Y}}_{k+1}^-\right)\left(z_{i,k+1} - \hat{\boldsymbol{Y}}_{k+1}^-\right)^T \tag{2.103}$$

The innovation covariance is found using the measurement noise matrix $\boldsymbol{R}_{k+1}$:

$$\boldsymbol{P}_{k+1}^{vv} = \boldsymbol{P}_{k+1}^{yy} + \boldsymbol{R}_{k+1} \tag{2.104}$$

To get the Kalman gain, the cross-correlation matrix between predicted state and prediction observation is needed, which is computed using:

$$\boldsymbol{P}_{k+1}^{xy} = \sum_{i=0}^{2n} W_i^c \left(\chi_{i,k+1} - \hat{\boldsymbol{X}}_{k+1}^-\right)\left(z_{i,k+1} - \hat{\boldsymbol{Y}}_{k+1}^-\right)^T \tag{2.105}$$

$$\boldsymbol{K}^{k+1} = \boldsymbol{P}_{k+1}^{xy}\left(\boldsymbol{P}_{k+1}^{vv}\right)^{-1} \tag{2.106}$$

which finally leads to estimated state and update covariance matrix:

$$\hat{\boldsymbol{X}}_{k+1}^+ = \hat{\boldsymbol{X}}_{k+1}^- + \boldsymbol{K}_{k+1}(\boldsymbol{Y}_{k+1} - \hat{\boldsymbol{Y}}_{k+1}^-) \tag{2.107}$$

$$\boldsymbol{P}_{k+1}^+ = \boldsymbol{P}_{k+1}^- - \boldsymbol{K}_{k+1}\left(\boldsymbol{P}_{k+1}^{yy} + \boldsymbol{R}_{k+1}\right)\boldsymbol{K}_{k+1} \tag{2.108}$$

2.6.5. Single Propagation Unscented Kalman Filter

The Single Propagation Unscented Kalman Filter (SPUKF) architecture is shown in Figure 2.11. It is almost identical to the UKF, except for the prediction step. To reduce the added computational load of the UKF, the SPUKF only performs a full prediction for the sigma point representing the mean state vector, whereas the other sigma points are propagated using a state transition matrix.

The SPUKF formulation follows the algorithm description in [5], except adapted for single-GNSS measurements.

With pseudorange measurements the same observation model is used as in EKF:

$$Y = d - c(dt_r - dt^s) + \epsilon \tag{2.109}$$

The state vector is defined as:

$$\boldsymbol{X} = [\boldsymbol{r}, \dot{\boldsymbol{r}}, cdt_r]^T \tag{2.110}$$

and is then augmented with the process noise terms:

$$\boldsymbol{X}_a = [\boldsymbol{X}, \boldsymbol{Q}]^T \tag{2.111}$$

The error covariance must also be augmented:

$$\boldsymbol{P}_a = \begin{bmatrix} \boldsymbol{P} & \boldsymbol{P}_{XQ} \\ \boldsymbol{P}_{XQ} & \boldsymbol{Q} \end{bmatrix} \tag{2.112}$$

where $\boldsymbol{P}_{XQ}$ is the cross covariance of $\boldsymbol{X}$ and $\boldsymbol{Q}$, $\boldsymbol{P}$ is the error covariance and $\boldsymbol{Q}$ is the process noise covariance matrix.

In the SPUKF, only a single sigma point is propagated, which is:

$$\boldsymbol{\chi}_0 = \boldsymbol{X}_a^+ \tag{2.113}$$

The remaining sigma points are predicted at the next epoch using a Transition Matrix. Therefore, the $0th$ sigma vector is predicted using:

$$\chi_{0,k+1} = f\left(\chi_{0,k}, k\right) \tag{2.114}$$

whereas the remaining sigma vectors are predicted with:

$$\chi_{i,k+1} = \chi_{i,k} + \boldsymbol{\Phi}\Delta\chi i, k \tag{2.115}$$

where the sigma point offset $\Delta\chi i, k$ is calculated according to Equation 2.94 and the STM $\boldsymbol{\Phi}$ is computed in a similar manner as shown for the EKF in Equation 2.77. The same STM is reused for each sigma point.

$$\boldsymbol{\chi}_s^-(t + \Delta t) = \boldsymbol{\chi}_0^-(t + \Delta t) + \boldsymbol{\Phi}\Delta\boldsymbol{\chi}_s \tag{2.116}$$

Where $\Delta\boldsymbol{\chi}_s$ is calculated according to Equation 2.94. The transition matrix is calculated using the matrix exponential of the Jacobian of the system model F:

$$\boldsymbol{\Phi} = e^{F\Delta t} \tag{2.117}$$

where F is the Jacobian of the augmented state:

$$F = \left.\frac{\delta\dot{\boldsymbol{X}}_a}{\delta\boldsymbol{X}_a}\right|_{\boldsymbol{X}_a^+} = \begin{bmatrix} \left.\frac{\delta\dot{\boldsymbol{X}}}{\delta\boldsymbol{X}}\right|_{\boldsymbol{X}^+} & \boldsymbol{0}_{8\times8} \\ \boldsymbol{0}_{8\times8} & \boldsymbol{0}_{8\times8} \end{bmatrix} \tag{2.118}$$

the weighted sum of the predicted sigma points is used to calculate the mean predicted state vector, as was shown in Equation 2.96. The predicted measurements are calculated for the $0th$ sigma vector using the observation equation:

$$z_{i0} = h(\boldsymbol{\chi}_0^-(t + \Delta t)) \tag{2.119}$$

and for the remaining sigma points using Equation 2.120:

$$z_{is} = z_{i0} + \left.\frac{\delta Y_s}{\delta\boldsymbol{X}}\right|_{\boldsymbol{\chi}_s^-(t+\Delta t)} [\boldsymbol{\chi}_s^-(t + \Delta t) - \boldsymbol{\chi}_0^-(t + \Delta t)] \tag{2.120}$$

where i refers to the navigation satellite and s to the sth sigma point.

The remaining steps follow the same procedure as the UKF in Equation 2.96- predicted state and covariances are computed using the weighted means of each sigma point. The same is done for the observation vector and innovation covariance. The cross-correlation is computed using Equation 2.105, leading to the Kalman gain with Equation 2.106 which is used to correct the mean state estimate and state covariance.

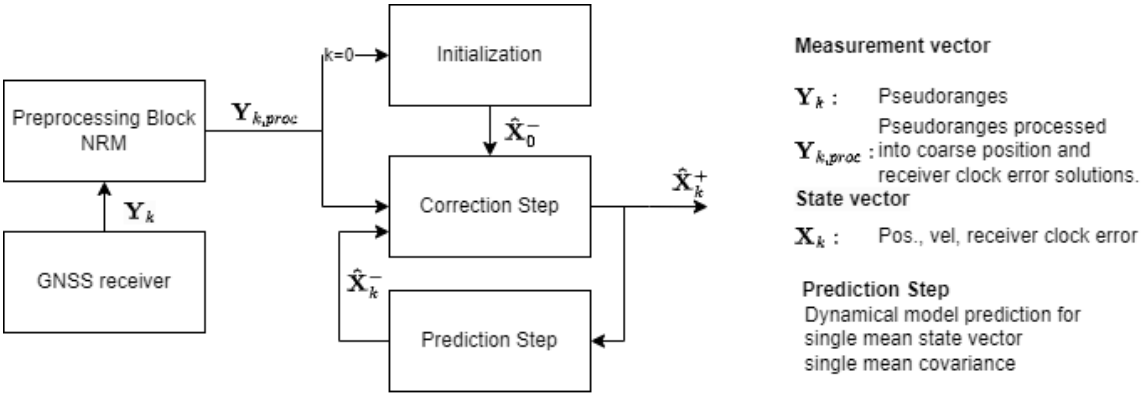

Figure 2.12: General architecture for original Preprocessing Extended Kalman Filter with the NRM.

2.6.6. Newton-Raphson Preprocessing EKF

The original Preprocessing EKF (PEKF) architecture is shown in Figure 2.12. It differs from the EKF as it uses an additional Preprocessing block, which uses a root-solving Newton Raphson Method (NRM) to determine coarse position and receiver clock error solutions from the raw pseudorange inputs. These are then used as measurements inputs for the typical EKF blocks. The coarse position solutions can also be used to initialize the EKF blocks.

The PEKF formulation will be presented according to the original method description in [3] and [4].

Before the EKF blocks are used, the pseudorange measurements are processed into coarse position and receiver clock error solutions. To do so, the simplified observation model is defined:

$$Y_i = d_i + c(dt_r - dt_i^s) + \epsilon = |\boldsymbol{r}^s - \boldsymbol{r}_i| + c(dt_r - dt_i^s) + \epsilon \tag{2.121}$$

where d is the geometrical distance between the receiver and the navigation satellite, i refers to the ith GNSS satellite, dt_r is the receiver clock error and ϵ are the remaining errors. These measurements are converted to coarse position estimates using the preprocessing block. The numerical solution $\boldsymbol{s}$ is sought:

$$\boldsymbol{s} = [x, y, z, cdt_r]^T = [\boldsymbol{r}_c, cdt_r]^T \tag{2.122}$$

which is searched for by minimizing the defined Loss function $\boldsymbol{L}$:

$$\boldsymbol{L} = \begin{bmatrix} L_1 \\ L_2 \\ L_3 \\ L_4 \end{bmatrix} = \begin{bmatrix} (Y_1 - c(dt_r - dt_1^s))^2 - (d_1)^2 \\ (Y_2 - c(dt_r - dt_2^s))^2 - (d_2)^2 \\ (Y_3 - c(dt_r - dt_3^s))^2 - (d_3)^2 \\ (Y_4 - c(dt_r - dt_4^s))^2 - (d_4)^2 \end{bmatrix} \tag{2.123}$$

Utilizing the NRM, the Jacobian matrix of the loss function is required, which is equal to:

$$J(\boldsymbol{L}) = \frac{\delta \boldsymbol{L}}{\delta \boldsymbol{s}} = \begin{bmatrix} \frac{\delta L_1}{\delta x} & \frac{\delta L_1}{\delta y} & \frac{\delta L_1}{\delta z} & \frac{\delta L_1}{\delta cdt_r} \\ \frac{\delta L_2}{\delta x} & \frac{\delta L_2}{\delta y} & \frac{\delta L_2}{\delta z} & \frac{\delta L_2}{\delta cdt_r} \\ \frac{\delta L_3}{\delta x} & \frac{\delta L_3}{\delta y} & \frac{\delta L_3}{\delta z} & \frac{\delta L_3}{\delta cdt_r} \\ \frac{\delta L_4}{\delta x} & \frac{\delta L_4}{\delta y} & \frac{\delta L_4}{\delta z} & \frac{\delta L_4}{\delta cdt_r} \end{bmatrix} = 2 \begin{bmatrix} x_1^s - x & y_1^s - y & z_1^s - z & c(dt_r - dt_1^s) - Y_1 \\ x_2^s - x & y_2^s - y & z_2^s - z & c(dt_r - dt_2^s) - Y_2 \\ x_3^s - x & y_3^s - y & z_3^s - z & c(dt_r - dt_3^s) - Y_3 \\ x_4^s - x & y_4^s - y & z_4^s - z & c(dt_r - dt_4^s) - Y_4 \end{bmatrix} \tag{2.124}$$

after initializing the NRM with $\boldsymbol{s}_0$ which can also be set as a zero vector, the algorithm proceeds to approach the coarse position solution as:

$$\Delta \boldsymbol{s}_j = -J(\boldsymbol{L})_j^{-1} \boldsymbol{L}_j \tag{2.125}$$

where $\boldsymbol{L}_j = \boldsymbol{L}(\boldsymbol{s}_j)$

$$\boldsymbol{s}_{j+1} = \boldsymbol{s}_j + \Delta \boldsymbol{s}_j \tag{2.126}$$

where j refers to the iteration step. The iterations continue until either the termination condition is satisfied or the maximum number of iterations is reached.

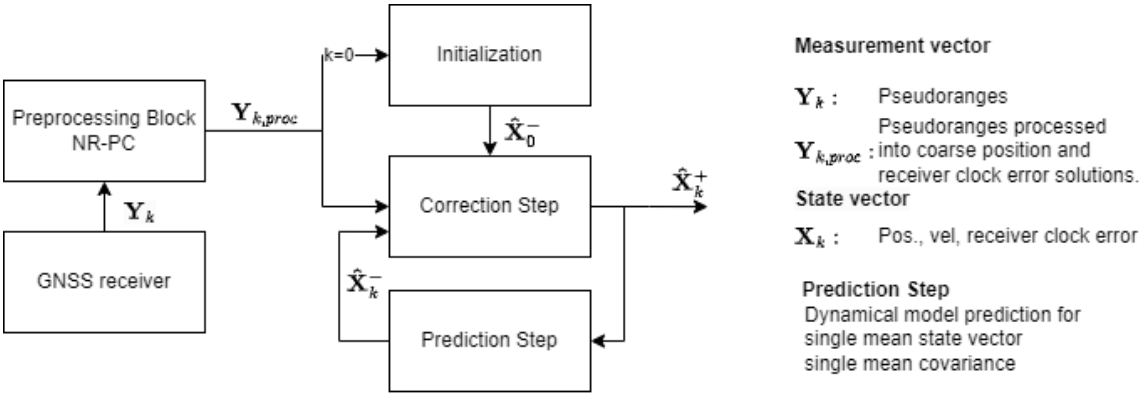

Figure 2.13: General architecture for the improved Preprocessing Extended Kalman Filter with the NRPC.

Once two sets of pseudorange measurements are converted to numerical solutions, the coarse positions $\boldsymbol{r}_c$ are used to compute the coarse velocity via a finite difference method:

$$\dot{\boldsymbol{r}} \approx \frac{\boldsymbol{r}_{c,1} - \boldsymbol{r}_{c,0}}{\Delta t} \tag{2.127}$$

which is used to automatically initialize the EKF portion of the algorithm.

Subsequently, the EKF blocks The state vector in the PEKF, same as for EKF is defined as:

$$\boldsymbol{X} = [\boldsymbol{r}, \dot{\boldsymbol{r}}, cdt_r]^T \tag{2.128}$$

in fact, the only differences between the algorithms are the:

1. observation model h
2. observation vector $\boldsymbol{Y}$
3. the observation Jacobian H
4. initialization procedure

The observation vector at point k is:

$$\boldsymbol{Y}_k = [\boldsymbol{r}_c, cdt_{r,c}]^T \tag{2.129}$$

Thus, the observation model is:

$$h(\boldsymbol{X}) = [\boldsymbol{r}, cdt_r]^T \tag{2.130}$$

which leads to the observation Jacobian:

$$H = \begin{bmatrix} \boldsymbol{I}_{3\times3} & \boldsymbol{0}_{3\times4} \\ \boldsymbol{0}_{1\times6} & 1 \end{bmatrix} \tag{2.131}$$

Instead of the initial filter state being specified, in the PEKF it is auto-assigned. Once two coarse solution are found, the initial velocity $\dot{r}_0$ is calculated according to Equation 2.127. The coarse positions and receiver clock errors fill up the remaining initial EKF state.

2.6.7. Newton-Raphson PC Preprocessing EKF

In this subsection, a modification to the original PEKF is proposed. A change is made in the Preprocessing block. In order to improve its computational load, a new numerical root-solver is used, called Newton-Raphson Predictor-Correction (NRPC). NRPC was originally applied to N-dimensional cases in [67]. While the original NRM has a convergence rate of 2, whereas NRPC method shows a rate of $\approx$2.4. The formulation presented below follows [67].

While the NRM performs a corrective step at every iteration, the NRPC methods performs two separate steps. Firstly, a prediction step is made using knowledge from the previous iteration, following a correction step in the current iteration. The $J(\boldsymbol{L_j})^{-1}$ values are reused, so even though 2 calculations are made per iteration, only a single Jacobian inversion is required.

The sought numerical solution s and the loss function $\boldsymbol{L}$ remain unchanged from Equation 2.122 and Equation 2.123, respectively. Furthermore, the first iteration remains identical to the NRM:

For j = 0:

$$\hat{\boldsymbol{s}}_j = \boldsymbol{s}_j \tag{2.132}$$

$$\Delta \boldsymbol{s}_j = J(\boldsymbol{L}(\boldsymbol{s}_j))^{-1} \boldsymbol{L}(\boldsymbol{s}_j) \tag{2.133}$$

where $\Delta \boldsymbol{s}_j$ is the *predicted* correction and $\hat{s}_j$ is the *predicted* solution. As mentioned, they are initialized to be identical to the initial NRM correction and solution. They then lead to the next *corrected* solution:

$$\boldsymbol{s}_{j+1} = \boldsymbol{s}_j + \Delta \boldsymbol{s}_j \tag{2.134}$$

for j > 0:

$$\Delta \hat{\boldsymbol{s}}_j = J(\boldsymbol{L}\left(\frac{1}{2}\left[\boldsymbol{s}_{j-1} + \hat{\boldsymbol{s}}_{j-1}\right]\right))^{-1} \boldsymbol{L}(\boldsymbol{s}_j) \tag{2.135}$$

which is used for the *predicted* solution at the next step:

$$\hat{\boldsymbol{s}}_{j+1} = \boldsymbol{s}_j + \Delta \hat{\boldsymbol{s}}_j \tag{2.136}$$

the correction at the current step is then computed using the mean between the *predicted* and *corrected* solutions:

$$\Delta \boldsymbol{s}_j = J(\boldsymbol{L}\left(\frac{1}{2}\left[\boldsymbol{s}_j + \hat{\boldsymbol{s}}_j\right]\right))^{-1} \boldsymbol{L}(\boldsymbol{s}_j) \tag{2.137}$$

which leads to the *corrected* solution at the next step:

$$\boldsymbol{s}_{j+1} = \boldsymbol{s}_j + \Delta \boldsymbol{s}_j \tag{2.138}$$

and as mentioned before, to compute the next *predicted* correction, $J(\boldsymbol{L}\left(\frac{1}{2}\left[\boldsymbol{s}_j + \hat{\boldsymbol{s}}_j\right]\right))^{-1}$ is reused as $J(\boldsymbol{L}\left(\frac{1}{2}\left[\boldsymbol{s}_{j-1} + \hat{\boldsymbol{s}}_{j-1}\right]\right))^{-1}$.

The same convergence condition is applied as for the original NRM. The interface between the Preprocessing block and the EKF blocks remains the same as in the original NRM-PEKF.

3

LISL Variable Evaluation

Having gone through the relevant theory, the focus is now shifted to geometry and dynamics occurring in LISL. This is relevant as an orbit position error's impact on the subsequent pointing error depends on multiple factors, such as the link distance, relative velocities, and the direction of the position error, relative to the LOS vector. Additionally, the available communication window length dictates the maximum required orbit prediction window and is thus relevant to quantify. Furthermore, as the laser terminals have different capabilities in terms of FOV and supported link distances, the differences in their potential performances can be highlighted. Lastly, increasingly challenging link cases can be selected to later benchmark the integrated OD-OP methods in 5.

First, the method used to evaluate the LISL is described in section 3.1. In section 3.2, the links available to a LEO Polar host satellite are analyzed. The links are processed into link histograms and communication windows while imposing LCT limitations. Time series of the occurring pointing angles and distances are also shown, where only Earth occultation is considered. Subsequently, the same is repeated for a LEO Inclined and MEO Host satellite in section 3.3 and section 3.4. Afterwards, the available communication windows are presented for both terminals in section 3.5, where the critical prediction windows are established. The link cases selected to benchmark the OD-OP algorithm performance are described in section 3.6. An overview of the results and conclusions of RQ1 are shown in section 3.7.

3.1. Method Description

3.1.1. Link Geometry Calculation Architecture

The architecture used to calculate and process the LISL variables is presented in Figure 3.1. First, the host-target positions are subtracted to calculate cartesian LOS vectors in ECI. These are then rotated to the host's RSW frame, which can then further be translated and rotated to the Terminal frames. At this point, the cartesian LOS can be converted to Azimuth/Elevation angles and link distances. At this point, limitations can be imposed to detect when link opportunities start/end.

The viewing angles and imposed limitations are visualized in Figure 3.2 for a 60 minute simulation between two satellites with LCT1 angle/range limitations. It can be seen that at around minute 8, the azimuth angles are out of the viewing limits and from 29 to 47 minutes, the link distance is too large. Thus, the link is unavailable at those periods and this would effectively results in 3 detected links: 1) 7 minutes at 0-7 minute period, 2) 21 minutes from 8 to 29 minutes and 13 minutes from 47 to 60. Implementing this and running it through for each target satellite, the link windows for the entire constellation can be quantified.

Further processing of link variables is possible using numerical differentiation. This way, the angular and slant rates are calculated. The pointing angles and their rates can be used to categorize links into link cases. These link cases will later be used to quantify the OD-OP algorithm performance in chapter 5.

Applying this data processing architecture to each host and target satellite combination and with the help of simplifying assumptions, idealistic LISL variables can be determined. The link windows and the link distributions represent the absolute maximums, while in reality only a fraction of the windows or links

will actually be attainable. The assumptions to be considered are that the host/target satellites' attitude is assumed to be perfectly aligned with the RSW reference frame. This would not be the case during attitude manoeuvres, such as sun-pointing mode. Furthermore, the LISL variables are only considered precise to the degree-level. Disturbances due to perturbations, micro-vibrations, any misalignment due launch loads or other sources are neglected. Avoidance of sun-pointing was also not considered.

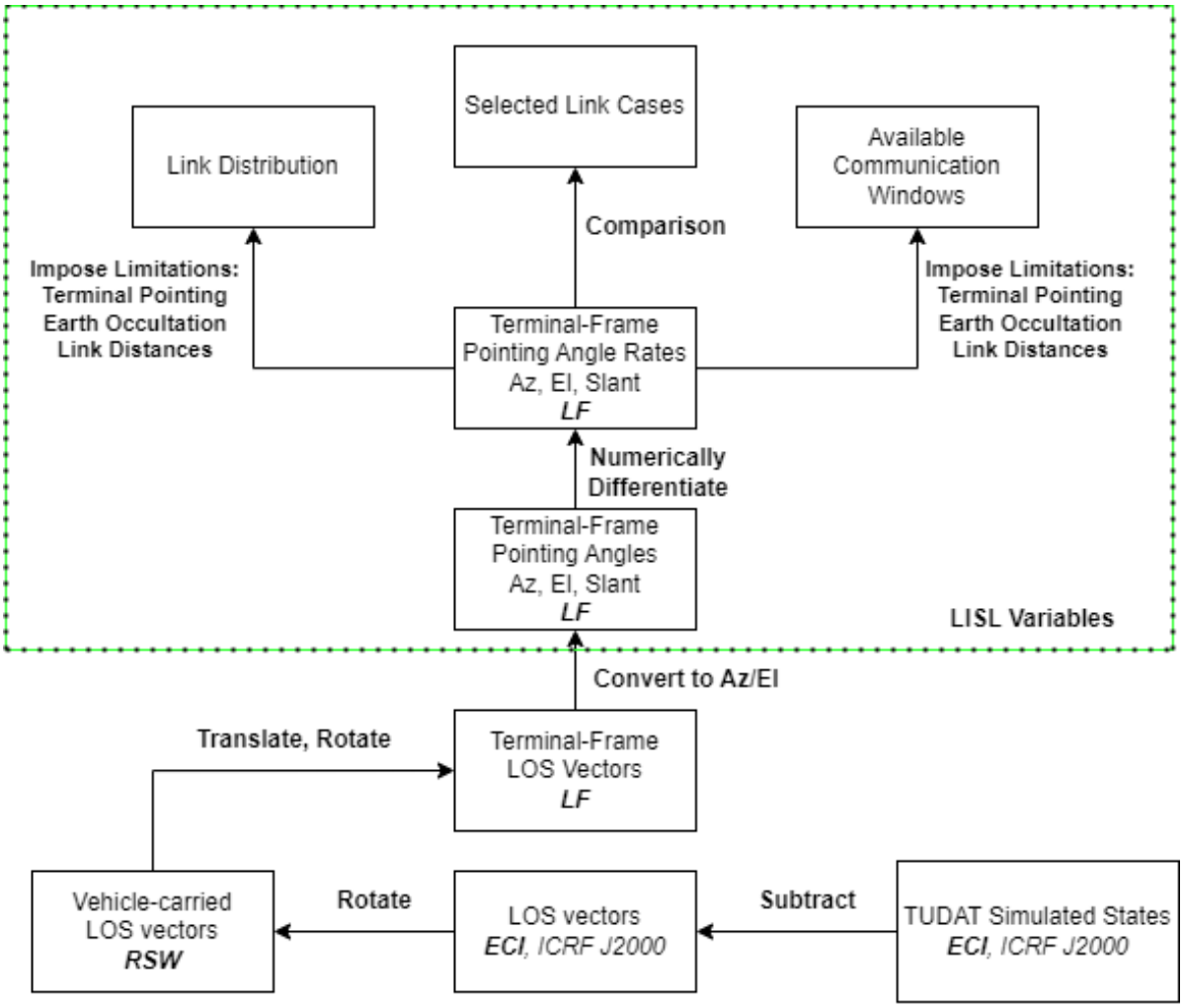

Figure 3.1: Architecture for processing simulated orbits to pointing angles and link parameters, indicating the reference frame of the parameters at each stage.

3.1.2. Considered Terminal Limitations

Two LCT's with different pointing angle and range limitations were considered. Their specifications for supported link geometry are shown in Table 3.1. LCT1 only has a basic 10 degree gap in supported azimuth angles and a total 30 degree elevation range. Although due to the link distance, it also unable to support links involving MEO satellites, only the angular limitation will be considered there. This way, although unrealistic, LCT1 links to MEO can be used to evaluate the benefits of the additional elevation coverage of LCT2. LCT2 supports an elevation range above 90 degrees and does not impose link distance limitations.

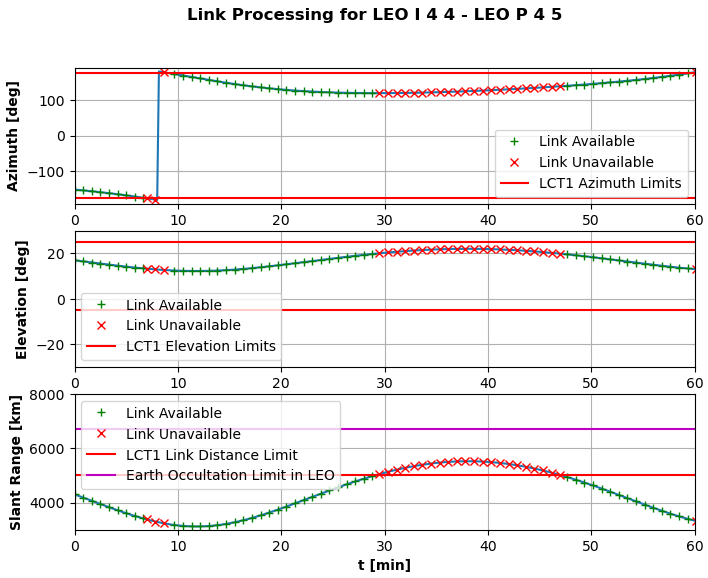

Figure 3.2: Example of link angle and distance processing into available link windows with imposed LCT1 Limitations.

Table 3.1: Link geometry limitations of both considered terminals, with LCT1 modelled according to Mynaric's CONDOR Mk2 and LCT2 according to CONDOR Mk3 publicly available specifications [24], [25].

Parameter/Terminal	LCT1	LCT2
Azimuth Range [deg]	[-175:175]	[-175:175]
Elevation Range [deg]	[-5:25]	[-60:90]
Supported Maximum Link Distance [km]	5000	25000

3.2. LEO Polar host links

The selected LEO Polar Host is visualized in Figure 3.3. The Polar satellite 4 of plane 4 was selected and consistently maintained throughout this chapter as the polar host. The opposite polar-shell planes are shown in orange color and adjacent planes in purple. The plane of the host was highlighted and scatters of the polar satellites visible at that time were also indicated.

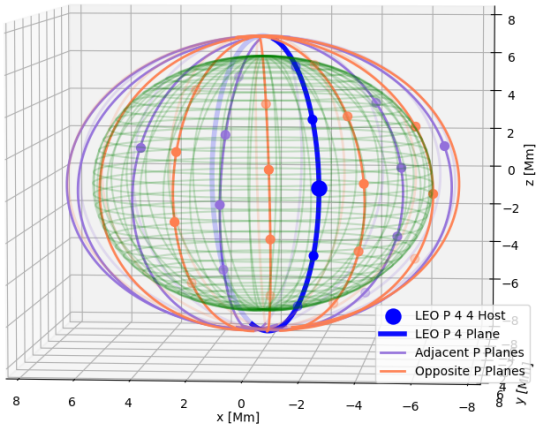

Figure 3.3: LEO Polar Host P 4 4 satellite, with adjacent planes in purple and opposite planes in orange.

3.2.1. Communication Window Distribution

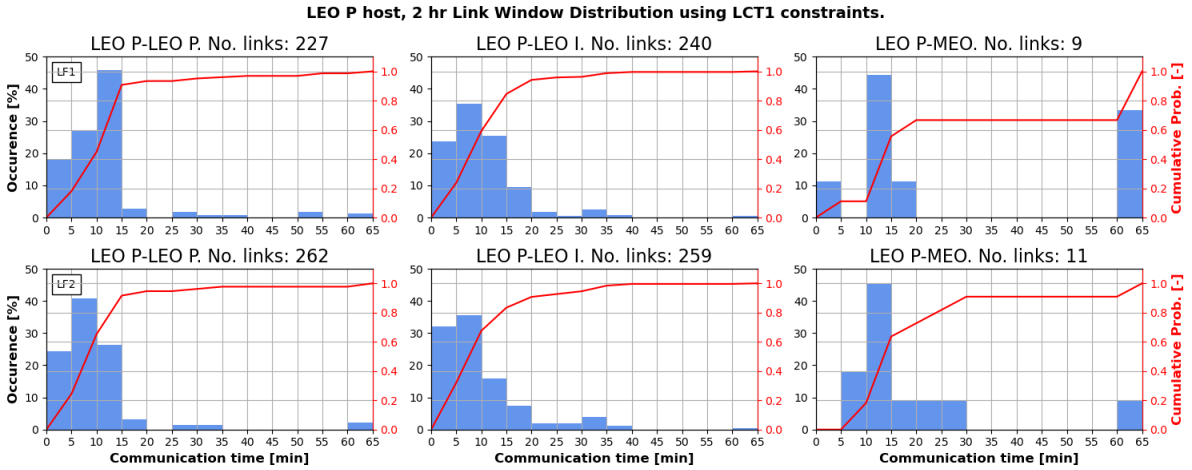

Figure 3.4: Communication window distribution for LCT1 in 2 terminal placements on the LEO Polar Satellite.

The link window distribution for the LEO Polar host using LCT1 can be seen in Figure 3.4. The majority of intra-shell links are 15 minutes or less, regardless of the LF1 or LF2 placement. Several links also occur in the 15-60 minute regions and very few in the 60+ minute region. Due to LCT1's azimuth limitations, LF2 orientation offers more 60+ minute links, as it can support both leader and follower intra-orbit LISL, whereas LF1 only supports the trailing satellite.

The LCT1 inter-shell LEO links are similar as over 80% of links are also below 15 minutes. Several links up to 40 minutes occur, which are possible for satellites in orbital planes close to the host's. A couple of 60+ minute links also occur, to targets with a nearby ascending node.

For LEO P-MEO cases, most links occur in 10-15 minute windows. Most links are also in the 0-15 minute range, but some are possible for 60+ minutes. Unlike LEO-LEO links, LEO-MEO links are not permanently available, as Earth occultation occurs each LEO orbit.

Considering the LEO Polar host link distribution using LCT2 in Figure 3.5 a general improvement in link availability can be seen. This is visible both in terms of number of links available (low-mid 200s for LCT1 improved to high 200s-mid 300s for LCT2 in LEO) and having longer links. Although most links are also 15- minutes, a significant portion fits in the 15-20 minute bin. Furthermore, more links occur in the 20-60 minute region, as well as the 60+ cut-off. This is true for both intra and inter-shell LEO links. In MEO links the situation improves too, as the majority of links are now 40+ minutes long, compared to the 10-15 minutes as seen for LCT1.

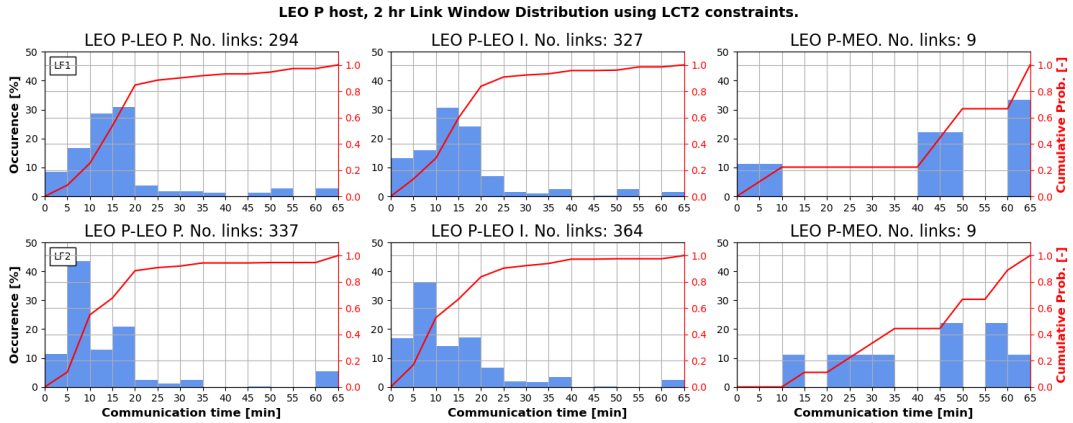

Figure 3.5: Communication window distribution for LCT2 in 2 terminal placements on the LEO Polar Satellite.

3.2.2. Available Link Distribution

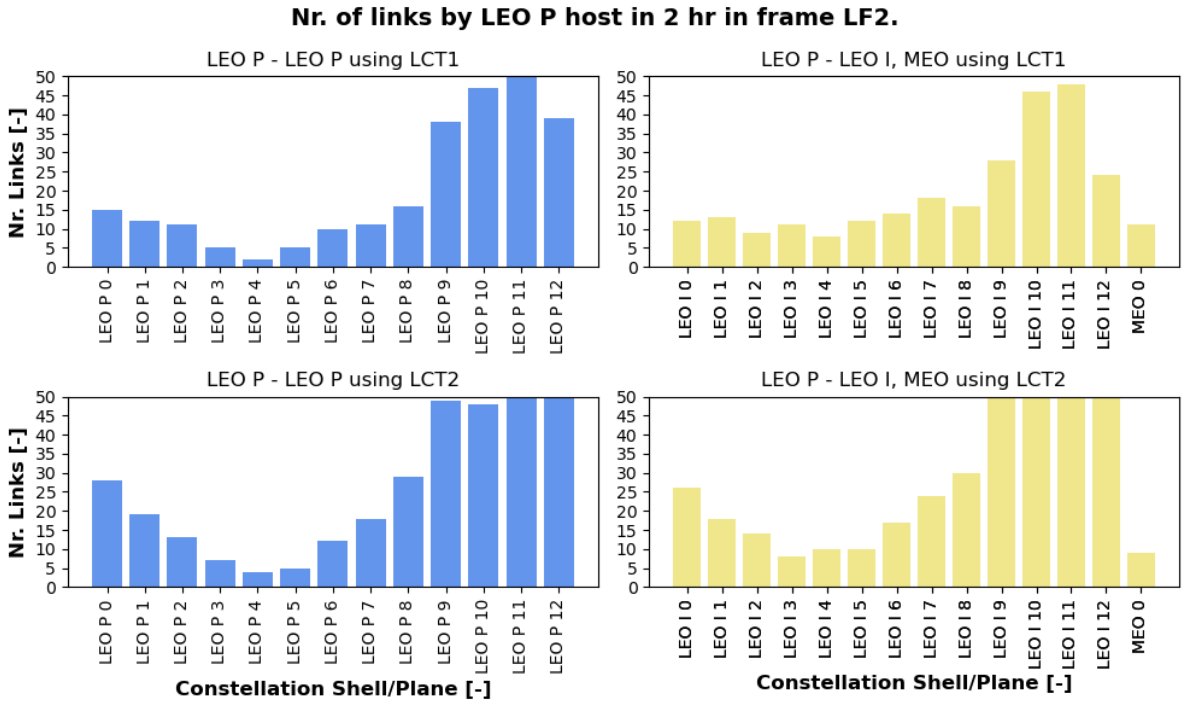

Figure 3.6: Available links per orbital plane for LCT1 and LCT2 placed at LF2 on the LEO Polar Satellite.

The established link distribution per orbital shell/plane for a LEO Polar host, using LCT1 and LCT2 is shown in Figure 3.6. In each terminal/shell case, it can be seen that the highest number of linked satellites are in planes 10 and 11, which are directly opposite to the host's. The links occurring in these planes are also the majority of the short (15- minute) links seen previously in the communication window distribution, since target satellites in these planes fly in nearly opposite direction as the host, meaning that links occur for a short time, twice per orbit with each target. When looking at planes with the ascending node at the same location as the host's is where the fewest links occur, but these links are available continuously and therefore are only counted once. With the plane's ascending node getting more and more distant, more shorter links become available, until the peaks at the opposite planes.

Comparing the LCT1 link number distribution to LCT2's, it can be noted that LCT2 generally provides more possibilities for links with almost every plane. This is especially visible in the planes near the opposite plane nr. 11, which is where LCT2's support of longer slant-ranges leads to links with more targets. That is also seen with the co-planar links, where twice as many satellites are continuously available as in LCT1's case.

The links with MEO satellites are few compared to LEO for both terminals, but this is due to the far sparser MEO orbital plane and due to the lower relative velocities leading to longer links. The main limitations are Earth occultation and out of range AE angles. The effect of AE angle limits is visible when comparing the LEO P - MEO links with LCT1 and LCT2, where it can be seen that LCT1 leads to more links. This is because LCT1 has a far lower AE range, leading to more links being cut and re-established, while LCT2's links remain available for longer.

3.2.3. LISL Coarse Pointing Variables

LEO Polar - LEO Polar

Co-planar links The co-planar links for the LEO Polar host satellite are shown in Figure 3.7. 4 links are in sight at all times, 2 ahead - with azimuth at 90 deg and 2 behind the host satellite, with azimuth -90 deg. It can be seen that azimuth, elevation and slant-range are pretty much constant and only orbit perturbations lead to small variations (<mdeg for AE rates and <50m/s for Slant rates). Of all link

types, the co-planar link appears to be the least challenging in maintaining a connection due to the near-constant pointing angles.

Comparing the limitations of each terminal, it becomes clear that LCT2 can support more co-planar links than LCT1. The 2nd satellite ahead/behind the leader/follower has a slant range above 6000 km and elevation over 25 deg, which are outside of LCT1's capabilities. That is why twice as many links for LCT2 were registered than for LCT1 in LEO P plane 4, as was shown in Figure 3.6.

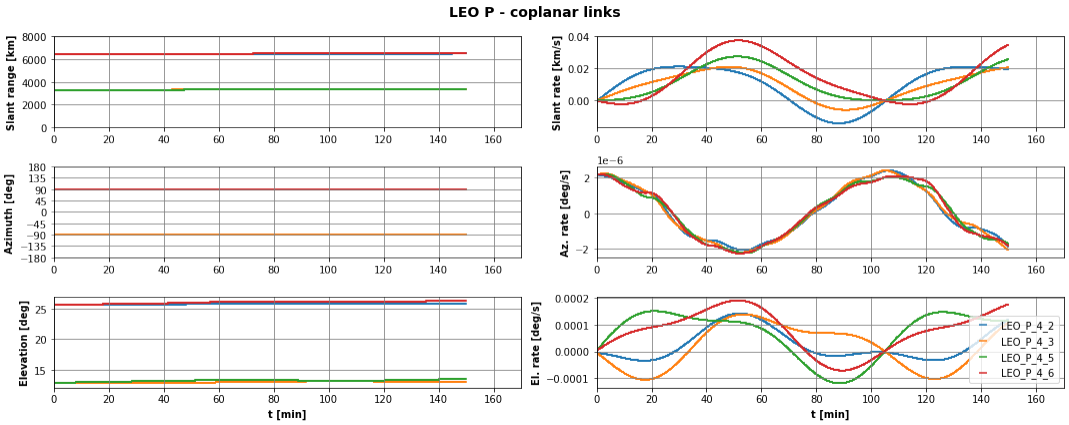

Figure 3.7: AER (left) and rates (right), using LF2 placement for LEO P intra-orbit links.

Cross-plane links The link dynamics with the plane having its ascending node opposite to the host's are shown in Figure 3.8. Due to the proximity of the orbital planes and opposite flight directions, links occur frequently and with fast dynamics: every link exhibits slant rates of over +/- 10 km/s and azimuth rates above +/- 0.3 deg/s. Observing the slant range for each target, it can be seen that within a 15-20 minute window, the target satellite comes into view (slant range approx. 7000 km), continues to get near the host, flies past and increases in link distance until it is out of view.

The most challenging links to establish appear to be the 2nd-4th satellites, due to the proximity at which the fly-by occurs. This can be seen in far lower minimum slant-range values (<500 km compared to approx. 1500km) and azimuth rates (+/- 2 deg/s compared to approx. 0.5 deg/s). Which satellites will have the lowest slant-ranges and faster azimuth rates depends on the relative phasing, but it can be concluded that the most challenging intra-polar shell links occur between satellites flying in opposite directions and with the closest fly-by distances.

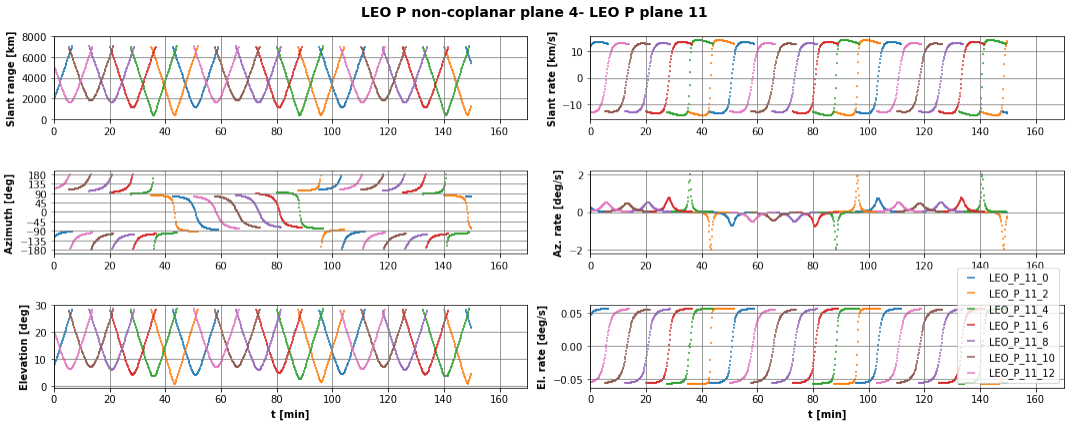

Figure 3.8: AER (left) and rates (right), using LF2 placement for LEO P furthest cross-plane links.

Comparing the terminal's capabilities, it becomes clear why LCT2 had many more links in the 15-20 minute region, compared to LCT1's peak occurrences at 10-15 minutes, as was shown in the LEO P-LEO P links in Figure 3.5 and Figure 3.4, respectively. LCT1 can support these links for a significantly

shorter period due to the slant range limitations. Effectively, when a target comes into view, it takes longer for it to get close enough to establish a link and after the fly-by, it takes less time for the link distance to become too large before the target is out of view.

LEO Polar - LEO Inclined

The inter-shell LEO links with the closest plane 4 are shown in Figure 3.9. Although at first sight it appears that the link with LEO I 4 4 proves to be the most challenging with azimuth rates over 5 deg/s, it must be pointed out that this is an unrealistic link case. Inspecting the slant-range, it is seen that it varies from slightly over 4000 km to 0 km, which indicates an unrealistically close fly-by. That is indeed the case, as no relative phasing between the two LEO shells was added in the simulation, which was an oversight. However, in reality inter-shell relative phasing would be included to reduce collision risks and therefore this extremely fast link is not considered for further analysis.

The remaining links with this plane are few and varied in available time windows dynamical complexity. Two are seen with slant ranges between 6000-4000km, which would lead to more 20-30 minute long links with LCT1 and 60+ minute links for LCT2. The two 6000+ km distance links would only lead to link possibilities for the LCT2 and fill some of the 30-40 minute long bins. Thus, an improvement of link availability can again be seen for LCT2 and these link types are sparse and in the mid-complexity in terms of dynamics and communication windows.

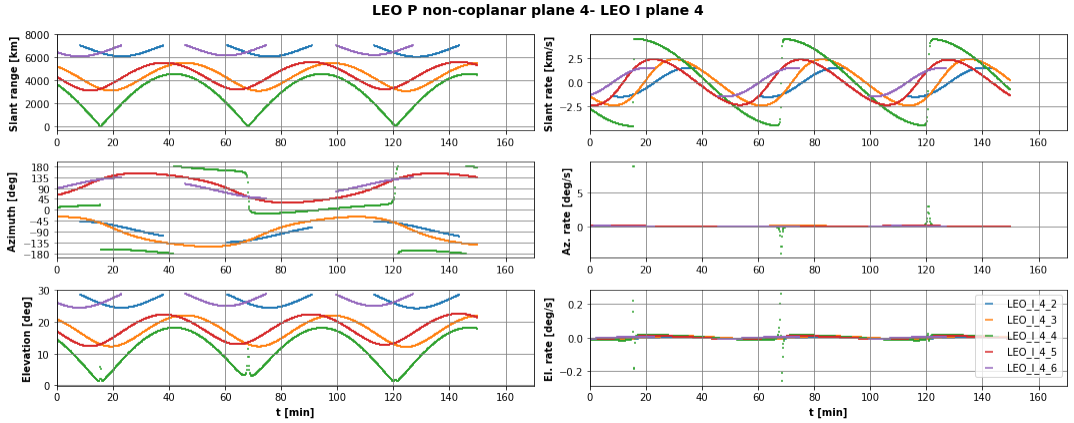

Figure 3.9: AER (left) and rates (right), using LF2 placement for LEO P-LEO I inter-shell near plane links with LEO I 4.

The inter-shell LEO links with the opposite plane 11 are shown in Figure 3.10. A similar unrealistic case can be seen here, as was in plane 4. Here, target satellite 10 also has an unreasonably close fly-by, with much higher azimuth rates and therefore is not analyzed further.

The remaining links have slant ranges which lead to the different communication window lengths and numbers of available links for the LCT1 and LCT2. Several links can be seen where the minimum slant range is barely below 5000 km, which explains why the largest proportion of LEO P -LEO I links were in the 0-5 minute region, while LCT2 was shown to have most links in the 5-10 minute region. Furthermore, as the orbital plane angles become larger, fewer links would appear to have slant ranges below 5000 km, which is why LCT2 registered 100 more links between a LEO P host and the LEO I shell.

Another set of inter-shell links to the 8th plane is shown in Figure 3.11. Observing these link variables, the general trend of how a bigger difference in the host and target orbit nodes affect the link variables. Fewer links become visible, slant ranges increase, as do the minimum slant ranges. The azimuth rates are up to +/- 0.4 deg/s, elevation rates up to +/- 0.05 deg/s. Overall, these links would also be in the middle in terms of communication window lengths and link dynamics.

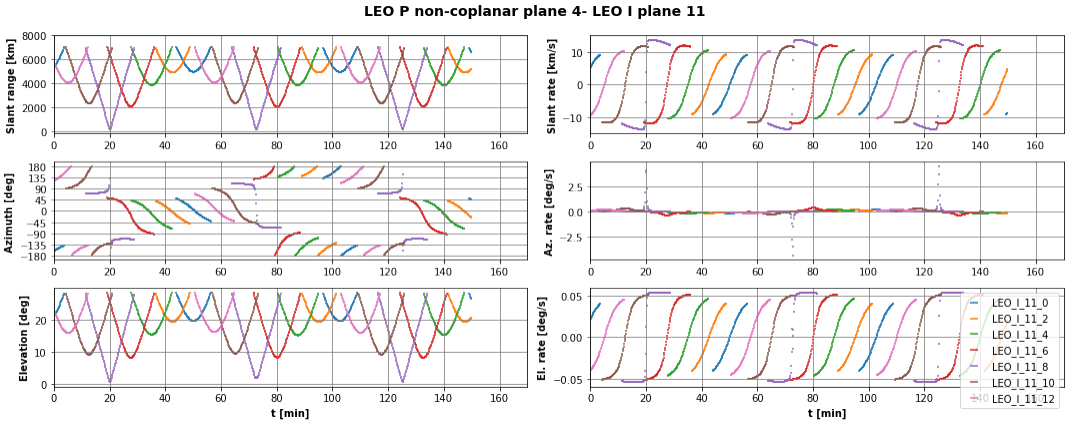

Figure 3.10: AER (left) and rates (right), using LF2 placement for LEO P-LEO I inter-shell opposite plane links with LEO I 11.

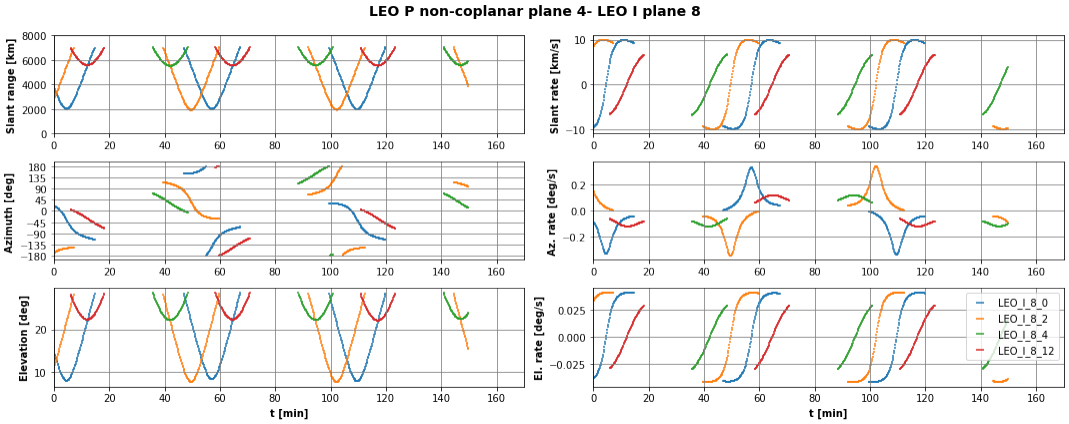

Figure 3.11: AER (left) and rates (right), using LF2 placement for LEO P-LEO I inter-shell links with LEO I 8.

LEO Polar - MEO

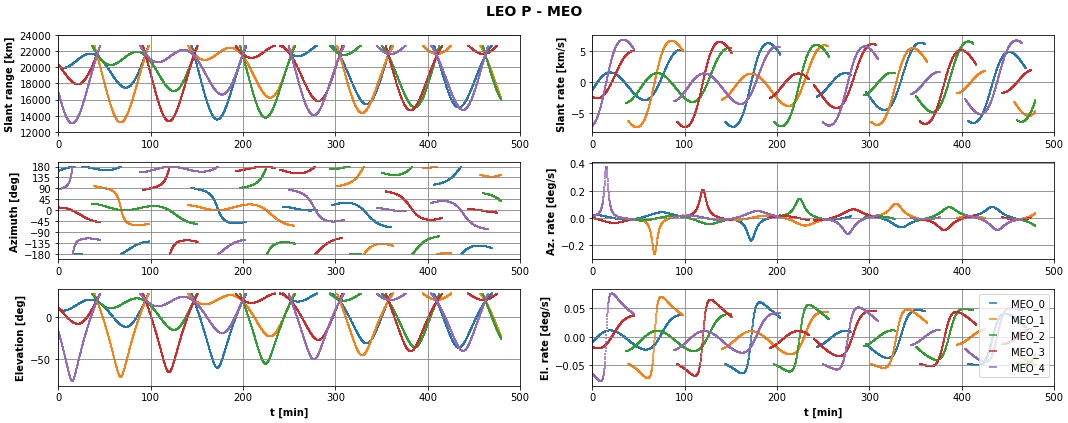

Figure 3.12: AER (left) and rates (right), using LF2 placement for LEO P-MEO links.

The links between the LEO Polar host and the equatorial MEO satellites are shown in Figure 3.12. The link dynamics are different from LEO links in several aspects: the links are generally much longer (20 or 50+ minutes), slant ranges are all above 13000 km, elevation angles range over about 90 degrees and the azimuth ranges are about 90 degrees per link. In terms the AER rates, they do not exceed the more challenging intra-shell LEO cases, as the relative motion slower, with slant rates about half of the

fastest LEO link cases.

In terms of terminal performance, the link variables would definitely prove challenging for the LCT1. Without considering the slant-range, the elevation ranges are too wide. As the LCT1 only supports elevations within a 30 degrees interval, about 2/3 of possible links could not be established. The azimuth angles can also be an issue, as in many cases they are above +/- 175 degrees. This was indeed the case seen on the right side in Figure 3.4 and Figure 3.5, as LCT2 could both support many more links in the 60+ minute bin. Therefore, although the link dynamics aren't as fast, LEO-P to MEO links still prove challenging due to the large ranges of expected azimuth and elevation angles.

3.3. LEO Inclined host links

The selected LEO Inclined Host is visualized in Figure 3.13. The Inclined satellite 4 of plane 4 was selected and consistently maintained throughout this chapter as the inclined plane host. In the plot, one can see the opposite inclined shell planes in orange color and adjacent planes in purple. The plane of the host was highlighted and scatters of the polar satellites visible at that time were also indicated.

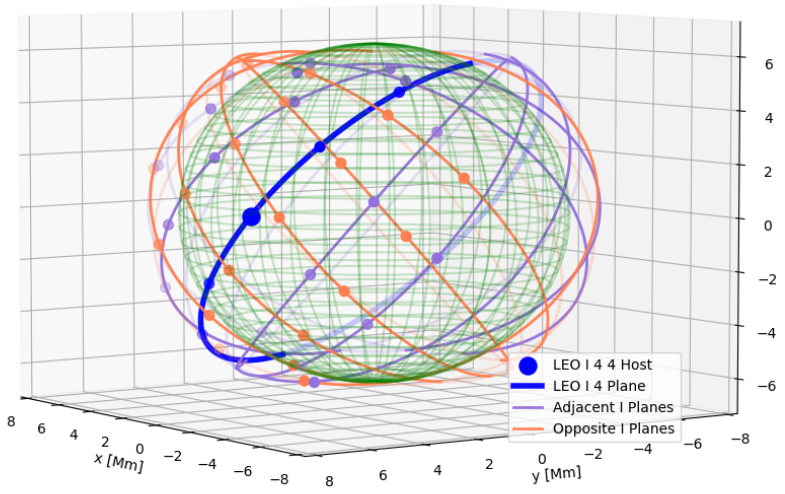

Figure 3.13: 3D visualization of the LEO Inclined Host I 4 4 satellite, with adjacent planes 1-3; 5-7 in purple and opposite planes 0; 8-12 in orange.

3.3.1. Communication Window Distribution

The link window distribution for the LEO Inclined orbit host using the LCT1 is shown in Figure 3.14 and using the LCT2 in Figure 3.15. A clear distinction compared to the LEO P host can be pointed out. Far fewer intra-shell links are available: LEO I- LEO I leads to 150 and 218 links using LCT1 and LCT2, while LEO P- LEO P had 262 and 337, respectively. Furthermore, the MEO link window distribution using LCT1 is only up to 30 minutes long, while LEO-P had 60+ minute LCT1 links available with both terminal placements. The reasons for these differences will become clear in the upcoming links/plane distributions in subsection 3.3.2 and link variable plots in subsection 3.3.3.

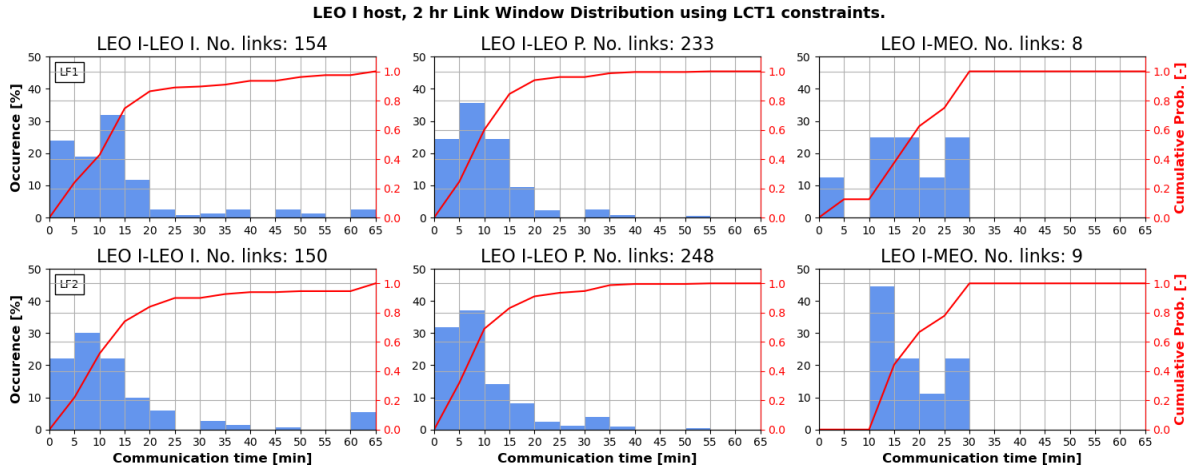

Figure 3.14: Communication window distribution for LCT1 in 2 terminal placements on the LEO Inclined Satellite.

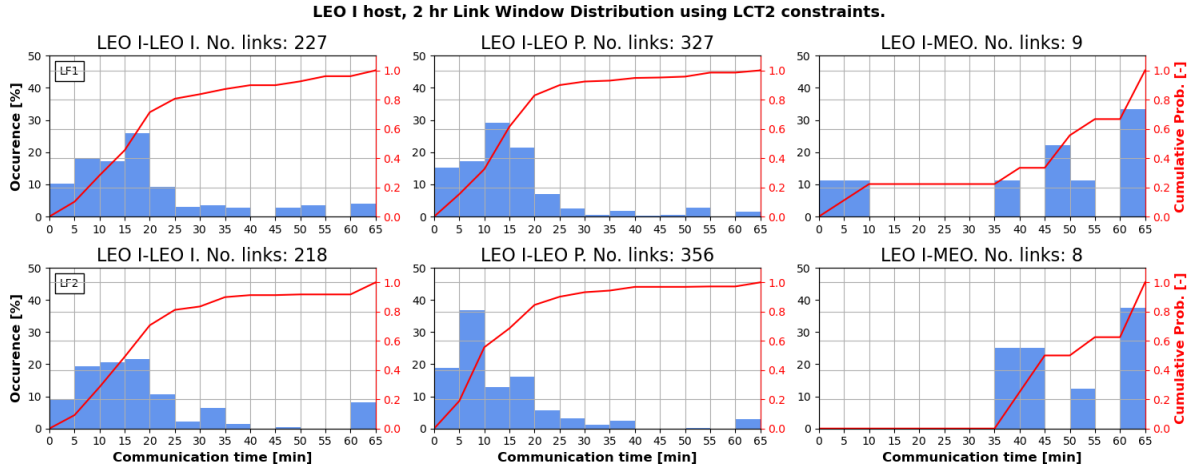

Figure 3.15: Communication window distribution for LCT2 in 2 terminal placements on the LEO Inclined Satellite.

Analyzing the link window distributions, several conclusions can be made regarding the required orbit prediction time. Considering the Terminal positions LF1 and LF2 for both LCT1 and LCT2, it is clear that the window distribution does not change significantly. Small differences can be spotted, such as more 60+ minute LEO I- LEO I for LF2 compared to LF1 or LF1 having to a higher fraction of 10-15 minute links than LF2 in the LEO I- LEO P case using LCT1. When looking at the overall distribution of communication windows for both terminals, it can be noted that much like the LEO P host case, most communications are 20 minutes or less. For LCT1, a large fraction of links are 15 minutes or less, while for LCT2 a significant portion also in the 15-20 minute bin. For LCT1, about 20% of links also occur in the 20-60 and 60+ minute regions for intra-shell links, while the LEO inter-shell links generally only span until 35 minutes, with very few in the 35-40 and 50-55 minute bins and none longer. For the LEO I- MEO links with LCT1, none of them exceed 30 minutes and they are similarly likely to occur in each of the 10-30 minute windows. Looking at LCT2, again, more and longer communication windows are available. The 15-20 minute bin is a very frequent intra-shell link duration and not uncommon for the inter-shell links. Additionally, many more short and long links are available in the LEO inter-shell case, with 60+ minute links becoming possible. Finally, in the LEO I-MEO case, links above 35 minutes are a lot more frequent, with the majority being 60+ minutes long.

3.3.2. Available Link Distribution

The number of links with each orbital shell/plane is shown in Figure 3.16. Analyzing the intra-shell planes on the left, it becomes clear why there are fewer LEO I-LEO I links in comparison to LEO

P-LEO P. A clear difference is the LEO I links with the opposite and near-opposite planes (8-12th), as 50 % fewer links occur than in the analogous LEO P- LEO P case. This is due to the non-polar inclination of inclined shell. Effectively, the link distances between opposite inclined orbital planes are only sufficiently close near the ascending and descending nodes. Further North/South along the orbit, the inclination leads to much larger relative distances than in the polar-polar case. In the case of LEO inter-shell links, many more links can be seen looking at the 45+ links with the LEO P planes 10 and 11. This is the result of the smaller angular difference between the opposite orbital planes, leading to link possibilities throughout the entire orbit, rather than only at the nodes.

Comparing the linking capabilities of LCT1 and LCT2, a significant difference can be seen within nearly every orbital plane. In the intra-shell links, an increase of 5-10 links can be seen with every plane. Similar results are seen in the inter-shell LEO links, most significantly with the near-opposite LEO I planes 9 and 12, where LCT2 leads to 15+ additional links. Linking with MEO does not lead to more links, but they were significantly longer. This shows how the larger link distance support can lead to significantly improved LISL communication capabilities, both in terms of number and length of links.

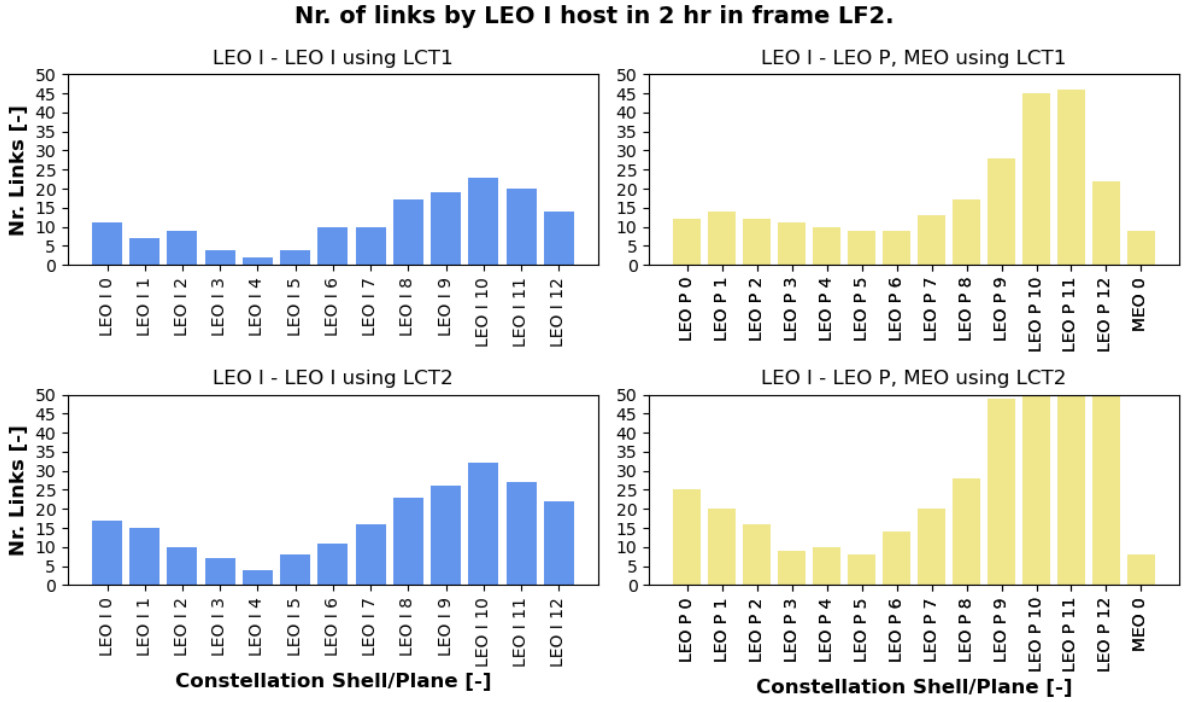

Figure 3.16: Available links per orbital plane for LCT1 and LCT2 placed at LF2 on the LEO Inclined Satellite.

3.3.3. LISL Coarse Pointing Variables

LEO Inclined - LEO Inclined

Co-planar links The co-planar links for the LEO Inclined host satellite are shown in Figure 3.17. 4 links are in sight at all times, 2 ahead - with azimuth at 90 deg and 2 behind the host satellite, with azimuth -90 deg. It can be seen that azimuth, elevation and slant-range are pretty much constant and only orbit perturbations lead to small variations (<mdeg for AE rates and 20m/s for Slant rates). This is consistent with the LEO P co-planar links, where near-constant pointing angles were observed.

Cross-plane links The link dynamics with the plane having its ascending node opposite to the host's are shown in Figure 3.18. Due to the large angular separation of orbital planes links are not frequent (maximum of 2 per orbit), while the opposite flight directions lead to fast dynamics: most link show slant rates of over +/- 10 km/s and azimuth rates up to +/- 0.5 deg/s. Observing the slant range for each target, it can be seen that within a 20-30 minute window, the target satellite comes into view (slant range approx. 7000 km), continues to get near the host, flies past and increases in link distance until it is out of view. Due to the inclination, it can be seen that some targets barely get into the visible distances (targets 5 and 11 having minimum slant ranges over 6000km) and others (0-4 and 13) are

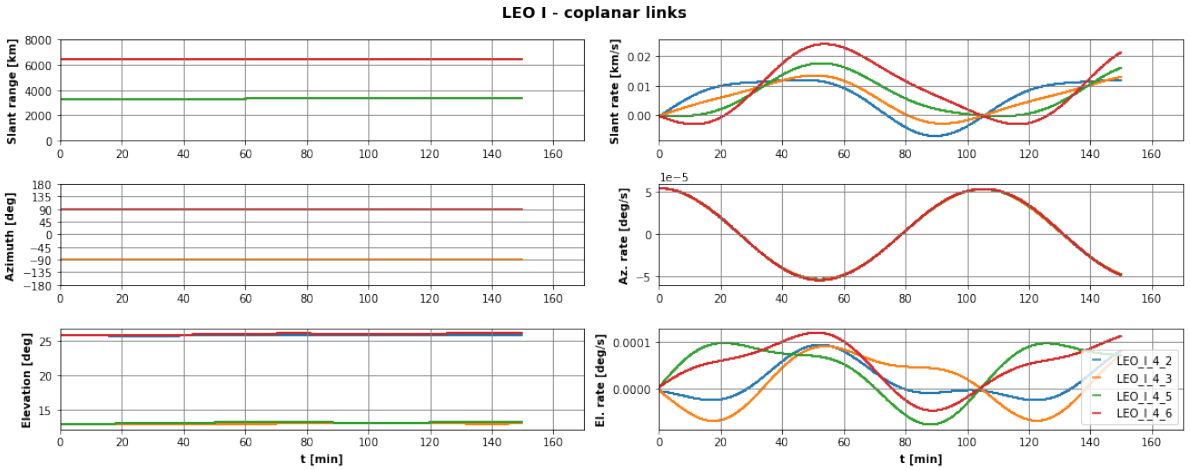

Figure 3.17: AER (left) and rates (right), using LF2 placement for LEO I intra-orbit links.

never in view. Thus it can be concluded that the mid-inclination is the reason for fewer intra-shell LEO I crosslinks being available.

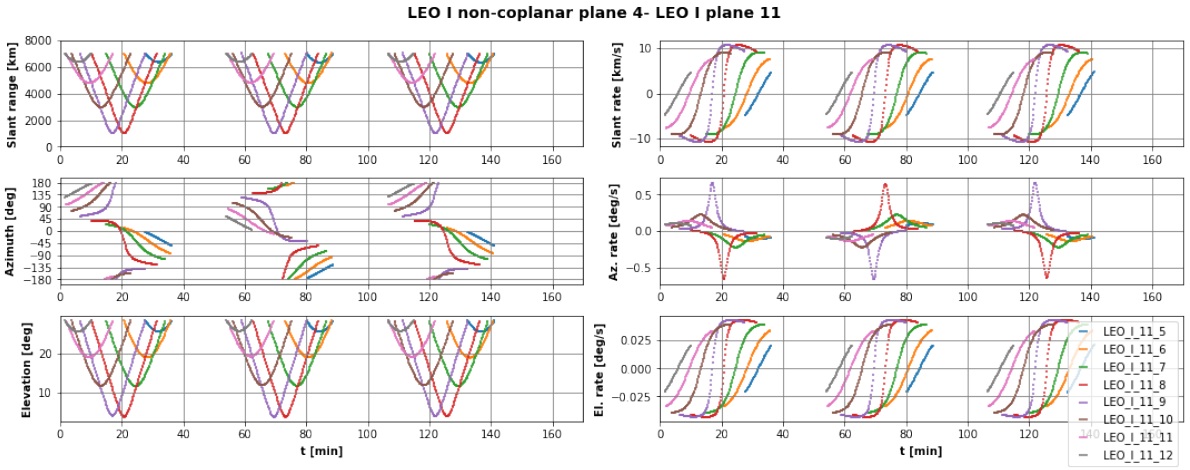

Figure 3.18: AER (left) and rates (right), using LF2 placement for LEO I furthest cross-plane links.

The link dynamics with the near opposite plane is shown in Figure 3.19. Similarly as with LEO I plane 11, links with each target become possible twice per orbit and show fast dynamics. The link with Target satellite 0 appears to be specifically challenging, as azimuth rates of +/- 2 deg/s occur. Again it becomes evident that this is due to opposite flight direction and the close proximity of the fly-by, which appears to be the common condition for the most challenging LEO-LEO links.

The cross-plane links to the nearest orbit are shown in Figure 3.20. Within this plane, relatively few targets are available with mostly long and dynamically slower links. This is a common feature for the near-plane cross links, as a similar flight direction leads to smaller relative velocities (slant ranges up to +/- 2 km/s) and in turns relatively low azimuth rates (mostly below +/- 0.1 deg/s), The most challenging target satellite showing an azimuth rate of around +/- 0.4 deg/s. Again, this occurs due to proximity of the fly-by. Overall, these near cross-plane links can be considered a nominal-challenging category of link cases.

LEO Inclined - LEO Polar

The inter-shell LEO links with the opposite plane 11 are shown in Figure 3.21. The same unrealistic case can be seen here, as was seen from the LEO Polar host in Figure 3.21. Here, target satellite 8 has an unreasonably close fly-by, with much higher azimuth rates and therefore is not analyzed further.

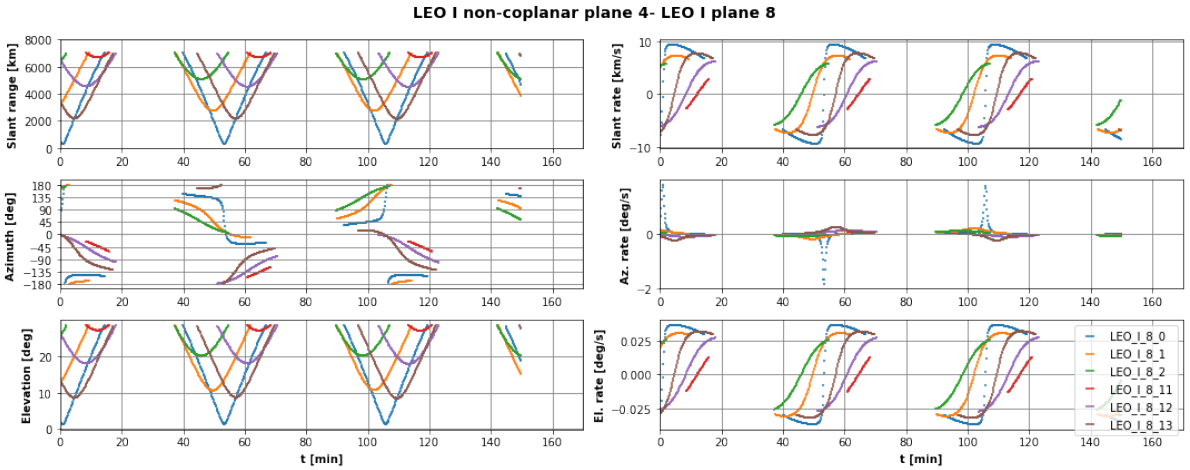

Figure 3.19: AER (left) and rates (right), using LF2 placement for LEO I near opposite links.

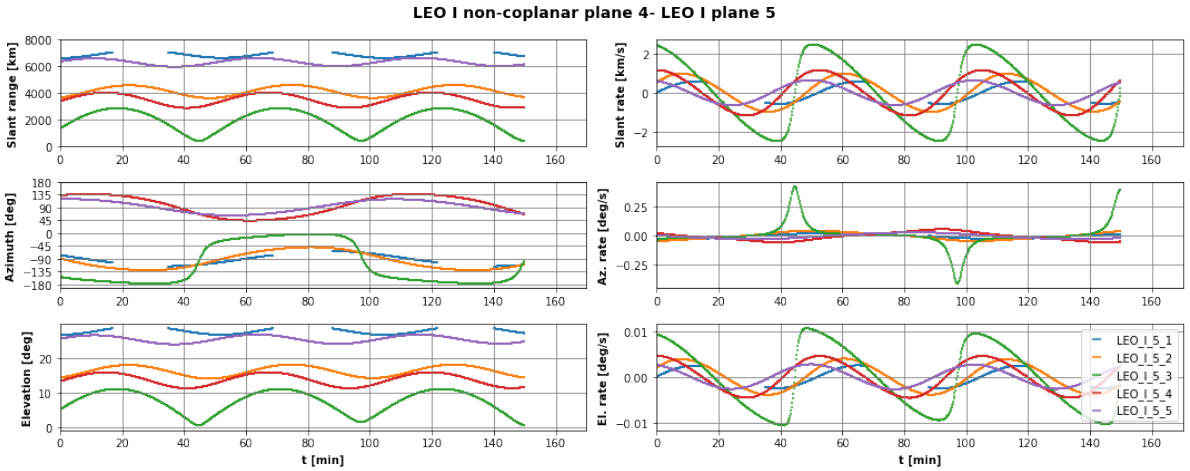

Figure 3.20: AER (left) and rates (right), using LF2 placement for LEO I near cross-plane links.

The remaining links have slant ranges which lead to the different communication window lengths and numbers of available links for the LCT1 and LCT2. Several links can be seen where the minimum slant range is barely below 5000 km, which explains why a large proportion of LEO I-LEO P LCT1 links were in the 0-5 minute region, while LCT2 was shown to have most links in the 5-10/15 minute region. Furthermore, as the orbital plane angles become larger, fewer links would appear to have slant ranges below 5000 km, which is why LCT2 registered 100 more links between a LEO I host and the LEO P shell. Overall, link patterns occur in the LEO I-LEO P links as were seen in LEO P- LEO I, with most links having medium lengths and average-fast dynamics.

LEO Inclined - MEO

The links between the LEO Polar host and the equatorial MEO satellites are shown in Figure 3.22. As was seen with the LEO Polar host, the link dynamics differ from LEO-LEO links in multiple aspects: the links are generally much longer (20 or 50+ minutes), slant ranges are all above 13000 km, elevation angles range over about 90 degrees and the azimuth ranges are about 90 degrees per link. In terms of link dynamics, the peak azimuth rates do not exceed +/- 0.4 deg/s, which again shows that angular rates are mainly linked to the relative speeds are proximity of the fly-by.

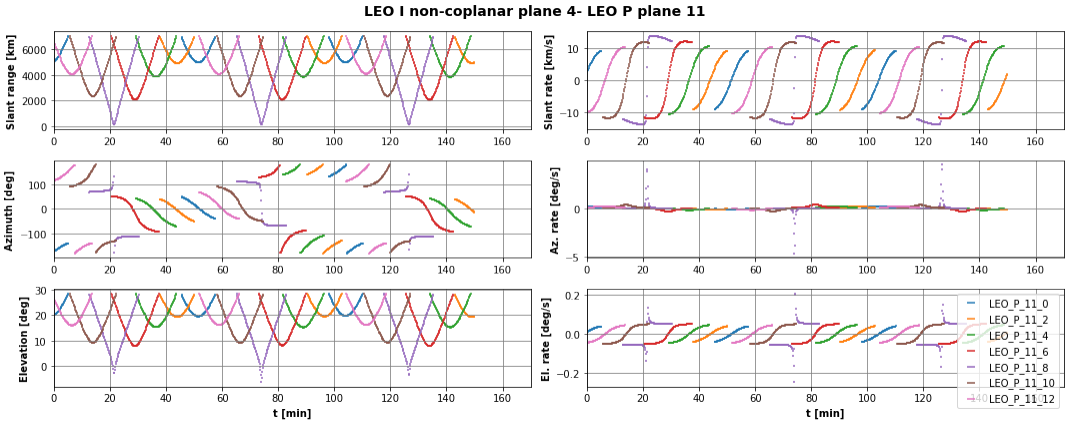

Figure 3.21: AER (left) and rates (right), using LF2 placement for LEO I-LEO P inter-shell opposite plane links with LEO P 11.

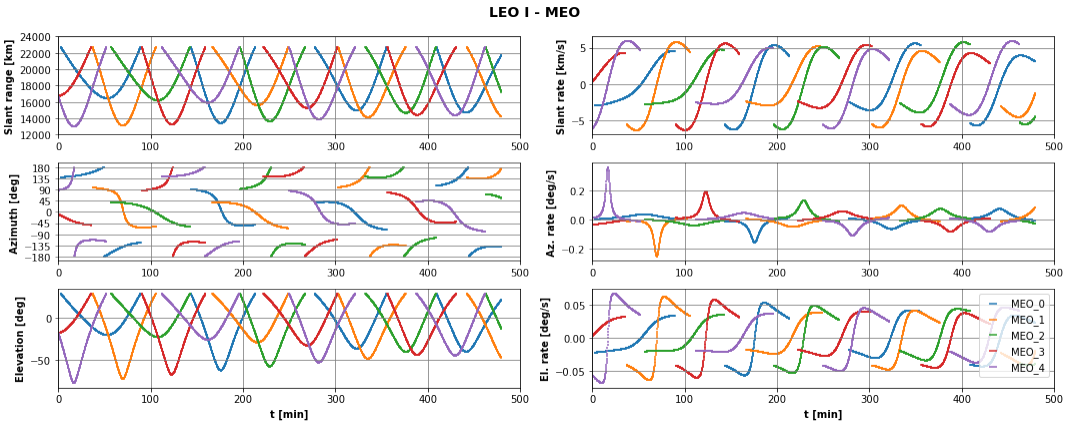

Figure 3.22: AER (left) and rates (right), using LF2 placement for LEO I-MEO links.

3.4. MEO host links

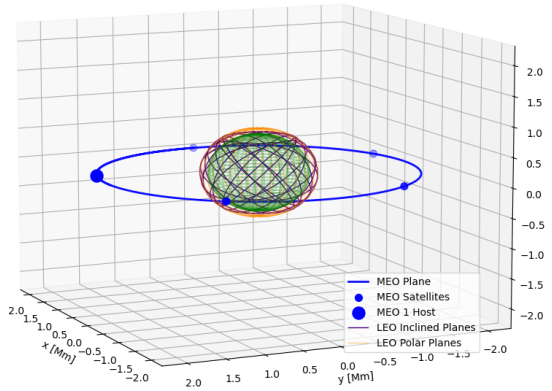

Figure 3.23: MEO Equatorial Host 1 satellite, showing the other MEO satellites, and both LEO shells.

The selected MEO Host is visualized in Figure 3.23. The MEO satellite with index 1 is considered the host in this chapter and only has a single index, as the MEO shell consists of one equatorial plane.

3.4.1. Communication Window Distribution

The link window distribution for the MEO host satellite using the LCT2 is shown in Figure 3.24. It is important to note that no links were registered using LCT1, due to the unachievable pointing angles that will be shown in subsection 3.4.2.

Compared to the LEO hosts, the link time distribution is very different. The vast majority of links to inclined LEO satellites are in the 60+ minute region, while the connections to polar LEO satellites also shown significant fractions of links in the 30-35 and 55-60 minute bins. In terms of MEO-MEO links, only a single leader/follower is linked and continuously available. It can thus be concluded that for MEO-LEO links, specifically long orbit prediction windows are the most relevant.

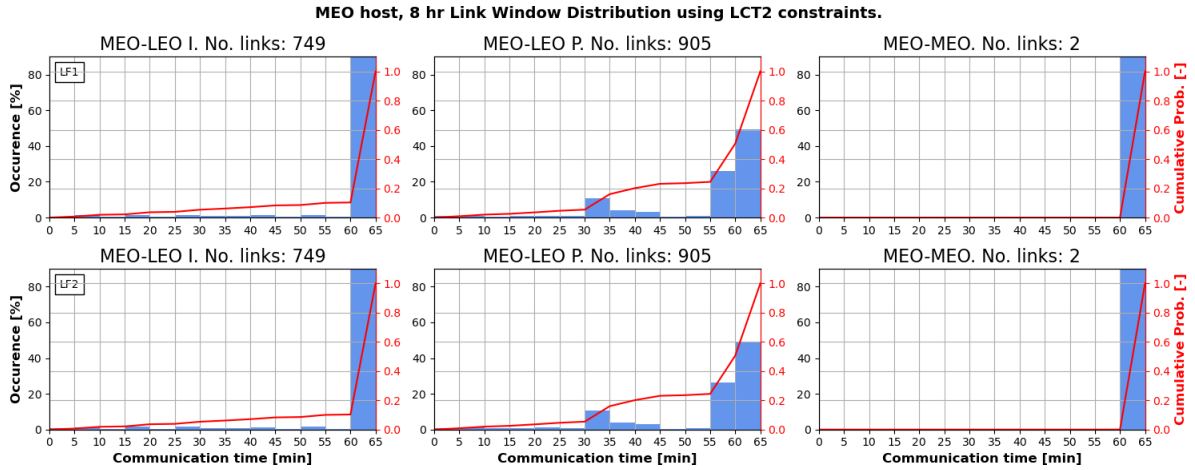

Figure 3.24: Communication window distribution for LCT2 in 2 terminal placements on the MEO satellite.

3.4.2. Available Link Distribution

The link established link distribution per orbital shell/plane for the MEO host using LCT2 is shown in Figure 3.25. In each case of MEO-LEO I links, it can be seen that a uniform distribution of links can be expected, with about 58 links per MEO orbital period. In contrast, the MEO-LEO P is also rather uniform, but exhibits consistently more links, closer to 70 with each plane. It would seem that this is due to the relative orientation of the MEO and LEO I/ LEO P orbital planes, which will be seen in subsection 3.4.3.

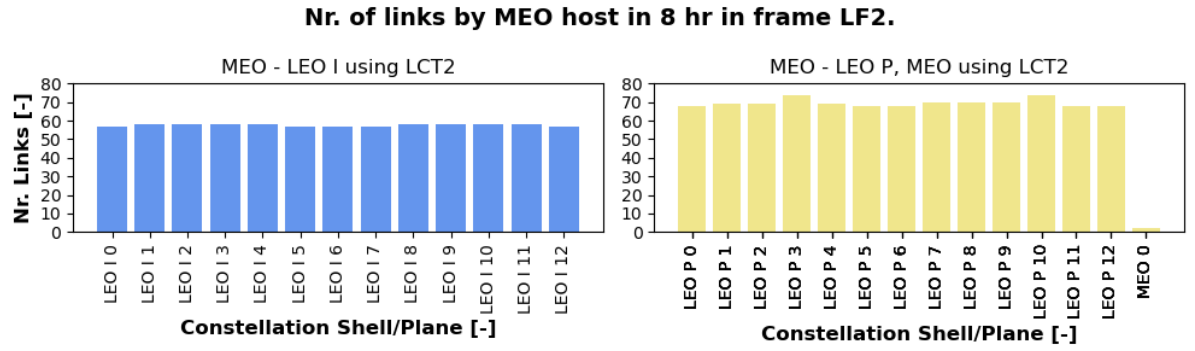

Figure 3.25: Available links per orbital plane for LCT2 placed at LF2 on the MEO satellite.

3.4.3. LISL Coarse Pointing Variables

MEO - MEO

The co-planar links for the MEO host satellite are shown in Figure 3.26. 2 links are in sight at all times, 1 ahead - with azimuth at 90 deg and 1 behind the host satellite, with azimuth -90 deg, slant ranges of 24000 km and elevations of 36 degrees. The pointing angles and slant ranges show smaller variations than in the LEO co-planar cases, with rates 1-4 orders of magnitude lower, which is due to MEO orbit

being equatorial and the reduced impact of perturbations due to the higher altitude. Overall, the MEO co-planar appear the least challenging.

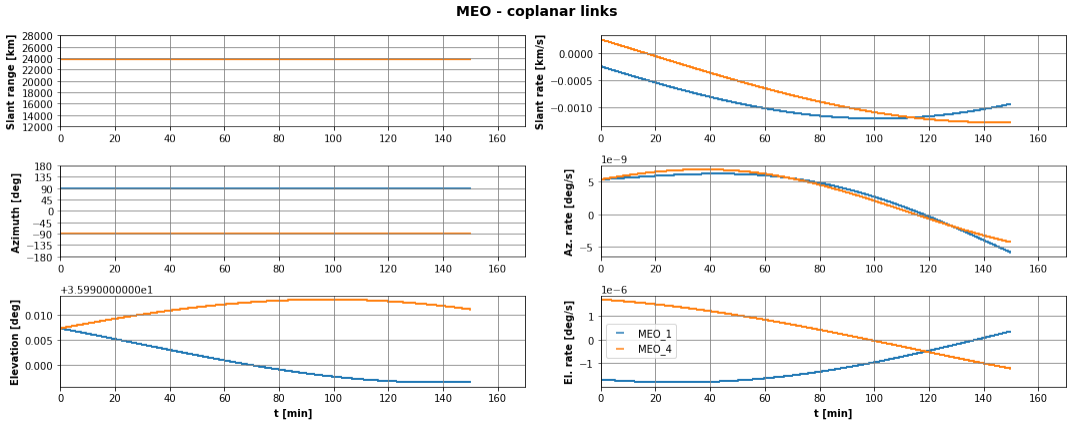

Figure 3.26: AER (left) and rates (right), using LF2 placement for MEO intra-orbit links.

MEO - LEO Inclined

The links to every 2nd LEO Inclined plane are shown in Figure 3.27. A clear elevation pattern, specific to MEO-LEO links can be seen in the elevation range- the range is relatively small 20 deg, though always relatively high, above 70 degrees and peaking at 90 in case of a complete overhead pass of the LEO target satellite. This was also the reason why no LCT1 links were detected, as the LCT1's maximum elevation limits are much smaller than the minimum MEO-LEO elevation angles.

Observing the azimuth values, the reason why most of the MEO-LEO I links are over 60 minutes, but a wide variety of shorter links occur too. The majority of the links (60+ minute) are because of the slow variation in slant range and the often constrained azimuth angles. The Earth occultation limitation mainly occurs for less than half of the LEO satellite orbit, meaning most links would be about 60+ minutes. Meanwhile, when the azimuth goes wraps from 180 to -180 deg, the link duration is split into two, leading to the shorter communication windows.

Most of the links show relatively slow dynamics with a small number of exceptions. The azimuth rates are mostly below +/- 0.3 deg/s, while elevation never exceeds +/- 0.03 deg/s. The few cases that do have higher azimuth rates (up to 2 deg/s) occur when the MEO host is approximately overhead of the LEO satellite, leading to an elevation close to 90 deg and a fast change in azimuth of 180 degrees. That was the case with the target LEO I in plane 2, index 4 at 50 minutes. The elevation increased nearly up to 90 deg, azimuth rapidly changed from -45 to 135 degrees and the slant-range reached the near minimum of 13000 km. This is among the most challenging MEO-LEO LISL cases.

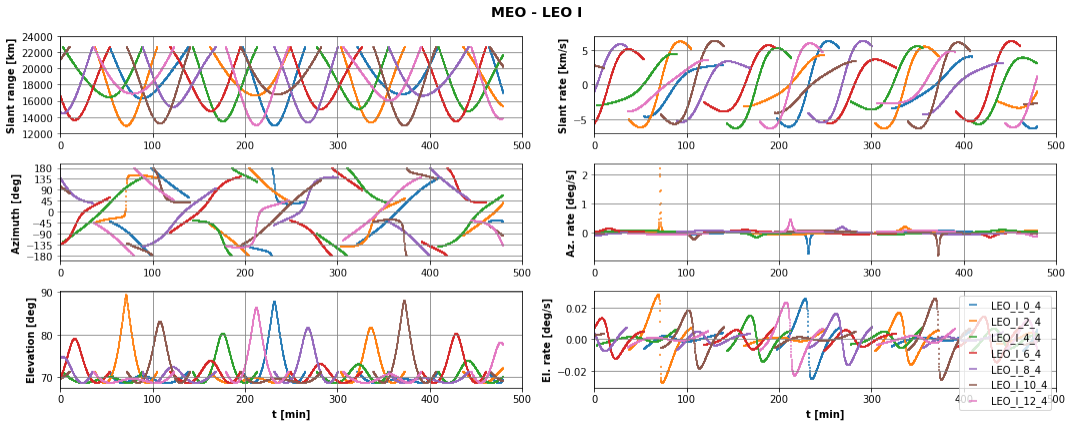

Figure 3.27: AER (left) and rates (right), using LF2 placement for MEO -LEO I links in every 2nd orbital plane.

MEO - LEO Polar

The links between the MEO host and the LEO Polar targets are shown in Figure 3.28. Comparing to LEO-LEO links, the same patterns of elevation and slant range can be seen as in the MEO -LEO I link case. Analyzing the azimuth angles, it can be seen that in nearly case the azimuth wraps around +/- 180 degrees. Due to how often this occurs, significantly more links are split into 55-60 and 30-45 minute windows, which was seen in Figure 3.24. This occurs due to the polar LEO and equatorial MEO being nearly perpendicular, unlike in the MEO - LEO Inclined case.

Besides the azimuth wrapping, the link variables are similar as in the LEO Inclined case. All- slant range, elevation and azimuth rates are within the same ranges. A single link case with LEO Polar plane 2, index 4 occurs where the LEO satellite flies nearly directly under the MEO host, leading to a fast azimuth rate of 2 deg/s. This is again a challenging case in MEO-LEO links.

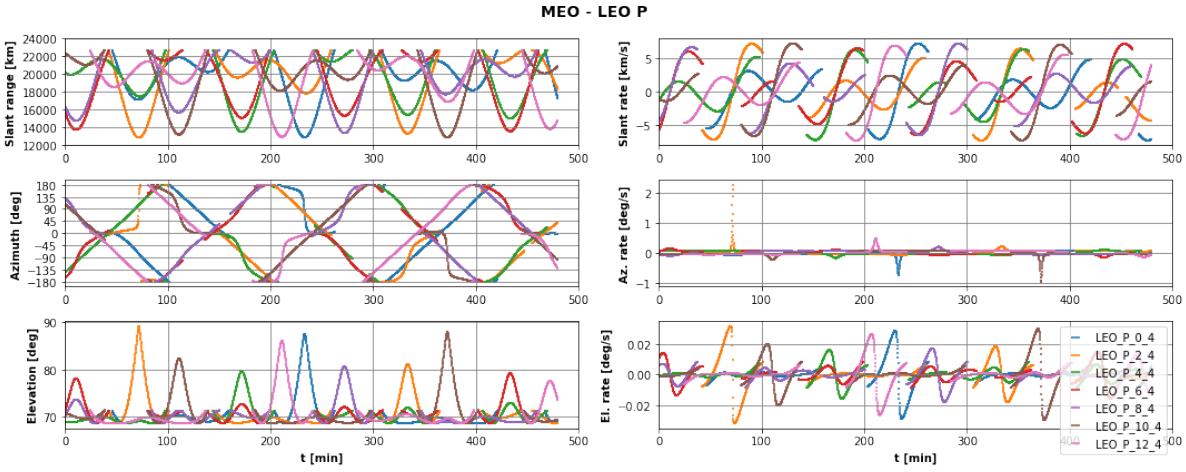

Figure 3.28: AER (left) and rates (right), using LF2 placement for MEO -LEO P links in every 2nd orbital plane.

3.5. Overview of Communication Windows

It must now be looked into what communication window length covers sufficiently many link cases for both terminals. Once determined, these communication window lengths will then be used as the required orbit prediction windows in the OD and OP algorithm design. This is first done for the LCT1 links in subsection 3.5.1, followed by checks for the LCT2 in subsection 3.5.2.

3.5.1. LCT1 link windows

The distribution of communication windows and the likelihood of a given link being within the specific window for LCT1 is shown in Table 3.2. Windows below 10 minutes cover over half of the LEO-LEO links and are already considered relevant for LCT1 Orbit Predictions despite not covering any LEO-MEO links. A longer window of 30 minutes already encompasses over 90% of every possible link case for the LCT1 and is also chosen as a relevant time window, specifically aimed for the LEO-MEO LCT1 links. Therefore, both 10 and 30 minute communication windows are selected for the LCT1 OP needs.

Table 3.2: Likelihood [%] of links being within communication window length for each link case using LF2 placement and LCT1.

Communication Window/ Link case	<10 min	<15 min	<30 min	<45 min	<60 min
LEO I-LEO I	52	74	90	94	95
LEO I-LEO P	69	83	95	100	100
LEO I-MEO	0	44	100	100	100
LEO P-LEO P	65	92	96	98	98
LEO P-LEO I	68	83	95	100	100
LEO P-MEO	18	64	91	91	91

3.5.2. LCT2 link windows

The distribution of communication windows and the likelihood of a given link being within the specific window for LCT2 is shown in Table 3.3. It can be seen the needed threshold will be longer than for the LCT1 terminal, as a 30 minute window does not cover half of any LEO-MEO or MEO-LEO links. If only a 10 minute window is considered, it would be sufficient for about 50% of LEO-LEO links, except in the LEO I intra-shell links. 30 minutes would cover the vast majority of LEO links. 45 minutes would cover about half of the LEO-MEO links, but would still be too short for most MEO-LEO links. Even at 60 minutes, many MEO-LEO links would be not be full supported, but it is not expected that 60+ minute communication would be needed in practical applications and therefore the 60 minute threshold is chosen for MEO-LEO, LEO-MEO and LEO-LEO co-planar links. For non-coplanar LEO links, 30 minutes will suffice.

Table 3.3: Likelihood [%] of links being within communication window length for each link case using LF2 placement and LCT2.

Communication Window/ Link case	<10 min	<15 min	<30 min	<45 min	<60 min
LEO I-LEO I	28	49	83	91	92
LEO I-LEO P	56	69	93	97	97
LEO I-MEO	0	0	0	50	62
LEO P-LEO P	55	68	92	94	95
LEO P-LEO I	53	67	92	97	98
LEO P-MEO	0	11	33	44	89
MEO-LEO I	2	2	5	8	10
MEO-LEO P	2	3	5	23	51

3.6. Selected Link Cases of Interest

In this section, the link cases selected to benchmark the OD-OP algorithms will be documented. The link cases were chosen to include the links with both with very basic and extremely difficult complexities. It was also important to include sufficient LEO-MEO and MEO-LEO links to test see if links can be established in both directions. Finally, both long and short communication window links were added.

The link cases are summarized in Table 3.4, briefly showing their lengths, angular rates and link distance ranges. This involves 3 link cases involving MEO satellites and 3 involving strictly LEO satellites.

Two link cases- 1 and 4 are co-planar, with 1 being between MEO satellites at 24000 km and 4 between LEO Polar at a constant 3500 km range. Cases 2 and 3 are between MEO and LEO satellites. The final cases 5 and 6 are dynamically fast links in LEO with close approaches. Each link case is described more thoroughly in the upcoming subsections.

Table 3.4: Overview of the 6 selected link cases to be used to benchmark the OD-OP algorithms.

Link nr.	Length [min]	Host	Target	Max AE Rate [deg/s]	Max. Link Dist. [km]	Min. Link Dist. [km]
1	60	MEO	MEO	0	24000	24000
2	60	MEO	LEO I	2	23000	13000
3	60	LEO P	MEO	0.3	22500	13000
4	60	LEO P	LEO P	0	3500	3500
5	20	LEO P	LEO I	4	7000	50
6	60	LEO I	LEO I	0.4	3300	100

3.6.1. Case 1 - Coplanar MEO-MEO link

A basic co-planar link between a follower and a leader MEO satellite is shown in Figure 3.29. In this link, constant pointing angles large link distance can be observed, which indicates favourable conditions for the PE contribution of the OD-OP algorithms. The link visualized in 3D can be seen in Figure 3.30 and can be seen to be roughly aligned with the along-track direction of the host orbit. This link case is expected to be least affected by the LOS predictions in terms of the resulting PE.

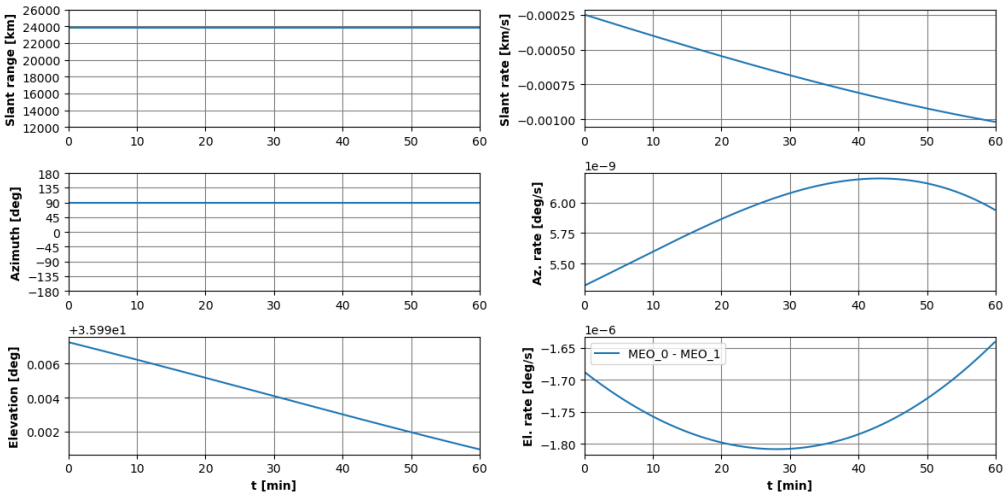

Figure 3.29: First link case between adjacent MEO satellites - AER (left) and rates (right), using LF2 placement.

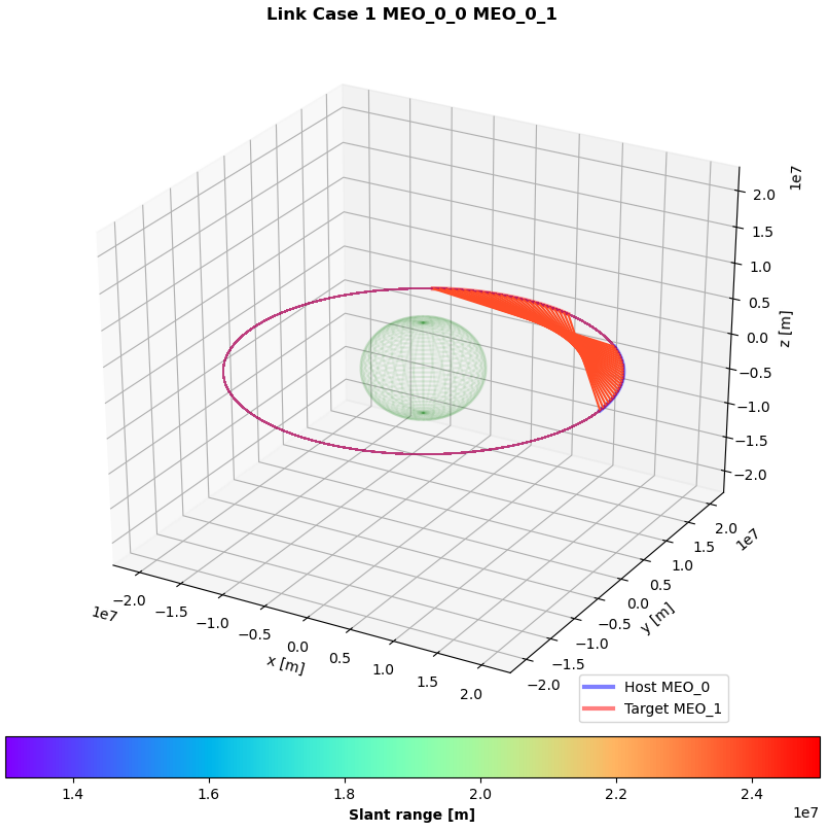

Figure 3.30: First link case between adjacent MEO satellites, visualized in 3D.

3.6.2. Case 2 - Inter-Orbit MEO - LEO Inclined link

The second link case was chosen to cover the MEO - LEO type with the link variables shown in Figure 3.31. In this case, a long window with fast angular dynamics dynamics can be observed, which peak at around 30 minutes after link start. Observing the relative geometry in Figure 3.32, it can be seen that the LEO target flies almost directly under the MEO host, which leads to the large spike in azimuth rates.

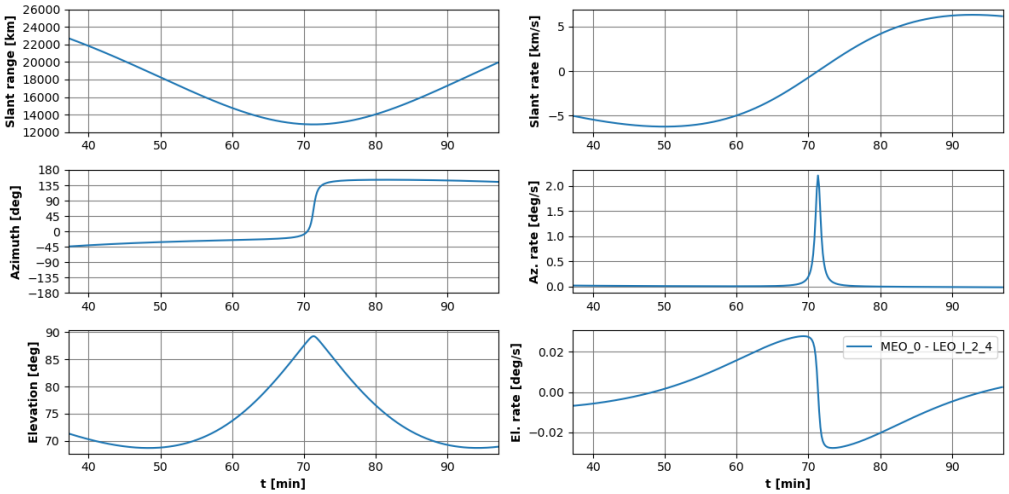

Figure 3.31: Second link case from MEO to LEO Inclined satellite at high elevation- AER (left) and rates (right), using LF2 placement.

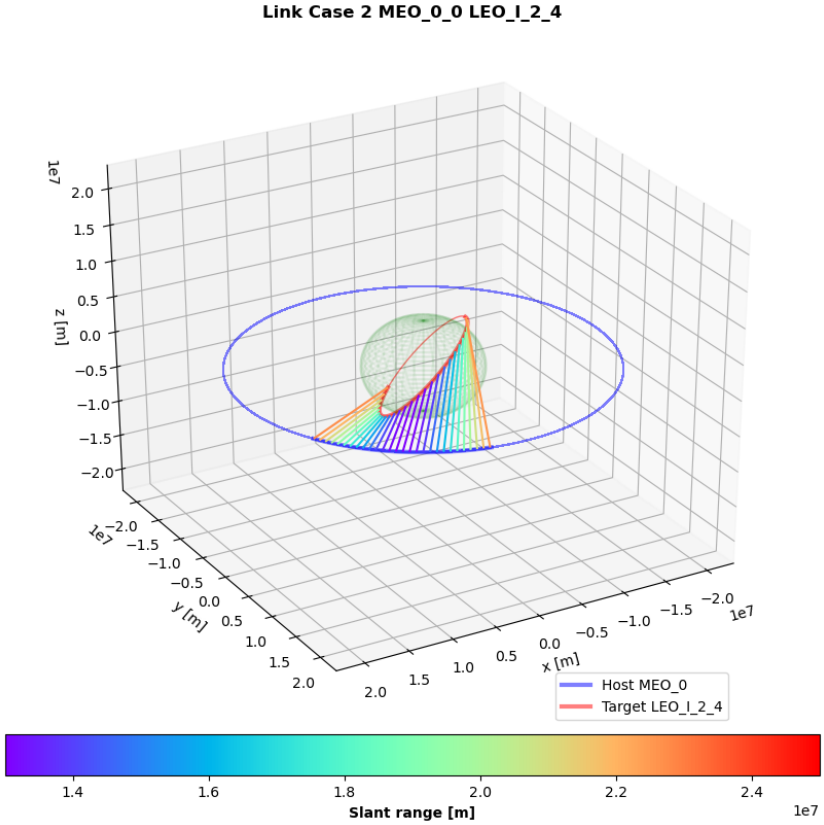

Figure 3.32: Second link case from MEO to a LEO Inclined satellite, visualized in 3D.

3.6.3. Case 3 - Inter-Orbit LEO Polar - MEO link

The third link case is another Inter-orbit link, but this time with the host in LEO, linking from the LEO Polar orbit to a MEO target. It is a medium-difficulty case in terms of angular rates, as seen in Figure 3.33, but it does present a long window. Again, the elevation reaches its minimum when the MEO host flies directly overhead, as can be seen in Figure 3.34

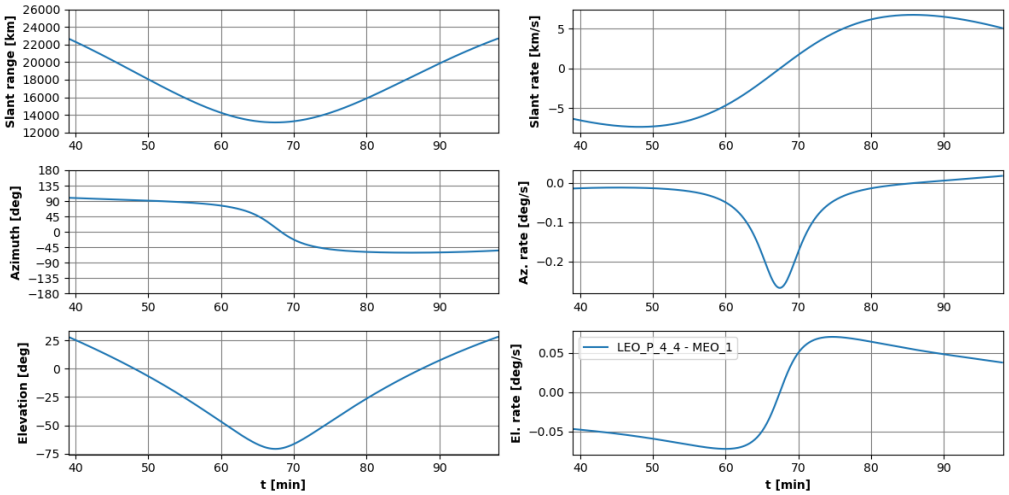

Figure 3.33: Third link case from Leo Polar to MEO with a med/high elevation pass - AER (left) and rates (right), using LF2 placement.

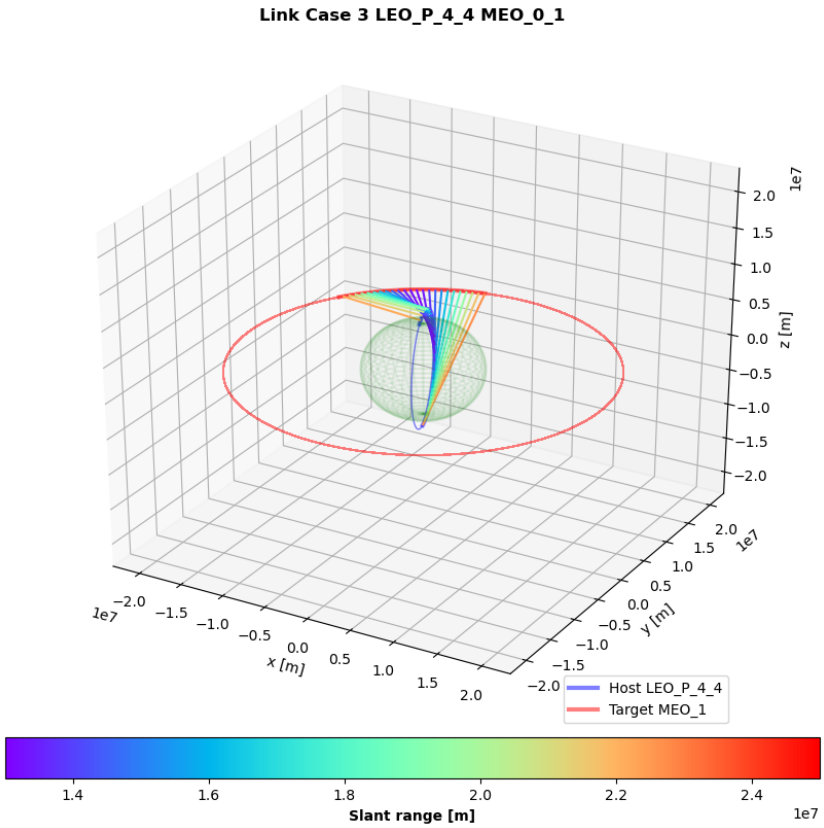

Figure 3.34: Third link case from Leo Polar to MEO, with the MEO satellite flying exactly overhead the LEO Polar host, visualized in 3D.

3.6.4. Case 4 - Intra-Shell LEO Inclined -LEO Inclined link

The fourth link case is a stark contrast to the links involving MEO satellites. As seen in Figure 3.35, the angular rates are much smaller with the azimuth and elevation staying pretty much constant. The link distance, however, is much shorter and thus orbit prediction errors will be a lot more significant in terms of their impact on the PE. The link is visualized in Figure 3.36, where the host and target share the same orbit and only have a true anomaly offset between them.

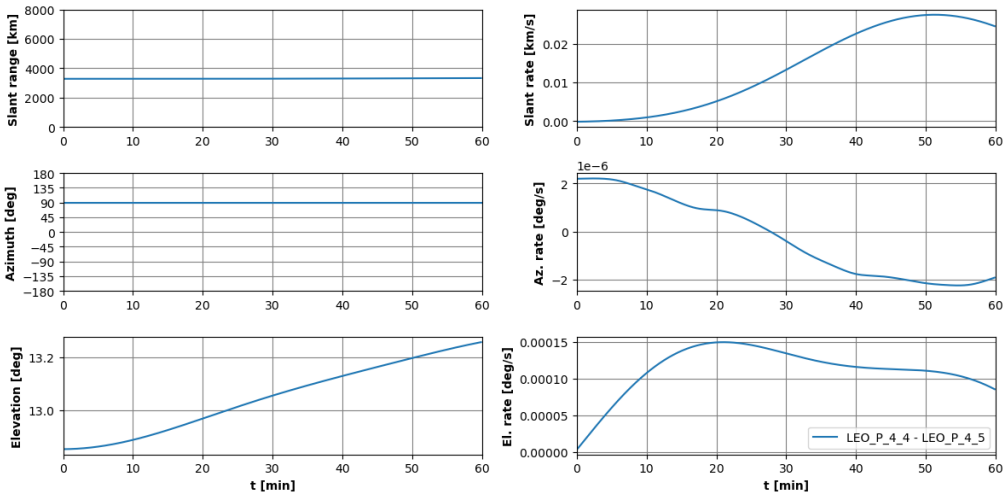

Figure 3.35: Fourth link case between adjacent LEO Polar satellites - AER (left) and rates (right), using LF2 placement.

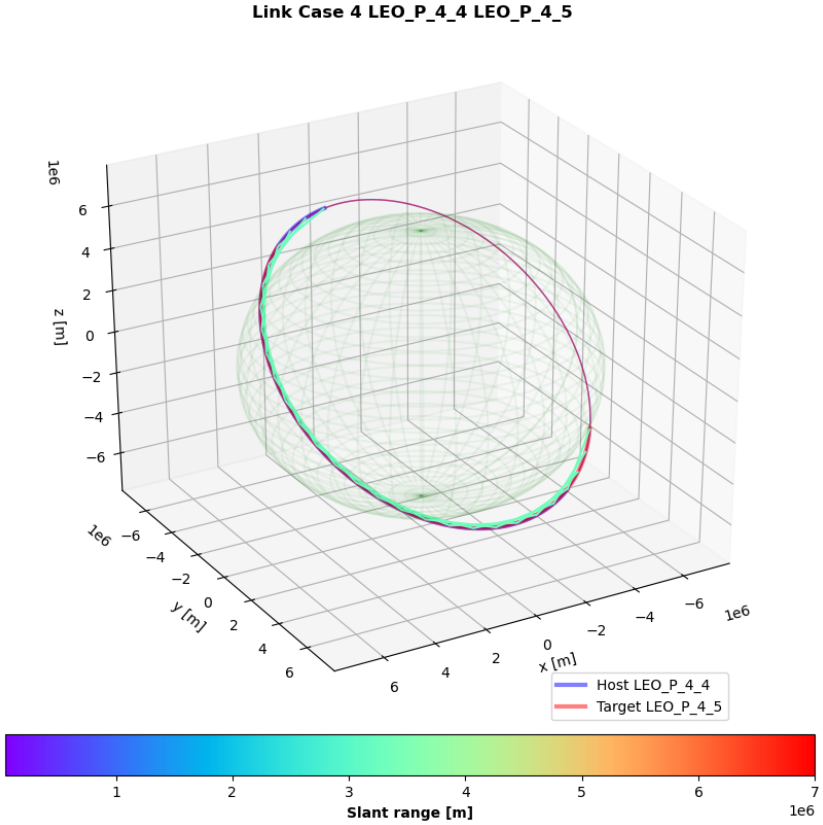

Figure 3.36: Fourth link case for two Co-planar LEO Polar Satellites, visualized in 3D.

3.6.5. Case 5 - Inter-Shell LEO Polar - LEO Inclined link

The fifth link case is a LEO link case with very challenging conditions. The link variables are shown in Figure 3.37- the communication window is much shorter, a total of about 20 minutes, but the angular rates are very fast. This is due to the opposite flight directions of the satellites and the extremely close approach that occurs in the middle of the link. This is visualized in Figure 3.38, where is can be seen that only in a short portion of the orbits, the satellites come close to each other.

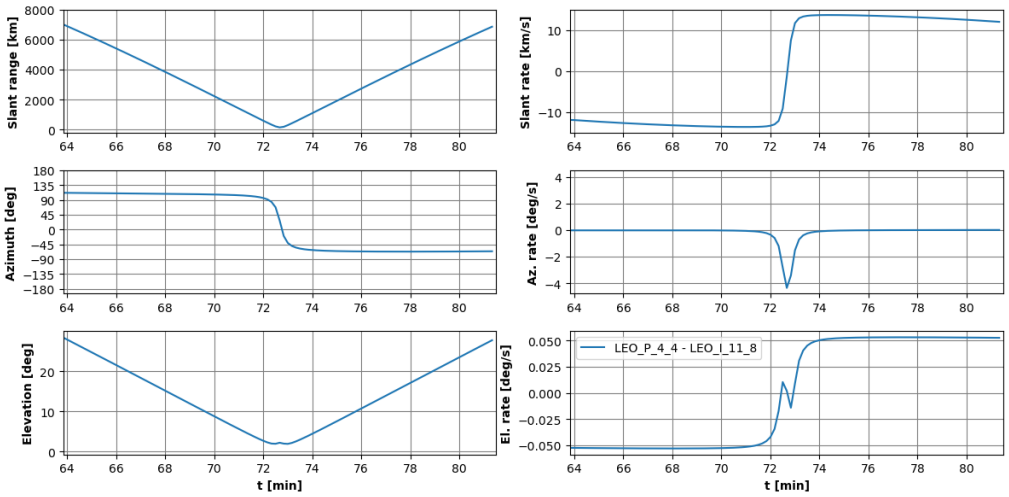

Figure 3.37: Fifth link case between LEO satellites, from Polar to Inclined- AER (left) and rates (right), using LF2 placement.

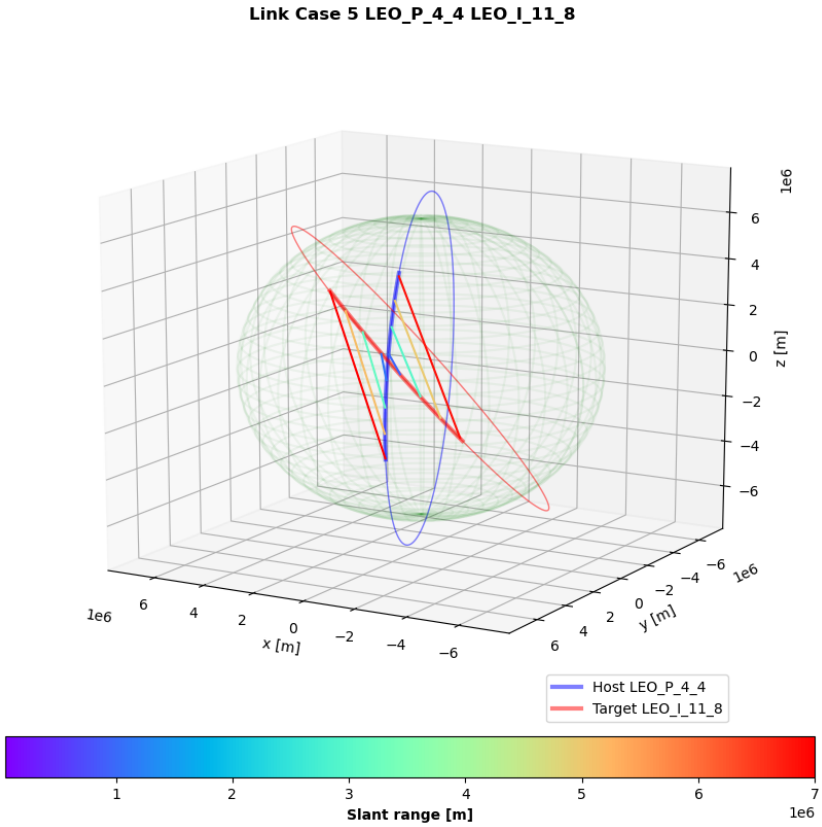

Figure 3.38: Fifth link case between LEO satellites from Polar to Inclined- AER (left) and rates (right), using LF2 placement.

3.6.6. Case 6 - Cross-plane LEO Inclined link

The final link case is a cross-plane link between two inclined LEO satellites in adjacent orbits. This link case is slightly easier in terms of pointing angles and slant rates than the previous LEO link case. The pointing angles and rates can be seen in Figure 3.39. Although the minimum link distance gets quite close, for the remaining portion of the orbit the angles remain rather constant. Nonetheless, due to the smaller link distances, it is expected that this will be a medium-difficult link case in terms of PE due to OD OP errors. This link geometry is visualized in Figure 3.40, where it can be seen that the link is almost constant, pointing in the cross-track direction, until the link direction swaps in the high latitude portions.

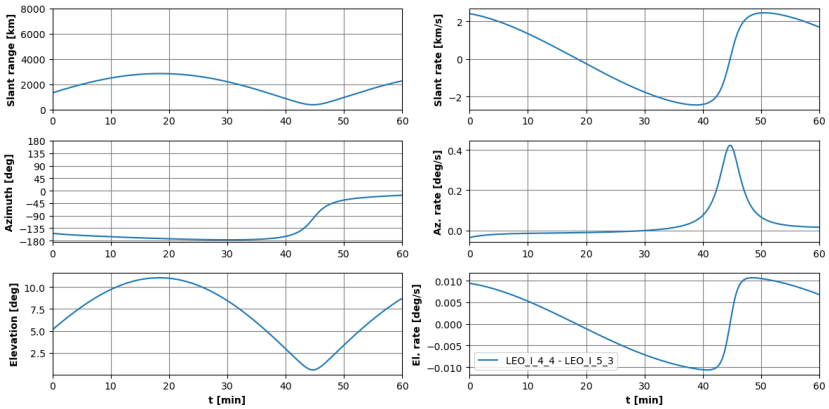

Figure 3.39: Sixth link case between LEO Inclined satellites in adjacent orbital planes- AER (left) and rates (right), using LF2 placement.

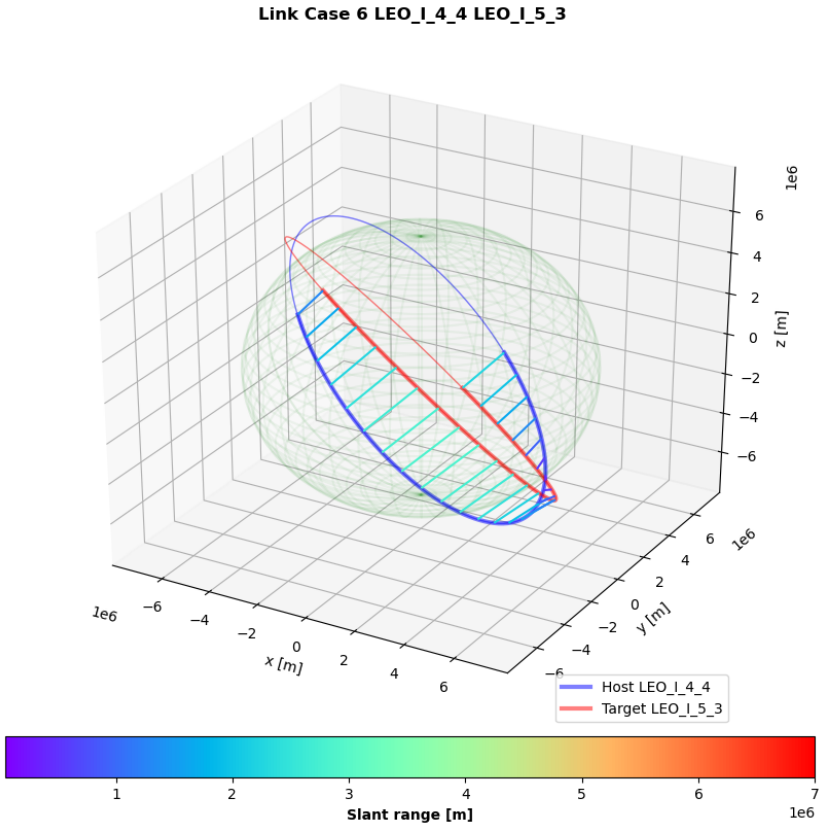

Figure 3.40: Sixth link case for a cross-plane LEO Inclined link, visualized in 3D.

3.7. LISL Geometry Conclusions

In this section, the conclusions relating to the originally formulated RQ1 will be summarized. This is done to each sub-question, leading to an overall answer to the central research question regarding the LISL properties in the LEO/MEO satellite constellation.

1 a). *What are the available communication window time distributions for the intra-orbit, inter-orbit and inter-shell in LEO-LEO, MEO-MEO, LEO-MEO and MEO-LEO links?*

Intra-orbit LEO Polar host and LEO Inclined host links were found to be continuously available for LCT2 regardless of nominal terminal placement/orientation. LCT1 could only continuously cover co-planar links in the nominally cross-plane facing orientations LF2 and LF4.

Inter-orbit LEO Polar links were mostly in the 10-15 minute region, with over 50% of all link windows being in that range for LCT1. For LCT2, more and longer inter-orbit links were detected with 50% of them occupying the 10-20 minute range. Most short links occurred with targets flying in the opposite direction. For both terminals, link opportunities also occurred in the 20-60 minute range, however, these were only about 5-10% of all link opportunities.

Inter-orbit LEO Inclined host links were generally shorter and fewer than LEO Polar host links. With LCT1, 40% of links were 0-10 minutes and 40% more in the 10-15 minute window. A total of 150 links were detected over 2 hours with LEO Inclined satellites with LCT1, whereas the LEO Polar host registered about 250 links under the same constraints. The reason for this was that fewer links can be reached with the opposite-flight satellites. While the LEO Polar host can link with opposite plane LEO targets throughout the entire orbit, for the LEO Inclined host this is only possible near the equator and in the mid-latitude regions, due to the larger link distances and earth occultation around the high latitude regions.

Inter-shell LEO links were found to be generally shorter than inter-orbit LEO links. About 90% of LEO P - LEO I links were 15- minutes with LCT1 and 25- minutes with LCT2. The same was true for LEO I - LEO P links. Fewer links occurred in the 20-60 minute regions and only LCT2 could support 60+ minute inter-shell LEO links.

Few inter-shell and mostly longer LEO-MEO links opportunities were found. In all cases, 8-9 link windows were detected over 2 hours. LCT1, LEO I - MEO links were mostly 10-30 min and for LEO P - MEO, the link windows were either 20- minutes or 60+ min long. With LCT2, the available windows became longer, for both LEO I- MEO and LEO P-MEO becoming mostly 40+ minutes.

In contrast, many more opportunities were seen from the MEO satellite's point of view. Over 8 hours, 750+ link windows were found to LEO satellites and mostly in the 55+ minute regions. In case of MEO-MEO links, only the leading and trailing satellites are available due to Earth occultation. Furthermore, links only with LCT2 were possible due to the 10000+ km link distances.

1 b). *What are the critical communication time cut-offs in terms of available communication windows?*

In addition to the 100 second acquisition window, 3 cut-offs were chosen based on link availability windows. A 10 minute cut-off was chosen as it it covered 50-70% of link windows LEO-LEO links for the LCT1. A 30 minute cut-off was also chosen as it covered 90+% of all LCT1 link windows and 80-90% of LEO-LEO links for LCT2. Finally, a 60 minute window was chosen as the longest cut-off for the long and continuously available links.

1 c). *What are the ranges and rates of azimuth, elevation and link distance for the intra-orbit, inter-orbit and inter-shell in LEO-LEO, MEO-MEO, LEO-MEO and MEO-LEO links?*

Intra-orbit LEO Polar and LEO Inclined links both had roughly constant pointing angles and link distances. The link distances were about 3700 km and 6200 km. Angular rates were less than 0.1 mdeg/s. Slant rates were about 50 m/s or less. Any longer links were geometrically impossible due to Earth occultation.

Inter-orbit LEO Polar host links to the opposite plane were found to have much faster dynamics. Azimuth angles were found to cover the entire field of view, while elevation was constrained between 0 and 30 degrees. Slant rates were up to 10 km/s and elevation rates reached a maximum of 0.05 deg/s. Azimuth rates varied drastically based on the minimum link distance. In most challenging cases, azimuth rates of over 2 deg/s were observed.

Inter-orbit LEO Inclined host were also found to have faster dynamics, but fewer cases of close approaches were found. For links between Plane 4 and Plane 11, Azimuth angles again covered -180

to +180 degrees and elevation varies between 0 and 30 degrees. The slant rates were also up to 10 km/s, while azimuth rates were lower and rarely exceeded 0.5 deg/s. Elevation rates were found to be within 0.04 deg/s.

LEO-MEO links lead to vastly different geometries. In terms of link distances, they varied between a minimum of about 13000 km to a maximum of over 22000 km. The slant rates reached a maximum of about 5 km/s. Azimuth angles covered the entire field of view but generally changed at slower rates, never exceeding 0.4 deg/s. The elevation angles covered a wide range from the LEO satellite's view, with the entire elevation range being about 90 deg. The elevation rates were again slower than azimuth, reaching a maximum of about 0.05 deg/s.

In case of MEO satellites, in intra-orbit links, a constant link distance of 24000 km occurred with the pointing angles also being static. MEO-LEO links had slightly different conditions than LEO-MEO links. While azimuth covered the entire range, rates of up to 2 deg/s occurred with both LEO Inclined and polar targets, which were much faster. The elevation range was a lot less, only being about 20 degrees- ranging from 70-90 degrees with both Polar and Inclined targets. The elevation rate, however, was lower, reaching about a maximum of about 0.03 deg/s.

1 d). *How many links of each type can be established by satellites in LEO and MEO to each orbital plane per orbital revolution?*

For a LEO Polar host, 2 and 4 co-planar links were possible with LCT1 and LCT2, respectively. For inter-orbit links, further planes lead to consistently more links being detected. With LCT1, about 5 links were possible with Planes 3/5, 10 links with 1/2/6/7. About 15 with planes 0 and 8 and 35-50 with planes 9-12. When LEO Polar-LEO Inclined links were considered, about 10-15 links were found to be possible to planes 0-8 and about 30 to planes 9/12 with LCT1. LCT2 lead to consistently more links, reaching up to 30 with plane 8 and 50 links with planes 9 and 12. With the opposite planes 10 and 11, about 50 links were found for both terminals.

For a LEO Inclined host, the same was found with co-planar links. For inter-orbit links, fewer opportunities were found and only up to 25 links were detected with the opposite planes 10-11 for LCT1 and up to 35 using LCT2, which was due to the much longer link distances occurring between LEO Inclined satellites. With LEO Polar targets, up to 50 links were found with the opposite planes, as the link distances around the high latitude regions were now less.

Considering MEO satellites, the same number of opportunities were found with each LEO orbital plane but there was a difference between the two shells. For MEO-LEO Inclined shell, about 55 links were detected in 8 hours with every plane. In contrast, with each LEO Polar shell, up to 70 links were found in the same time. For MEO co-planar cases, the 2 continuously available links were detected.

4

GNSS-based OD performance

In the previous chapter, the link geometry, prediction window and link case aspects of OD-OP for LISL have been described. Now, the OD aspect must be looked into. The observed performance of various OD schemes will now be looked into. This is done with 2 goals- 1) testing novel Kalman Filters for the first time with flight data and 2) comparing and quantifying expected pseudorange-based KF performance for subsequent Orbit predictions. First, the GNSS flight and precise orbit data used is described in section 4.1. In section 4.2, an overview of the performance of every analyzed dynamic filtering method will be presented. Furthermore, expected results for carrier-phase based kalman filters is collected from literature. Lastly, is discussed how these results would apply to use cases in satellite constellations when considering the performance of COTS GPS receivers. Subsequently, in section 4.3 the novel filters are focused on, first presenting their performance with flight data at different update intervals, followed by a discussion and analysis of their shortcomings. Finally, an overview of the results and answers to the second RQ are presented in section 4.4.

4.1. Used GNSS Flight Data

In order to evaluate Novel filters with flight data, GNSS measurements were needed as inputs and precise orbits were required to test the filters' accuracy. For these purposes, Gravity Recovery and Climate Experiment Follow-On (Grace-FO), Jason-3 and CHAllenging Mini-Satellite Payload (CHAMP) data was used. Additionally, HY2A precise orbit data was used to verify the orbit prediction algorithms, as the HY2A orbital parameters match the analyzed constellation's LEO Polar satellites altitude and inclination.

To evaluate the applicability of each satellite's data to the report outcomes, the orbital parameters need to be considered. These are shown for each satellite in Table 4.1. While all sets of GNSS measurements are applicable to test the Novel Kalman Filters, only a single set will be used to quantify the PR-based KF performance for subsequent OP. The results derived when using Jason-3 data will be used for this purpose, as its higher orbit better represents the LEO constellation satellites, which at 1000 km will be affected significantly less by drag and slightly less by the perturbing Earth gravity terms.

Table 4.1: Rough satellite orbital parameters derived from the precise orbit data and timestamps of the datasets used for Filter Tuning and testing/verification purposes.

Satellite	Altitude [km]	Inclination [deg]	Orbital Period [hr]	Data datestamp Testing [YY-MM-DD]	Data datestamp Tuning [YY-MM-DD]
Grace-FO	530	89	1.65	18-09-01	18-07-02
CHAMP	440	87.18	1.56	01-01-10	01-01-30
Jason-3	1337	66	1.87	19-12-31	19-05-17
HY2A	971	99.35	1.74	11-10-07	-

GRACE-FO data is archived by Jet Propulsion Laboratory's Physical Oceanography Distributed Active Archive Centre (PODAAC) and was accessed through [1], after being granted Earth Data login

details. Level-1B data was used, which is made available to the scientific community [31]. GPS1B and GNV1B files were used, the GPS1B includes three PR and CP measurements (CA, L1, and L2) [31], although only the L1 PR was used. GNV1B was used for Precise Orbit solutions and are documented to be accurate to the cm-level [75]. These files contain the position and velocity solutions in ECEF and were used to evaluate the OD and OP method accuracy.

The data for CHAMP are archived by GeoForschungZentrum (GFZ) Potsdam and public data is accessible through an fps server. The Rapid Science Orbits were used as precise orbits, which are indicated to be accurate to 1-2 cm [53].

Jason-3 is the follow-on mission from TOPEX/Poseidon Jason-1 and OSTM Jason-2 missions, co-operated by the French Space Agency CNES, NASA and European Organisation for the Exploitation of Meteorological Satellites EUMETSAT. Its GNSS measurements and Precise Orbit orbits were accessed through AVISO+ data services `http://www.aviso.altimetry.fr`. The precise orbits are indicated to have accuracies better than 5 cm 3D RMS [26]. HY2A Precise Orbits were also downloaded from AVISO+ servers to be used as verification data in the next chapter, due to the mission's similar orbital parameters to the simulated LEO Polar host satellite.

4.2. Expected GNSS-OD Performance

In this section, the expected GNSS-based OD method performance that will later be applied for subsequent OP will be described. First, the KF settings will be looked into in subsection 4.2.1, which will include theoretical and tuned settings for each implemented KF. Subsequently, in subsection 4.2.2, the performance of the analyzed filters will be presented with the tuned/theoretical KF settings, as well as the potential filter performance with ideal measurement selection. Then, Carrier-phase based KF performance found in a literature search will be described in subsection 4.2.3. Finally, in subsection 4.2.4 the previously shown results will be applied to a Satellite Constellation by considering COTS GPS receivers specifications. This will allow to draw conclusions regarding more realistic expectations for GNSS-OD performance in the considered satellite laser communication.

4.2.1. Kalman Filter Settings

In this subsection, the KF settings will be documented. First, the settings used pre-tuning will be shown based on theoretical expectations and followed by settings found in basic offline tuning using a grid-search algorithm.

Theoretical Settings

The theoretical filter settings are presented in Table 4.2. These settings were selected based on the expected measurement uncertainty and expected prediction errors.

Considering the measurement noise matrices, the EKF, SPUKF and UKF all had a diagonal R matrix of 25, which represents the squared value of the expected measurement uncertainty. In this case, it was the expected precision of the used SF pseudorange measurements. In [66], the largest magnitude GNSS measurement error component listed is the 1st order Ionospheric error, up to 30 m. However, a more conservative value is used for the noise matrices of 5 m, to avoid the filter being too insensitive to measurement updates [68]. The measurement noise is kept consistent among these filters as they use the same measurement. In contrast, the PEKF is assigned a larger magnitude R, as the measurements are the coarse position kinematic solutions. Testing the NRM errors with the flight data, they are not expected to have a better precision than 15 meters and the noise matrix is set accordingly.

The Process Noise matrices were kept relatively low for EKF and PEKF and larger for UKF and SPUKF. These represent the added uncertainty of the orbit prediction step. It adds to the covariance of the filter, thus increasing the Kalman gain and keeping the filter sensitive to new measurements [36]. For the EKF and PEKF, they are kept minimal, as only a single point is propagated and for a relatively small time-step of 10 s. For the UKF, a 10 times larger Q is used, as multiple sigma points are propagated and summed, thus the total prediction uncertainty should be higher. Q is further increased for the SPUKF, as it also makes predictions using multiple sigma points, but the non-mean representing sigma points are propagated in a simplified manner, further increasing the expected uncertainty.

For the unscented filters, an additional parameter is λ, which controls the weighing of the sigma points. Higher value puts more weight on the sigma point representing the mean state and less on the other sigma points. Theoretically, a value of $3-N$ is recommended [28] where N represents the number

of estimated states. However, this results in a negative weight for 0th sigma point, which in turn leads to the covariance estimate no longer being positive semi-definite. That is an issue, as the UKF/SPUKF implementations use Cholesky decomposition to determine the square root of the covariance estimate and this leads to the code crashing if the estimated covariance is not positive semi-definite. Therefore, the theoretical recommendation was not applicable in this case. Other options for λ values are not well documented and hard to come by in literature. A positive value of 32 is chosen, which is representative of the value used in the GPS-based OD using UKF in [16], which leads to a weight of about 0.2 for the 0th sigma point.

Table 4.2: Theoretical filter settings used.

Filter	Process Noise	Measurement Noise	Lambda
EKF	[10, 10, 10, 1, 1, 1, 10]	[25, 25, 25, 25]	-
PEKF	[10, 10, 10, 1, 1, 1, 10]	[225, 225, 225, 225]	-
UKF	[100, 100, 100, 10, 10, 10, 100]	[25, 25, 25, 25]	32
SPUKF	[200, 200, 200, 20, 20, 20, 200]	[25, 25, 25, 25]	32

Tuned Settings

Each of the filters were tuned offline, using 2 hours of flight on a separate date. A basic grid-search method was used, running the filters with different combinations of Q and R matrices (and lambda values for the unscented filters) and minimizing 3D RMS errors as the objective. Precise orbit data for each satellite was used to quantify filter performance and determine which filter settings lead to the lowest errors.

The tuned settings are presented in Table 4.3, which are very different from the theoretical settings presented in Table 4.2. The extended filters leaned towards smaller R values and a wide range of Q values, generally putting more trust on the measurements. The settings also differed significantly between the satellites, up to 2 orders of magnitude for Q. The unscented filters settings were largely consistent with low R and large Q matrices, as well as large lambda values. This leads to the filters being very sensitive to measurement updates and putting large weights on the 0th sigma point in the prediction step.

Table 4.3: Filter settings tuned off-line.

Filter	Satellite	Process Noise	Measurement Noise	Lambda
EKF	CHAMP	[50, 50, 50, 5, 5, 5, 50]	[0.4, 0.4, 0.4, 0.4]	-
EKF	GRACE-FO	[0.78, 0.78, 0.78, 0.08, 0.08, 0.08, 0.78]	[0.4, 0.4, 0.4, 0.4]	-
EKF	Jason-3	[25, 25, 25, 2.5, 2.5, 2.5, 25]	[0.4, 0.4, 0.4, 0.4]	-
PEKF	CHAMP	[570, 570, 570, 57, 57, 57, 570]	[0.02, 0.02, 0.02, 0.02]	-
PEKF	GRACE-FO	[250., 250., 250., 25., 25., 25., 250.]	[0.15, 0.15, 0.15, 0.15]	-
PEKF	Jason-3	[25, 25, 25, 2.5, 2.5, 2.5, 25]	[85, 85, 85, 85]	-
UKF	CHAMP	[260, 260, 260, 26, 26, 26, 260]	[1.92, 1.92, 1.92, 1.92]	300
UKF	GRACE-FO	[29, 29, 29, 2.9, 2.9, 2.9, 29]	[1.92, 1.92, 1.92, 1.92]	300
UKF	Jason-3	[87, 87, 87, 8.7, 8.7, 8.7, 87]	[1.92, 1.92, 1.92, 1.92]	300
SPUKF	CHAMP	[260, 260, 260, 26, 26, 26, 260]	[0.64, 0.64, 0.64, 0.64]	300
SPUKF	GRACE-FO	[260, 260, 260, 26, 26, 26, 260]	[0.64, 0.64, 0.64, 0.64]	300
SPUKF	Jason-3	[260, 260, 260, 26, 26, 26, 260]	[0.64, 0.64, 0.64, 0.64]	300

4.2.2. Overview of Implemented Filter Performance

The implemented filter performance will first be shown when using theoretical KF settings. Subsequently, this will be repeated with the tuned settings and finally, potential filter performance using idealistic GPS measurement selection will be presented.

Performance with Theoretical Noise Matrices

The performance of each implemented filter for 2 hours of flight data is presented in Table 4.4 using theoretical filter settings, showing the standard deviation in the R radial, S along-track and W cross-

track error components and the 3D RMS for position and velocity. Focusing on the 3D RMS errors, a wide range of accuracies can be seen. Several tendencies can be pointed out.

First, the original PEKF and the new PEKF using the NRPC method consistently perform identically in terms of accuracy, for all sets of flight data. This should not come as a surprise, as the intended purpose of the improved NRPC-PEKF was to reduce CL and not to improve precision.

The performance of each filter differs per satellite, but some tendencies can be seen. In general, it appears that the standard EKF leads to the best accuracy, with PEKF or the UKF coming close, while the SPUKF leads to the worst accuracy. For CHAMP, the EKF, UKF and PEKF lead to large 3D RMS errors of over 100 m. For Grace-FO, much better results can be seen with the EKF leading to 3D RMS errors below 10 m, UKF below 20 m and PEKF just above 20 m. Finally, for Jason-3, all filters have an accuracy around 50 m 3D EMS, with PEKF slightly outperforming EKF.

Table 4.4: PR-based KF OD errors for CHAMP, Grace-FO and Jason-3 L1 GPS measurements, using theoretical filter settings and J2 dynamical model. Showing the standard deviation for each state component in the RSW (Radial, along, cross-track) and the 3D RMS. *9% of orbit solutions diverged and were excluded from accuracy computation.

Filter	Sat.	Position [m]				Velocity [cm/s]			
		R	S	W	3D	R	S	W	3D
PEKF	CHAMP	65.2	52.7	52.9	101	378.1	685.7	249	822.5
NRPC-PEKF	CHAMP	65.2	52.7	52.9	101	378.1	685.7	249	822.5
EKF	CHAMP	59.7	33.6	16.3	71.3	171.8	123.3	75.5	224.6
UKF	CHAMP	72.9	47.2	20.9	90.4	195.6	136.8	90.2	255.3
SPUKF	CHAMP	114.3	65.7	37.3	137.9	2023.4	1093.5	688.3	2434.2
PEKF	GRACE-FO	8.6	19.4	8.4	23.2	32.8	98.3	89	186.5
NRPC-PEKF	GRACE-FO	8.6	19.4	8.4	23.2	32.8	98.3	89	186.5
EKF	GRACE-FO	5.8	5.8	1.9	8.4	9.9	11.5	6.7	18.8
UKF	GRACE-FO	5.7	5.7	1.9	8.3	10.3	11.5	6.9	19
SPUKF	GRACE-FO	5.3	5.7	1.8	8	21.5	22.4	44.1	86
PEKF	Jason-3	31.8	24.7	23.4	47	120.1	111.3	148.5	265.1
NRPC-PEKF	Jason-3	31.8	24.7	23.4	47	120.1	111.3	148.5	265.1
EKF	Jason-3	31.3	26.7	23	47.9	113.7	215.8	231.3	335.9
UKF	Jason-3	26.7	28.8	24.9	47.3	131.8	228.5	219.2	342.7
SPUKF	Jason-3	22.6	20.3	30.2	43.1	476.8	407.8	148	669.4

The 3D position errors over time for the GRACE-FO and Jason-3 datasets can be seen in Figure 4.1. Observing the filter performance for the GRACE-FO data, the orbit errors are mostly below 20 m, with some excursions above this threshold. In portions where the accuracy degrades, the EKF appears to be least prone to increase in error. In comparison, the accuracy is a lot less stable for Jason-3 data, although many of the solutions still remain below 20 m errors for all filters.

Performance with Tuned Noise Matrices

The performance of each implemented filter for 2 hours of flight data is presented in Table 4.5 using tuned filter settings. It is important to again note, that the filters were tuned for a separate period of flight data taken on another day and the results shown here are for a separate period, representing the test dataset.

Firstly, just as seen with the theoretical settings, the original and NRPC-PEKF implementations perform identically. A deeper discussion on the reasons and the comparison of the two PEKF implementations are presented in subsection 4.3.2.

Comparing the implemented filter performance to the outputs using theoretical filter settings, differing results can be seen. While some filter/satellite combinations improve significantly. SPUKF specifically improves- for CHAMP from 200 m to 120 m 3D RMS, from 50 m to 30 m for GRACE-FO and from 65 to 53 for Jason-3. EKF with CHAMP also improved from 120 m to 45 m 3D RMS. In contrast, the remaining filer/satellite combinations did not change significantly.

Analyzing the performance of each filter, it can again be seen that the EKF generally performs best. For Grace-FO and CHAMP, EKF shows errors at least twice smaller than the other filters, while for Jason-3 it performs at the same level as the other filters.

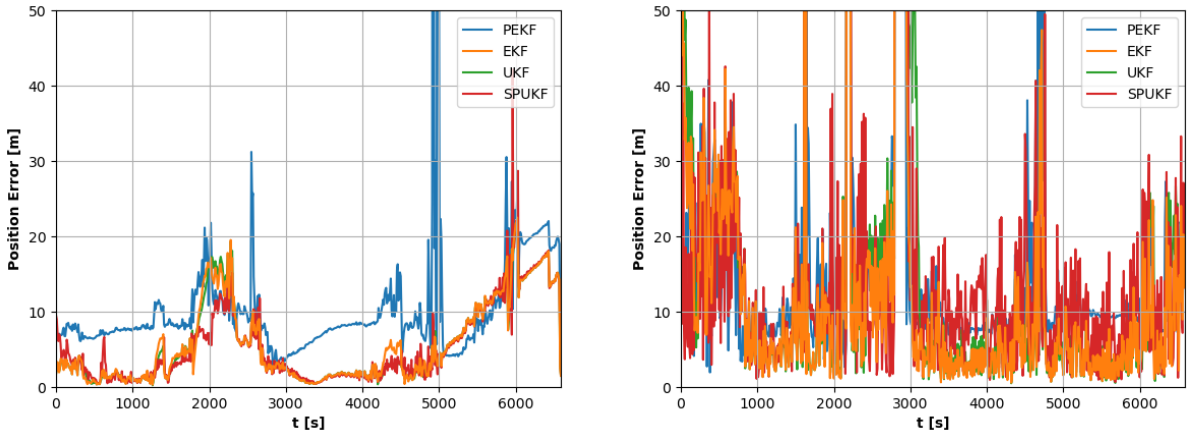

(a) GRACE-FO. **(b)** Jason-3

Figure 4.1: PR-based KF results using theoretical KF settings and elevation-threshold based measurement selection.

The 3D position errors over time for the GRACE-FO and Jason-3 datasets can be seen in Figure 4.2. For Grace-FO, the accuracy excursions appear smaller, especially for SPUKF and UKF, which perform very similarly to the EKF/PEKF. This is potentially because of the much higher weight being put on the 0th sigma point, representing the mean, therefore leading to better quality predictions. Furthermore, more trust is put on the measurements, thus making them the main limitation on overall OD accuracy.

For the Jason-3 filter performance, the discrepancy between filter performance also reduces significantly. All filters appear mostly similar, which again indicates that the measurement accuracy is the main limiting factor, rather than the quality of the predictions.

In general, the tuned filter performance is not significantly better than the filters using theoretical settings. This could simply be due to a too small dataset being used for tuning purposes. With only 2 hours of data used for tuning purposes, the filters might be tuned to work better with lower quality measurements, or vice-versa, the measurements could be higher quality than the average. A potential solution could be to use a larger dataset for tuning purposes, although this does slow down the tuning process. But in general, it can be concluded that the filters can perform relatively well with the theoretical noise matrices.

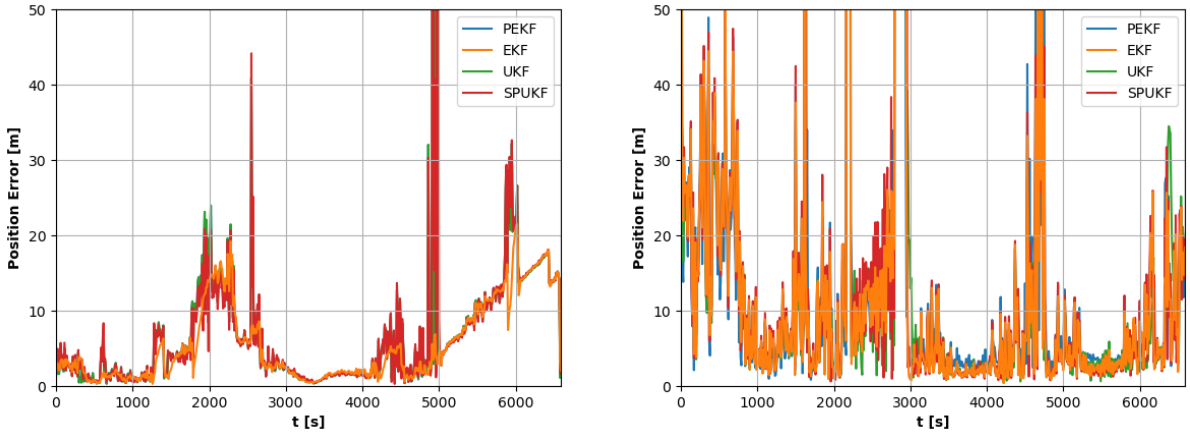

(a) GRACE-FO. **(b)** Jason-3

Figure 4.2: PR-based KF results using tuned KF settings and elevation-threshold based measurement selection.

Table 4.5: PR-based KF OD errors for CHAMP, Grace-FO and Jason-3 L1 GPS measurements, using tuned filter settings, J2 dynamical model and real-time GPS measurement selection. Showing the standard deviation for each state component in the RSW (Radial, along, cross-track) and the 3D RMS *10% of solutions diverged and were excluded from the accuracy calculation.

Filter	Sat.	Position [m]				Velocity [cm/s]			
		R	S	W	3D	R	S	W	3D
PEKF	CHAMP	80.3	51.3	56.8	113.3*	694.6	828.8	526.1	1201.8
NRPC-PEKF	CHAMP	80.3	51.3	56.8	113.3*	694.6	828.8	526.1	1201.8
EKF	CHAMP	36.3	20.2	12.9	45.5	184.2	101	73.9	222.6
SPUKF	CHAMP	90.6	54.9	57.2	122.9	115.6	111.9	45	220.6
UKF	CHAMP	89	54.1	54.8	120.5	677.3	424.5	504.9	944.7
PEKF	GRACE-FO	10.1	24.9	9.6	28.6	99.1	303.3	126.7	350.6
NRPC-PEKF	GRACE-FO	10.1	24.9	9.6	28.6	99.1	303.3	126.7	350.6
EKF	GRACE-FO	5.5	5.7	1.9	8.2	9.1	11.4	6	18.3
SPUKF	GRACE-FO	10.5	26.6	10.3	30.4	100.5	100.6	9.1	199.4
UKF	GRACE-FO	10.1	24.9	9.6	28.6	99.3	303.2	118.2	340
PEKF	Jason-3	33.4	26.7	24	49.5	199.9	188.6	176.6	343.1
NRPC-PEKF	Jason-3	33.4	26.7	24	49.5	199.9	188.6	176.6	343.1
EKF	Jason-3	33.6	28.2	25	51	251.4	286	249.2	454.6
SPUKF	Jason-3	36.3	30.3	27.1	55	295.5	177.2	141.6	374.4
UKF	Jason-3	31.3	28.5	24.9	49.8	186.9	192.3	152.7	308.4

Potential Filter Performance

In this subsection, the implemented filter performance is shown using ideal GPS measurement selection, leading to significantly improved performance. The goal is to highlight the potential short-coming of the current implementations and importance of the GNSS preprocessing blocks, before the KF interface. The only difference in the OD algorithms here from the previous subsction is the GPS measurement selection. All other variables: KF settings, dynamical model and filter, and prediction formulations remain identical.

The measurement selection block must select 4 GPS observations from all the tracked GPS space vehicles. The Kalman Filters are set up to find a solution using 4 observations, whereas the receivers have many more channels and at times have up to 11 measurements available. The selection of these measurements has a direct impact on the quality of the orbit solution. Measurements can be selected based on the SNR of the signal, distribution of the GPS satellites by evaluating the Dilution of Precision (DOP) values or the elevation of each GPS vehicle w.r.t. the receiver.

In the previous OD results, measurements are selected in a simple manner by applying a commonly used real-time 5 degree elevation cut-off threshold. SNR was not considered, as it was not available in the RINEX observations for the Jason-3 data and the Geometric Dilution of Precision (GDOP) was not computed due to the added computational load.

In the results of this subsection, ideal preprocessed measurement selection procedure was used. The observations are selected by testing every possible combination in every time-step. The kinematic solution for each combination of measurements is computed and evaluated w.r.t. the precise orbit data. The combination of tracked SV leading to the smallest orbit error is then saved to be used as the KF inputs at that time-step. This method was repeated for the entire time-series, resulting in a predetermined set of selected observations.

The results for this ideal measurement selection are shown in Table 4.6. The improvement in orbit solution quality is immense, with CHAMP's OD accuracy improving to about 10 m 3D RMS and Jason-3/GRACE-FO showing better accuracy than 5 m 3D RMS.

These results not only provide insight into the important of the GPS observation selection but also in the shortcomings of the novel filters. While the position accuracy of all filters is good and generally similar for each algorithm, the velocity errors stand out for the novel filters. For each satellite, the UKF and EKF have much smaller velocity errors- from 20 cm/s to 100+ cm/s in case of Jason-3 and from EKF/UKF's 20 to PEKF's 80 and SPUKF's 250 cm/s for GRACE-FO. As the subsequent prediction requires good knowledge of the satellite's velocity, this shows that the novel filters perform worse than the typical EKF. This indicates a potential implementation fault in the state transition matrices of the

velocity term partial derivatives, as EKF and UKF relied on these matrices less than the novel filters. However, no such issue was identified.

The representative time-series of the OD errors for GRACE-FO and Jason-3 are shown in Figure 4.3. In case of Grace-FO data, the PEKF, UKF and EKF perform very closely, while the SPUKF is consistently showing larger errors. Also, the accuracy excursions around 2000s and 6000s are also observable, but have a lower magnitude with this measurement selection scheme. For Jason-3, all filters perform very closely, but the EKF visibly outperforms every other option, with the PEKF coming at a close second.

Table 4.6: PR-based KF OD errors for CHAMP, Grace-FO and Jason-3 L1 GPS measurements, using tuned filter settings, J2 dynamical model and post-processed GPS measurement selection. Showing the standard deviation for each state component in the RSW (Radial, along, cross-track) and the 3D RMS ·*10% of solutions diverged.

Filter	Sat.	Position [m]				Velocity [cm/s]			
		R	S	W	3D	R	S	W	3D
PEKF	CHAMP	9.8	3.1	3.8	11.1	431	1040.9	52.2	1128
NRPC-PEKF	CHAMP	9.8	3.1	3.8	11.1	431	1040.9	52.2	1128
EKF	CHAMP	9.9	3.2	4.1	11.3	73.3	26.1	32.3	84.4
UKF	CHAMP	9.4	3	3.8	10.7	88	26.1	39.6	100.1
SPUKF	CHAMP	9.8	3.1	4	11.2	7.8	2.6	4.9	9.6
PEKF	GRACE-FO	1.5	1.3	1.7	2.7	15.1	11.4	47.3	88.6
NRPC-PEKF	GRACE-FO	1.5	1.3	1.7	2.7	15.1	11.4	47.3	88.6
EKF	GRACE-FO	1.2	1.3	1.6	2.4	8.7	8.5	7.8	17.4
UKF	GRACE-FO	1.5	1.3	1.7	2.7	15.9	9.6	11.4	22.8
SPUKF	GRACE-FO	1.7	1.4	1.7	2.9	1.6	7.2	42	78.9
PEKF	Jason-3	0.6	0.5	1.4	2.3	5	10.9	83.3	135.1
NRPC-PEKF	Jason-3	0.6	0.5	1.4	2.3	5	10.9	83.3	135.1
EKF	Jason-3	1.1	0.7	0.6	1.4	15.7	8.5	7.7	19.8
UKF	Jason-3	1.1	0.7	0.6	1.5	10	7.5	6.6	16.2
SPUKF	Jason-3	1.2	0.7	0.6	1.5	12.4	9.1	60.9	99.2

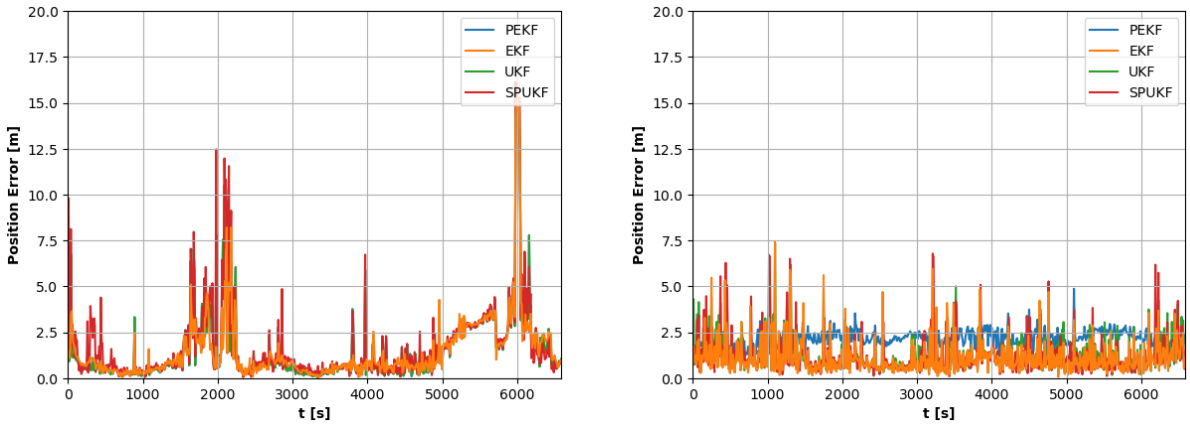

(a) GRACE-FO. **(b)** Jason-3

Figure 4.3: PR-based KF results using tuned KF settings and ideal measurement selection.

4.2.3. Carrier-Phase EKF Expected Performance

In this subsection, the expected performance for a carrier-phase based EKF formulation will be looked into. Due to time constraints, CP-based EKF were not implemented and instead it was decided to refer to literature to quantify the expected OD errors. This enables further evaluating CP-based methods for the combined OD-OP performance.

The CP-based EKF performance Table 4.7 based on past and current literature are shown in Table 4.7. While the results for HY-2A and SWAMR C satellites indicates performance that is better than 0.5 m, these required the use of DF measurements which do not conform with the SF observation constraint. The remaining satellites used the GRAPHIC combination, first introduced by [69], which eliminates the ionospheric range delay. These only require the SF pseudorange and carrier-phase measurements at the L1 frequency and conform with the SF receiver limitation. Therefore, the most conservative results from the flight experience of the PROBA-2 satellite will be used as the expected CP-based OD method accuracy in the subsequent analyses.

Table 4.7: CP-based OD results for satellites with flight experience

Satellite	Meas.	3D RMS [m]	Pred. Step [s]	Receiver	Source
PROBA-2	GRAPHIC	1	30	Phoenix	[40]
X-SAT	GRAPHIC	0.9	30	Phoenix	[14]
FY3C	GRAPHIC	0.7	30	GNSS Occultation Sounder	[15]
HY-2A	DF CP	0.33	-	CAST	[71]
SWARM C	DF CP	0.3	30	PODRIX	[18]

4.2.4. OD application to Satellite Constellations

The GNSS-OD algorithms will be applied in a satellite constellation and thus commercially available, reliable and affordable receivers must be considered. However, their capabilities will differ from the scientific GNSS receivers used on CHAMP, Grace-FO and Jason-3 satellites. Therefore, several COTS receivers will be looked into and their performance will be compared to the scientific receivers in order to determine whether a similar performance can be expected for the entire constellation.

First, the capabilities of COTS receivers must be quantified. This can be seen for 4 receivers in Table 4.8. The indicated 1-sigma position accuracies are roughly similar, with the SF receivers indicating a slightly worse performance than the EKF results seen in Table 4.5. In contrast, the Blackjack receiver on Jason-3 is specified to have 16 tracking channels and to provide the position accurately to 50 meters, while the pseudo-range measurements are accurate to 10 cm and carrier-phase to 1 mm [37]. Although this indicates worse performance of the scientific receiver, in reality the OD accuracy strongly depend on the used algorithms, flight regimes, etc. and cannot be directly compared. The found EKF results for the Jason-3 satellite were in fact less accurate and thus will be kept consistent for the subsequent OP evaluation. The resulting conclusions will remain applicable as long as the COTS receivers do indeed perform as indicated in their data sheets.

Table 4.8: COTS GNSS receivers with flight heritage and some of their technical specifications.

Model	Manufacturer	Freq. Band	Channels	3D Pos. Error [m]	Source
NGPS-01-422	Newspace Systems	L1	12	10	[64]
SM-GNSS-MSP430-SKTRQ	Spacemanic	Not Specified	60	2.5	[59]
G3PSTAR	Elecnor Deimos	L1/E1 L5/E5a	60	4	[11]
ACC-GPS NANO-NR	Accord Software & Systems Private Limited	L1	32	10	[2]

The expected SF GNSS-OD performance for Kinematic, PR-based EKF and CP-based EKF is presented in Table 4.9. The errors components are shown in the RSW reference frame, as these are more intuitive as basic ECI/ECEF coordinates in terms of their values over time. The PR-based EKF and Kinematic Single Point Positioning results were derived using the Jason-3 flight data. For the SPP's velocity errors, the velocity was first computed using a using a second order differentiation of the computed positions. The CP-based position errors were taken from the PROBA-2 flight experience results in [40].

Table 4.9: State Errors for each Orbit Determination algorithm, showing the mean and standard deviation.

OD Algorithm	Kinematic SPP	PR-based EKF	CP-based EKF
Radial Pos. Error [m]	11.0+/-46.0	6.5+/-33.6	0.5+/-0.5
Along-track Pos. Error [m]	-5.9+/-27.0	-4.1+/-28.2	0.3+/-1.2
Cross-track Pos. Error [m]	0.7+/-32.0	-2.2+/-25.0	0.0+/-0.3
Radial Vel. Error [m/s]	0.0040+/-5.80	0.0230+/-2.51	-0.0030+/-0.0009
Along-track Vel. Error [m/s]	0.2000+/-6.90	0.0130+/-2.86	-0.0001+/-0.0006
Cross-track Vel. Error [m/s]	-0.0004+/-12.80	0.0030+/-2.49	0.0001+/-0.0004

4.3. Novel Filters Tested with Flight Data

In this section, the Novel KF performance will be looked into deeper, analyzing how the PEKF and SPUKF perform with more spaced out GPS measurement updates. It will also be looked into what leads to their performance shortcomings. This is first done for the SPUKF in subsection 4.3.1. The PEKF will be analyzed in subsection 4.3.2, including the original PEKF performance and shortcomings, as well as the NRPC-PEKF.

4.3.1. Single-Propagation Unscented Kalman Filter

Result and Discussion

The accuracy of the SPUKF for 2 hours of flight data at increasingly large update intervals is shown in Table 4.10. Points with 3D position errors above 1000 m or velocity errors exceeding 100 m/s were considered to be diverged, as there are expected to be too poor for the required subsequent orbit prediction.

Generally, a worse performance can be seen for longer update intervals. Outside of the CHAMP satellite, the 3D RMS grows for longer update rates- going from 27 to 47.5 m for GRACE-FO and from 52.7 to 72.1 m for Jason-3. Additionally, at update steps of 60, the fraction of diverging solutions increases significantly, with about 35-50% diverging and at update steps of 120 s, no solutions converge. The SPUKF's performance would likely diminish much less if it was re-tuned for each increased update interval. Nonetheless, the results do indicate that the filter's prediction step quality is 1) strongly dependent on the tuning or 2) only good enough for shorter steps. The latter point is backed up by the fact that most of SPUKF's sigma points are propagated using the linearized STM. Therefore, the simplified prediction procedure could be the cause for the filter's poor performance.

Table 4.10: PR-based SPUKF OD errors for multiple satellites' L1 GPS measurements for changing measurement update intervals, using tuned filter settings. Showing standard deviation for each state component in the RSW (Radial, along, cross-track) and the 3D RMS for the converged solutions.

Sat.	Upd. Int. [s]	Div. Sol. [%]	Position [m]				Velocity [m/s]			
			R	S	W	3D	R	S	W	3D
CHAMP	10	0.2	86.9	52.7	54.7	117.9	0.6	0.4	0.4	0.8
CHAMP	20	0.3	68.5	44.1	48.6	96.7	1.1	3.3	0.1	3.7
CHAMP	30	0	79	45.1	35.8	100.3	10	23.3	0.3	27.3
CHAMP	60	47.6	193.8	83.3	110.6	264.5	53.7	172.6	0.6	182.6
CHAMP	120	100								
GRACE-FO	10	0	9.6	23.5	9.1	27	0.1	0.2	0.4	0.8
GRACE-FO	20	0	11.4	30.8	11.9	35	1.1	3.2	0.4	3.9
GRACE-FO	30	0	16.3	40.4	14.2	47.5	9.7	22.7	0.5	26.9
GRACE-FO	60	46.6	287.4	106	102.8	333.9	52.2	169.7	0.5	179.7
GRACE-FO	120	100								
Jason-3	10	0	34.6	29.2	25.8	52.7	2.9	1.6	1.4	3.8
Jason-3	20	0	42.9	36.7	31.8	65.5	3.2	2.7	1.3	5.1
Jason-3	30	0	45.2	41.5	34.4	72.1	8.4	16.9	1.1	21.6
Jason-3	60	37.9	301	149.1	86.5	350.5	56.7	138.2	2	150
Jason-3	120	100								

Observing the time-series of the OD errors of the SPUKF can provide some additional insight into the filter's performance with longer update intervals. This is shown for the Jason-3 and CHAMP satellites in Figure 4.4. The OD performance visually decreases over the entire time-series. Even during periods of the SPUKF performing well (eg. around 2500s for CHAMP, 4000s for Jason-3), the 60-s update OD errors are mostly above the 10/20/30 s lines. That statement further applies to the 30-s update errors compared to 10/20-s results and 20-s to 10-s. Another observation is that that excursions from the nominal 30-50 m OD accuracy occur for both short (10-20 s) and long (60 s) update intervals. However, these are less detrimental to the high-frequency update rate results, as fewer poor updates are made in the low-quality observation clusters, leading to a smaller impact on the 3D RMS error.

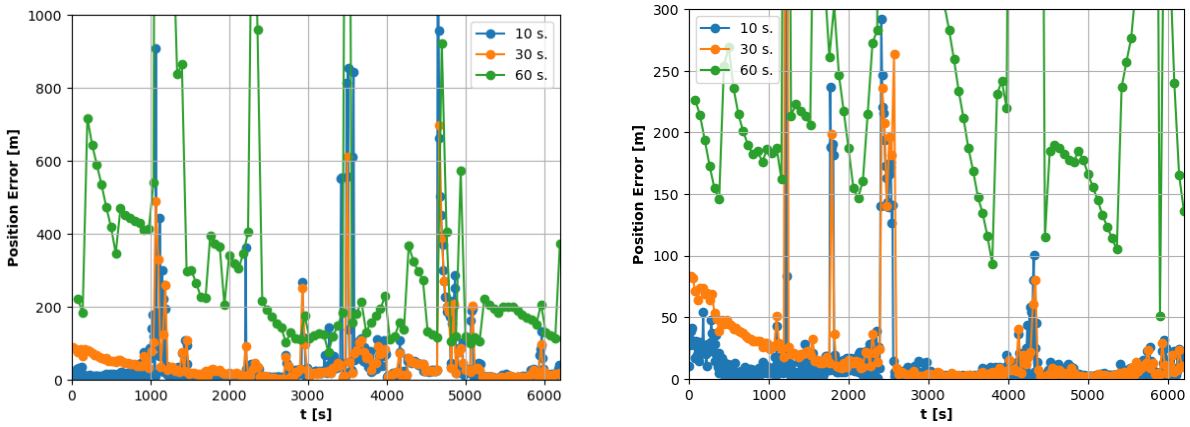

(a) CHAMP. **(b)** Jason-3

Figure 4.4: PR-based SPUKF for different measurement update rates, showing results using tuned settings, elevation-threshold based measurement selection.

Analysis of Prediction Step

In this subsection, the prediction step quality of the SPUKF will be looked into. This is the suspected reason for SPUKF's poor performance compared to the other analyzed filters. As an Unscented filter, the SPUKF uses a weighted mean of multiple sigma points to predict the state, but to save on computational load, it fully propagates only the 0th sigma point, representing the mean state. The simplified updates of the remaining sigma points could lead to a lower quality of the complete prediction step. Therefore, it will be analyzed how large the prediction error are for each sigma point, with a closer look at the 0th sigma point and the weighted mean. The prediction step errors of the SPUKF will be compared to the UKF.

The prediction errors of each sigma for the SPUKF using CHAMP and Jason-3 data can be seen in Figure 4.5. A sharp contrast can be seen in the prediction error for the labelled groups of sigma points. Points 1-7 and 8-16 mostly show prediction errors above around 1000 m for both satellites. The 0th point remains at much smaller prediction errors. This makes sense, as the other points are artificially offset prior to the prediction to better capture the true mean and does not indicate an issue with the predictions. However, what can be seen is that the weighted sum is generally at the same level of error as the 0th sigma point. This indicates that the prediction quality does not improve on a single-step basis by using multiple sigma points and just a single point would likely suffice. The same can be seen for the UKF predictions in Figure 4.6 - where the weighted sum of the predictions does not lead to a smaller error than the 0th sigma point.

After observing the prediction step quality- very limited conclusions can be drawn regarding the lack of unscented filters' performance improvement. It could be seen that the predictions generally perform well, although on a single-step basis, no improvement can be spotted by the use of multiple sigma points. However, this does not show whether the behaviour over the entire time-series improves, as the filters do carry information over from the previous update steps. Thus, it can only be concluded that the Unscented filters' performance issues are not due to the prediction step being poor, but are likely limited by the correction or another unforeseen factor.

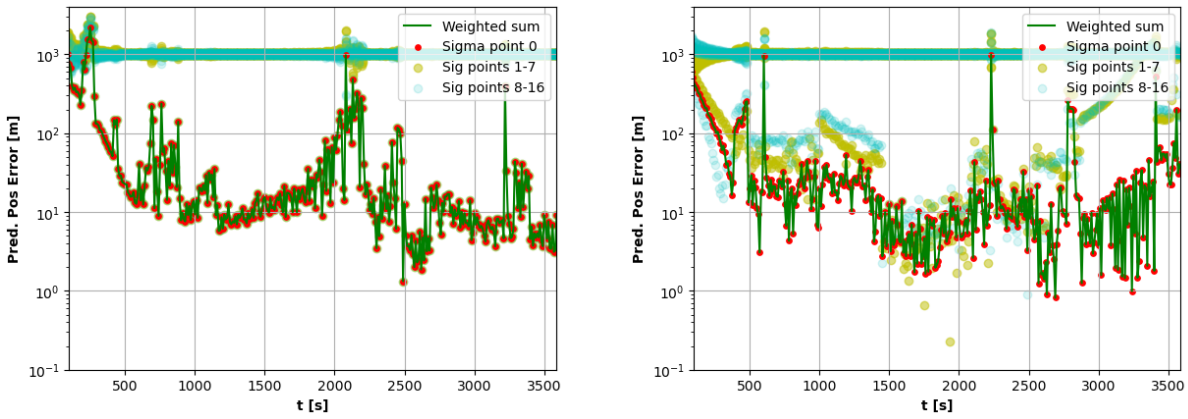

(a) CHAMP. **(b)** Jason-3

Figure 4.5: Prediction step errors for the SPUKF, showing the error of each sigma point, as well as their weighted sum, representing the predicted state value.

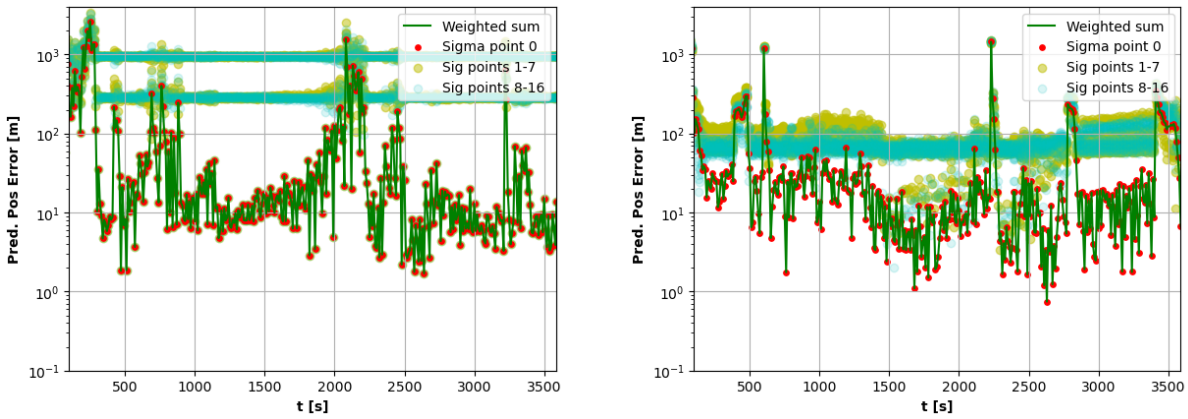

(a) CHAMP. **(b)** Jason-3

Figure 4.6: Prediction step errors for the classic UKF, showing the error of each sigma point, as well as their weighted sum, representing the predicted state value.

4.3.2. Preprocessing Extended Kalman Filter

Results and Discussion

The OD accuracy of the PEKF for 2 hours of flight data with increasingly longer update intervals are shown in Table 4.11. Again, solutions with 3D position errors above 1000 m or velocity errors exceeding 100 m/s were considered to be diverged, as they are expected to be too poor for the required subsequent orbit prediction.

First, observing the results for CHAMP, a increasingly more solutions diverge for longer update intervals, which is to be expected. However, the 3D position RMS error appears to decrease, which is the opposite is expectations. This could be due to the PEKF's dependence on good coarse position inputs and the longer update intervals might lead to fewer bad coarse position inputs. Also, due to a higher fraction of solutions diverging and being filtered out, this could artificially increase the OD accuracy. When looking at the time-series of the OD errors for CHAMP in Figure 4.7, the accuracy improvement indeed appears to be an artifact. The OD errors peak at 1000 s, for the sparser case of 120 s, fewer sets of lower quality measurements are captured, leading to the filter diverging less than the 10 or 30 s cases. However, observing the velocity errors, they are higher for 60/120s update intervals compared to 10s intervals by a factor of 2, which does indicate that the OD performance generally worsens.

Table 4.11: PR-based PEKF OD errors for multiple satellites' L1 GPS measurements for changing measurement update intervals, using tuned filter settings. Showing standard deviation for each state component in the RSW (Radial, along, cross-track) and the 3D RMS for the converged solutions.

Satellite	Upd. Int. [s]	Div. Sol. [%]	Position [m]				Velocity [m/s]			
			R	S	W	3D	R	S	W	3D
CHAMP	10	7.4	76	48.6	53.8	107.3	6.6	7.8	5	11.4
CHAMP	20	7.7	64.2	42.5	47.6	92	3.5	5.6	3.2	7.4
CHAMP	30	8.2	74	40.5	39.8	95.6	3.3	1.9	1.9	4.2
CHAMP	60	8.7	48.6	37.1	43.3	76.9	8.8	19.6	1.4	21.5
CHAMP	120	9.6	33.2	24.2	16.4	48.6	8.5	15.8	0.8	18
GRACE-FO	10	0	9.6	23.7	9.1	27.2	0.9	2.9	1.1	3.2
GRACE-FO	20	0	11.9	32.8	12.6	37.2	0.7	2.2	0.9	2.5
GRACE-FO	30	0	13.9	40.1	15.4	45.3	0.6	1.8	0.7	2
GRACE-FO	60	0	18.4	56.3	21.6	63.3	0.4	1.1	0.4	1.3
GRACE-FO	120	0	13.8	30.9	12.4	36	0.5	0.6	0.1	1.1
Jason-3	10	0	31.9	25.9	22.7	47.7	1.9	1.8	1.5	3
Jason-3	20	0	37.5	33.6	28.2	58.5	1.7	1.8	1.4	2.9
Jason-3	30	0	43.4	40.1	32.9	68.2	1.7	1.6	1.3	2.7
Jason-3	60	0	55.7	55	44.3	90.6	1.2	1.3	1	2
Jason-3	120	0	15.3	9.1	7.3	19.8	0.3	0.3	0.2	0.6

Observing results for the other 2 satellites, the results also generally get worse for longer update intervals. The 3D RMS errors grows for intervals from 10s to 60s, with position errors increasing by about a factor of 2, while velocity errors remain similar. Unlike CHAMP, none of the solutions diverge. As to the 120 s update interval leading to better OD accuracy, a similar case as for the CHAMP satellite can be seen in the right of Figure 4.7. Fewer poor coarse solutions are captured as inputs for the PEKF, thus leading to fewer error peaks.

Therefore, the PEKF does perform slightly worse for longer update intervals, but still provides reasonably accurate solutions. This was according to expectations, as the PEKF's correction step performance mostly depends on the quality of the kinematic OD solution. Although the kinematic NRM and NRPC do use the previous solution as an initial guess for the next point, the sensitivity is insignificant compared to a typical KF dependency on the previous solution.

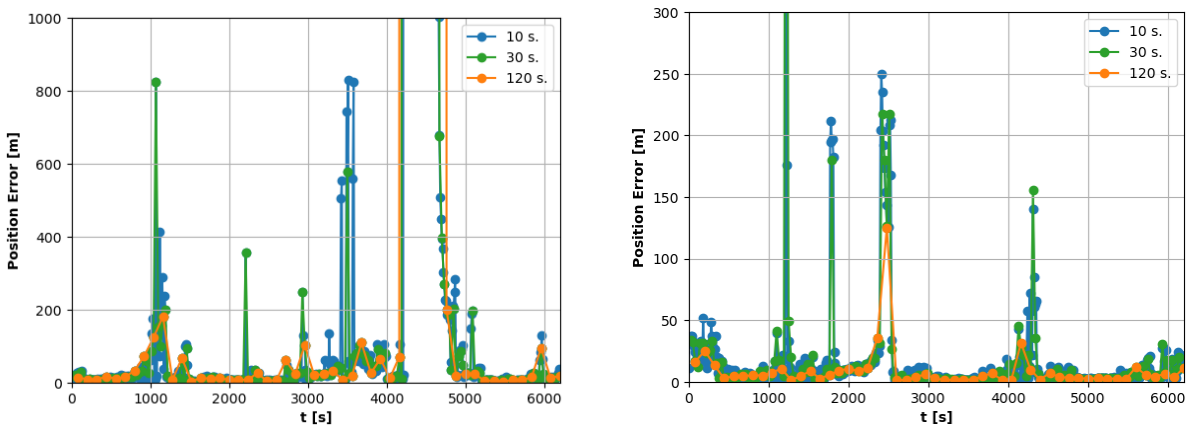

(a) CHAMP. **(b)** Jason-3

Figure 4.7: PR-based PEKF for different measurement update rates, showing results using tuned settings, elevation-threshold based measurement selection.

Analysis of Coarse Solution Filtering

In this subsection, the performance issues of the PEKF will be looked into. Comparing the general structure of the EKF and PEKF- their prediction steps are identical, while the correction step is the

same in terms of the interface with measurements, but the latter do differ. While the EKF handles the pseudoranges directly and directly models the predicted states as the pseudoranges, the PEKF already receives the coarse position solutions- thus not directly seeing the pseudoranges and their errors. Therefore, the EKF directly handles the errors in the pseudorange, while for the PEKF the measurement errors are transformed to coarse position errors. As the Numerical methods are less predictable in their solution qualities, the resulting coarse position solution errors might be harder for the PEKF to filter out. Therefore, it will be analyzed whether the PEKF indeed struggles to filter out the coarse solution errors which occur when using the analyzed GNSS flight data. This will be done by comparing the performance of the PEKF when using NRM outputs and using simulated coarse position solutions with artificially added Gaussian Errors.

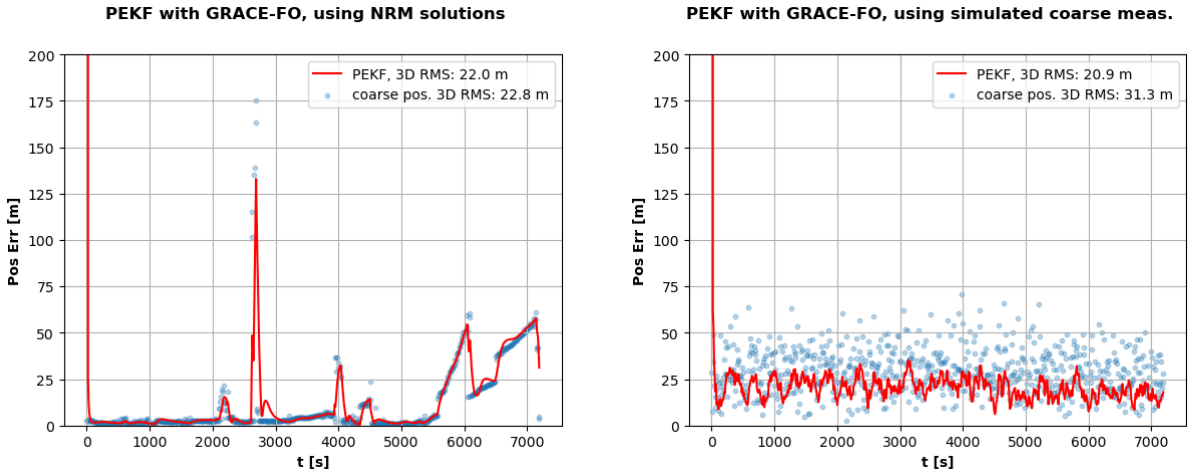

(a) PEKF processing NRM coarse solutions.

(b) PEKF processing simulated, noisy coarse solutions.

Figure 4.8: PR-based PEKF performance using NRM-derived coarse position solutions (left) and simulated coarse position solutiosn (right).

The PEKF's performance is shown on the left of Figure 4.8 when using actual NRM coarse solutions. It can be seen that the filter generally performs well and filters out low quality NRM solutions, which can be observed in the bump around 2200 s. But its performance still rapidly degrades when a series of poor coarse solutions occur, as seen just after 2500 s or after 5500 s. It makes sense that the PEKF fails to cope with this errors behavior, as the errors seem to grow and decrease in clusters, while remaining very low (<5 m) for long periods of time. These error excursions offset the PEKF enough that it takes multiple good solutions until the PEKF returns to the converged behaviour. While the PEKF solutions are slightly better than the coarse positions (from 22.8 m 3D RMS down to 22 m), the improvement is rather minimal and is strongly affected by the position error excursions. Thus, the PEKF can only lead to minimal improvements over the inconsistent NRM solutions.

A different behaviour can be seen on the right of Figure 4.8, where the PEKF receives simulated coarse position measurements. The simulated coarse position errors offset with non-zero mean Gaussian noise and are on average higher than the previous NRM solutions (31.1 m compared to 22.8 m), but the PEKF performance is in fact better with the simulated measurements (20.9 m compared to 22 m 3D RMS). It can also visibly be seen that the erroneous coarse positions are consistently improved, while in the case of the NRM solutions, they are much closer in quality. Therefore, the poor PEKF performance can be partially explained by the inconsistent NRM solution quality and the problematic error behaviour.

NRPC-PEKF Performance Analysis

The Novel NRPC-PEKF performance was quantified previously and it did not lead to improvement. In terms of accuracy, NRPC and the original NRM PEKF performed identically. This was consistent for all sets of flight data used.

To analyze why the NRPC-PEKF did not improve in performance compared to the original PEKF- the changed preprocessing block must be looked into. Since the filters are identical in their prediction

and correction steps, the Newton-Raphson Predictor-Corrector method must be focused on. This will be done by comparing the coarse position solutions from the NRM to the NRPC.

Table 4.12: Iterations used to converge to numerical solutions by the NRM and NRPC when 1) using previous solutions as initial guesses and 2) using constant initial guesses.

Sat.	Num. method	Mean iter. used[-]	Convergence probability at mean iter. [%]	Max iter. used [-]
Using previous solution as initial guess				
CHAMP	NRM	3	99.6	5
CHAMP	NRPC	3	99.6	5
GRACE-FO	NRM	3	99.9	5
GRACE-FO	NRPC	3	99.9	5
Jason-3	NRM	3	99.9	5
Jason-3	NRPC	3	99.9	5
Using [0,0,0,0] as initial guess				
CHAMP	NRM	5	98.3	7
CHAMP	NRPC	5	97.9	9
GRACE-FO	NRM	5	100	5
GRACE-FO	NRPC	5	99.9	6
Jason-3	NRM	5	96.2	5
Jason-3	NRPC	5	97.8	5

Both NRM and NRPC were used to process the coarse orbit solutions for all sets of flight data. The iterations used by both methods are shown in Table 4.12. In the upper half of the table, the root-solvers were updating the initial guesses used as each subsequent point, equal to the previous point's coarse solution. In the lower half, a constant initial guess value of [0,0,0,0] was used, which represents coordinates of the origin of the ECI frame and a 0 m receiver clock error. This represents the case when the numerical methods are being initialized. The methods were considered to converge when the update step size was below 0.1 m, which is an order of magnitude below the best-case accuracy of the root-solvers.

When the initial guesses are updated and effectively closer to the sought solution, NRM and NRPC consistently use the same number of iterations for the same flight data. They both converge within 3 iterations for >99.5% of the cases in rare cases need up to 5 iterations. As NRPC has several extra multiplications performed in each prediction/correction step, this indicates that a simple NRM is a slightly better option for kinematic GNSS-OD solution when running continuously.

Observing the bottom half of Table 4.12, when the numerical methods are using constant initial guesses far away from the solution, discrepancy in their required iterations can be seen. A mean of 5 iterations is needed consistently for both methods, but NRPC is consistently more likely to require additional iterations than the NRM for all sets of flight data. Using CHAMP data - NRPC needed up to 9 iterations and used more than 7 in 2.1% of the datapoints, compared to NRM's 1.7%. With GRACE-FO data, the discrepancy is smaller and it only needed a 6th iteration in 0.1% of the datapoints. With Jason-3 data, the maximum iterations were equal to the mean of 5, with some points converging within 4. For the NRM, this occurred in 3.8% of cases and only 2.2% for NRPC, which again shows that NRM needed marginally fewer iterations than NRPC on rare occasions. This shows that during initialization of the root-solvers, NRM is around 1-2% more likely to converge sooner than the NRPC, which again shows that it is a slightly better option for kinematic GNSS-OD solutions than NRPC.

The solution error per iteration is shown in Table 4.13. The algorithms updates are identical for most iterations. Except on iteration 4, the NRM already converges, while the NRPC still performs another negligibly sized update for its 5th iteration. This does not work as intended, as the convergence condition should be satisfied sooner, which points to a potential implementation fault. Regardless, of this, it can again be seen that the NRPC does not perform any visibly better updates, even without the added iterations. Therefore, it is concluded that the NRPC/NRPC-PEKF do not pose any advantages over the original NRM/NRM-PEKF in GNSS-based OD applications.

Table 4.13: Numerical methods solution error at each iteration for a single datapoint of Jason-3 data with used iteration discrepancy. Final solution marked in bold.

Iteration Nr.	3D Error NRM [m]	3D Error NRPC [m]
0	7718009.921	7718009.921
1	718974.0539	718974.0539
2	1015.207201	1015.207201
3	56.86203809	56.61984324
4	**56.85384639**	56.85384499
5	**56.85384639**	**56.85384665**

4.4. GNSS-based OD Conclusions

In this section, the conclusions relating to the originally formulated RQ2 will be summarized. This is done to each sub-question below.

2 a) *What errors are the expected RSW position and velocity errors for on-board kinematic and reduced-dynamic SF pseudorange based GNSS-OD methods?*

The OD method errors varied between when using different satellites' input data, the ones chosen as most fitting for the subsequent use case for Jason-3, due to its similar altitude and inclination which matches the LEO Inclined satellites. The errors for both methods were listed in Table 4.9 and were in the 10-50 m range for position and 5-10 m/s for velocity.

2 b) *What errors are the expected RSW position and velocity errors for on-board reduced-dynamic SF carrier-phase based GNSS-OD methods?*

Although the CP-based method was not implemented, these have been evaluated in the past. The flight experience of the PROBA-2 satellite using the GRAPHIC combination indicated much lower errors, up to 2 orders of magnitude below the determined with m-dm level errors in position the mm-level errors in velocity. The results were also listed in Table 4.9.

2 c) *How do novel pseudorange-based NRM-PEKF and SPUKF perform with flight data compared to typical EKF and UKF formulations in terms of OD accuracy?*

In general, neither of the novel filters consistently lead to improved precision over the EKF or UKF. With tuned settings and GRACE-FO data, the EKF indicated about 8 m 3D RMS and the UKF - 29 m errors. The PEKF showed 29 m errors and the SPUKF - 30.4 m errors. Although the novel filters showed worse accuracy than indicated by the authors using simulated measurements, the issue could have been due to poor GPS-observation filtering techniques, as a preprocessing *ideal* measurement selection lead to each filter showing about a 3 m 3D RMS. Other reasons for the novel filters' poor performance could have been improper filter tuning.

2 d) *How do novel pseudorange-based NRM-PEKF and SPUKF perform with increasingly sparse measurement updates rates in terms of OD accuracy?*

The SPUKF was found to be very sensitive to measurement updated, whereas the PEKF was affected less. SPUKF showed decreasing precision, going from 9 to 15 m 3D RMS when measurement updated were changed from 10 to 30 s updates and diverged at 120 s update intervals. This indicates that the novel filter's simplified sigma-point propagation prediction quality is poor or an implementation fault in the prediction step. In contrast, the PEKF was a lot more consistent. Going from 10 to 120 s updates, the filter still converged with about 9 and 20 m 3D RMS. This was because the PEKF was more dependent on the preprocessing block performance, which does not strongly depend on previous solution quality.

2 e) *Does the performance of the NRM-PEKF algorithm, documented by [3] improve when using a higher efficiency NRPC root finding method in terms of OD accuracy or CL?*

Implementing and testing the NRPC-PEKF, no improvement was observed over the original NRM-PEKF. In terms of precision, both methods were identical to cm-level. This was because the preprocessing blocks also provided the same quality of solutions and the EKF portions of both filters did not differ. When observing the CL, the NRM slightly outperformed the NRPC when running with no initial position knowledge. Furthermore, the NRPC had more steps and computations in each iteration compared to the NRM and thus it could be concluded that the new NRPC-PEKF did not have any advantages over the original NRM-PEKF in GNSS-based OD applications.

5

Orbit Determination and Prediction Performance in LISL

Having chosen the relevant link cases and quantified expected OD algorithm performance, these intermediate results can finally come together to quantify GNSS-OD-OP performance in satellite laser communication. Thus, in this chapter, the Orbit Prediction block will be interfaced with the orbit determination algorithms and their performance will be evaluated in each chosen link case. First, the method to evaluate the OD-OP algorithm performance will be described in section 5.1, including verification efforts. Subsequently, the results of the method will be presented and discussed in section 5.2. The chapter conclusions will be summarized in section 5.3

5.1. Analyzed Method

In this subsection, the method used to compute the OD-OP performance will be described in subsection 5.1.1. Subsequently, the combined OD-OP will be documented in subsection 5.1.2. In subsection 5.1.3, the issue of unavailable validation data for this analysis will be addressed by demonstrating a wide-scale partial system test utilizing the HY2A precise orbit data.

5.1.1. Method Description

The architecture of the OD-OP algorithm evaluation is presented in Figure 5.1. Using the conclusions from the previous analysis of the LISL variables, the chosen host/target initial conditions in each link cases will be used for the true and predicted orbit simulations. The true orbits will be simulated using a full DM and no Initial Condition (IC) offsets. In contrast, the Predicted positions will use simplified DM and IC errors sampled from the OD error statistical distributions, which were determined in chapter 4.

The true orbits are then converted to the true LOS, whereas the predicted orbits to predicted LOS. The angle between the true and predicted LOS will then represent the resulting PE contribution.

Several communication window lengths will be considered to evaluate the PE. First, the Pointing Acquisition window must be considered, which is the initial 100 seconds. This is the total time limit for the signal to be Acquired and tracking to begin. It is therefore the minimum communication window length where the PE must not exceed the maximum threshold. The remaining communication windows to consider are 10, 30 and 60 minute windows. These windows were determined in chapter 3 and were found to cover the major fractions of LISL link case types.

Multiple orbit prediction start-points will need to be considered for the OD-OP algorithm performance in the cross-plane link cases. That is because the PE not only depends on host/target position errors, but also the the link dynamics and geometry, which for any of the more challenging link cases are not constant. Therefore, for the link acquisition prediction window of 100 s, the prediction start times will be shifted through every minute of the entire link window. This way, it can be evaluated during which portions of the available link windows, the OD-OP algorithms provide sufficiently precise LOS predictions.

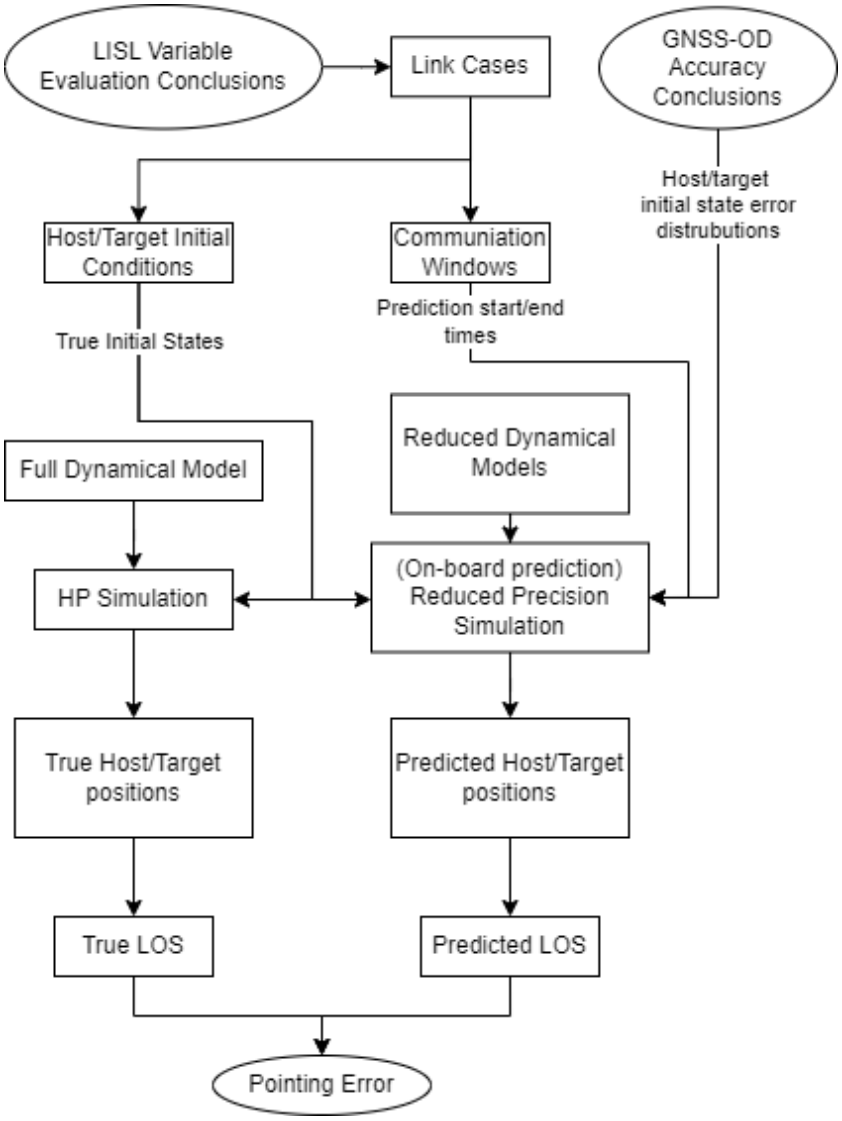

Figure 5.1: Architecture for evaluating the Pointing Errors of combined Orbit Determination and Prediction Algorithms.

5.1.2. Considered OD-OP Algorithms

3 distinct OD-OP algorithm architectures will be considered, varying in complexity, precision and computational load. The interfaced OP algorithm will be tailored to use a similar complexity of prediction method as the OD algorithm, such that no additional algorithm complexity is required for the subsequent predictions.

The integrated OD-OP algorithms are described in Table 5.1. The first is the fully Kinematic Algorithm (KA)- neither the SPP OD method, nor the extrapolation requires any dynamical knowledge. The second is a Basic Dynamic Algorithm (BDA): PR-based EKF, interfaced with an orbit propagator using a J2 dynamical model, the same as in the prediction step of the EKF. The final algorithm is the Complex Dynamic Algorithm (CDA). It assumes Initial state errors equivalent to that of a SF-CP based EKF and uses a complex DM for the predictions. The DM requires SH Earth gravity terms up to D/O 64/64 and perturbations such as luni-solar gravity, SRP and Aerodynamic drag. Both of the dynamic algorithms utilize a fixed-step 4th order Runge-Kutta (RK), which is widely used in GNSS-OD methods and was also utilized in the EKF prediction steps.

Table 5.1: Overview of the analyzed OD and OP algorithms.

OD-OP Algorithm	Kinematic (KA)	Basic Dyn. (BDA)	Complex Dyn. (CDA)
OD IC Errors	KOD SPP	PR-based EKF	CP-based EKF
OP Method	Quadratic Extrapolation	J2 orbit prop.	Full DM orbit prop.
GNSS-OD obs. used	SF L1 PR	SF L1 PR	SF L1 PR and CP
OD State Parameters	r, cdtr	r, v, cdtr	r, v, cdtr, CD, CR, A, emp. accel.
Prediction Model			
Earth Gravity	-	PMG + J2	GOCO05c, D/O 64/64
Perturbing Gavitation	-	-	Luni-solar PMG
Solar Radiation Pressure	-	-	Cannonball SRP model
Drag	-	-	NRLMSISE-00
Numerical Integrator	-	RK4	RK4
Integration time-step	-	5	30
Rotation Model	-	-	IAU2006A

5.1.3. Method Verification

Partial System Test Description

This analysis combines numerous blocks and interfaces varying complexity orbital simulations to get the expected Pointing Errors. Thus, in order to have any confidence in the conclusions, Verification and Validation activities are absolutely essential. However, no validation data is available for LISL and thus the largest scope tests that are available are partial-system verification tests.

The integrated OD-OP algorithm will be tested at the partial system level by utilizing the precise orbits of the Ocean Observation Satellite HY2A. The satellite's data was chosen as its precise to the cm-level and its orbital parameters are closely representative of the LEO Polar satellites in the LEO/MEO constellation considered in this report.

The partial system test will utilize orbit prediction errors calculated using precise orbits and the OD-OP algorithms, as shown in Figure 5.2. The HY2A precise orbits will be used to compute host orbit prediction errors using the combined OD-OP algorithm by removing the HP simulated orbit component from Figure 5.1. On one side, the precise orbit will be used as initial conditions for the OD-OP algorithm-they will be offset with OD errors and subsequently predicted using the OP methods, with the resulting position error being computed between the precise orbit and the predicted orbit. On the other side, the position error will be taken from the HP simulated LISL orbits, where the host's position error is taken between the HP simulated orbit and the predicted orbit using the same OD-OP algorithms. These are computed at the True/Predicted LOS stage of Figure 5.1.

The verification test will be considered passed if the orbit prediction errors using the simulated orbits and HY2A tracked orbits increase at a roughly similar rate. At this level of analysis, the aim is to evaluate the PE component due to imperfect coarse pointing knowledge, which is only one of the components of the entire PE budget. Thus, the margin of the PE is still rather broad and only considered in the 100 urad level. Therefore the orbit prediction method will be verified if 1) the position errors differ within a factor of 2 and the absolute are a above a 100+m-level or 2) if the absolute values OP errors differ below the 100 m-level.

Partial System Test Results

The results of the partial system test applied to each case of initial OD errors and varying complexity orbit prediction methods are shown below.

Kinematic method

The orbit prediction error differences for the Kinematic IC errors and extrapolation-based predictions are shown in Figure 5.3. It can be seen that in both cases of HP and HY2A orbits, the OP error grows rapidly and both reach value above 1e7 m. The absolute differences are above also above 1e5 m, but grow in a similar fashion. The relative difference peaks at above 50% while the OP errors are still small (<1e4 meters) but as the OP errors grow, the relative difference decreases and nears 0%. Therefore, the verification test for this OD-OP algorithm case is passed.

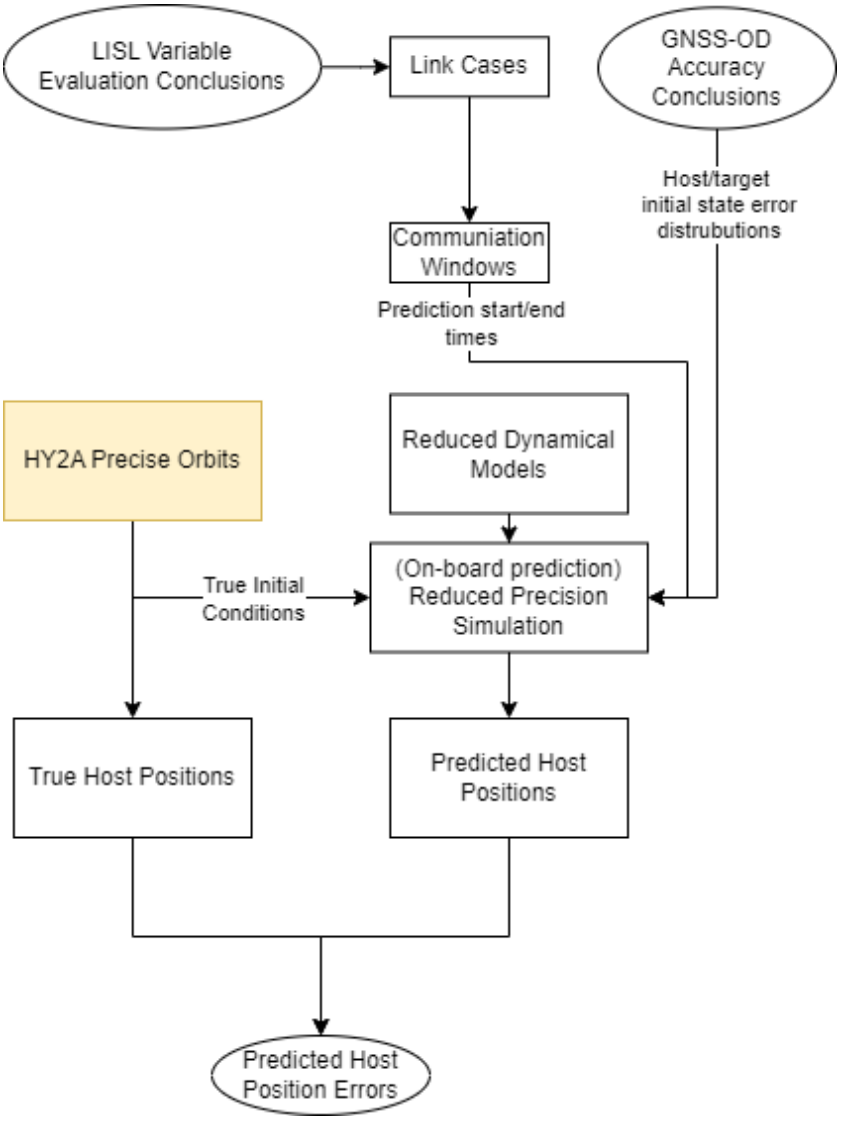

Figure 5.2: Use of precise orbits of the HY2A satellite in verifying the OD-OP algorithm performance.

Basic Dynamic method

The orbit prediction error differences for the PR-based EKF IC errors and Basic Dynamic propagation errors are shown in Figure 5.4. It can be seen that in both cases of HP and HY2A orbits, the OP error grows much slower than the extrapolation methods and only reach about 1e4 m after 1 hour of predictions. The absolute differences only reach about 100 m and grow in a similar fashion. The relative difference remains below 5% throughout the entire prediction window. Therefore, the verification test for this OD-OP algorithm case is also passed.

Complex Dynamic method

The orbit prediction error differences for the CP-based EKF IC errors and Complex Dynamic propagation errors can be seen in Figure 5.5. It can be seen that in both cases of HP and HY2A orbits, the OP errors are much smaller than the other methods and only reach about 10 m after 1 hour of predictions. The absolute differences are also only about 10 m. In comparison, the relative differences are higher, reaching about 50%, but still remain within the required threshold. Therefore, the verification test for the final OD-OP algorithm case is passed.

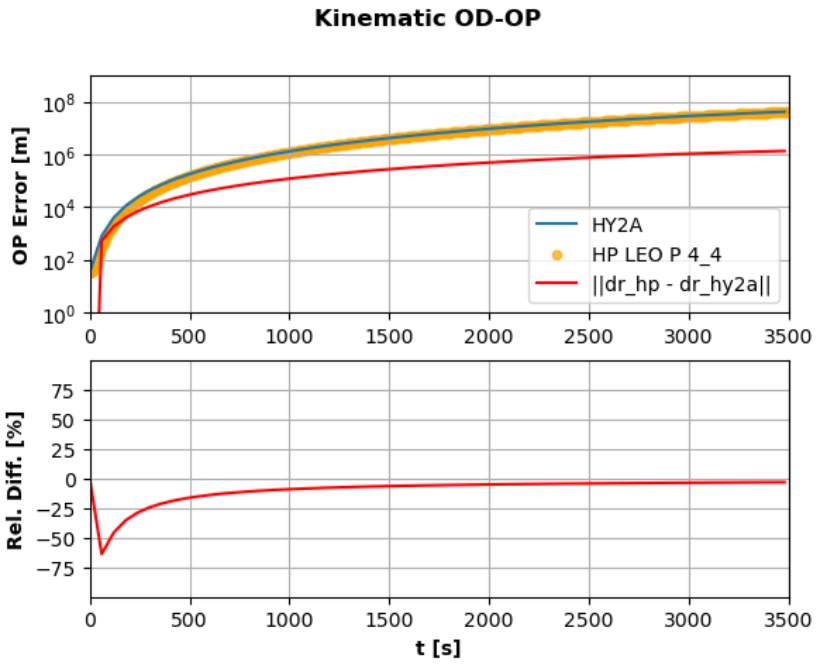

Figure 5.3: Difference in Orbit Prediction Errors for the Kinematic OD initial errors and orbit extrapolation algorithm when using Precise HY2A and simulated High Precision LEO Polar satellite orbits

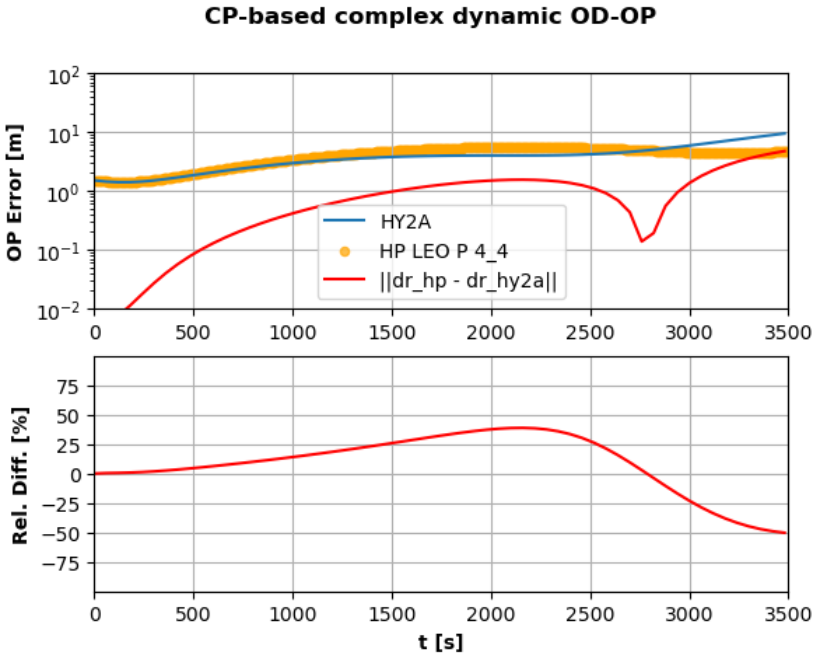

Figure 5.5: Difference in Orbit Prediction Errors for the Complex Dynamic OD-OP initial errors and propagation algorithm using Precise HY2A and simulated High Precision LEO Polar satellite orbits

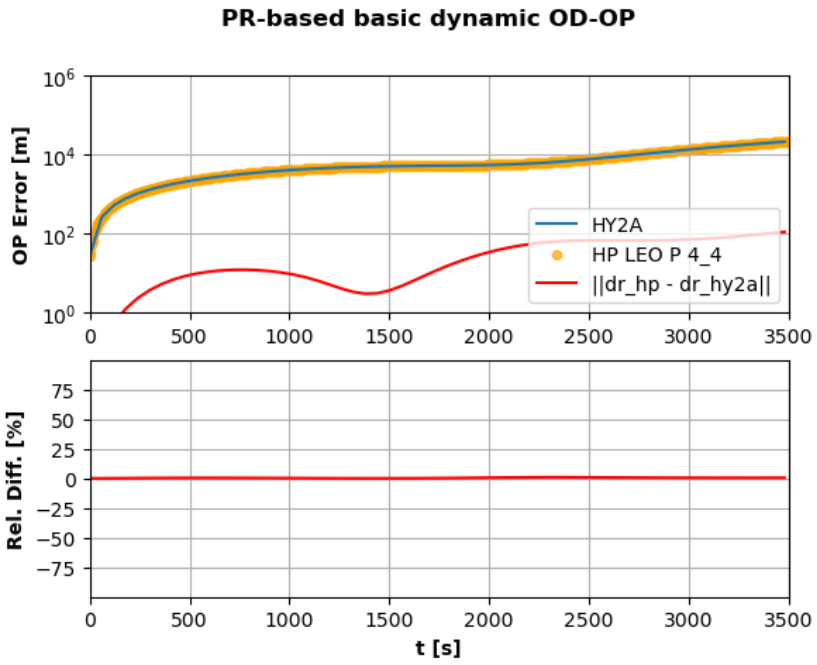

Figure 5.4: Difference in Orbit Prediction Errors for the Basic Dynamic OD initial errors and basic propagation algorithm using Precise HY2A and simulated High Precision LEO Polar satellite orbits

5.2. Results and Discussion

The results will be first separately discussed for the short-term 100 second acquisition window predictions. This is done in subsection 5.2.1. Subsequently, in subsection 5.2.2, the results are presented for the 10, 30 and 60 minute prediction windows.

5.2.1. Acquisition Time Prediction Windows

In this subsection, the pointing errors for the acquisition-time prediction windows will be shown. The results are shown for the mean pointing error with the acquisition predictions starting throughout the entire link window with 30s time-steps. This means that the PE are evaluated after 100 s of predictions if the acquisition window predictions start at 0, 30, 60, etc. second of the link availability window. This allows to see how the PE differ, depending on the start-time and shows how the link-distance affects the quality of orbit predictions.

The results for links including MEO satellites are shown in Figure 5.6. It can be seen that consistently, the Complex-dynamic OD-OP performs the best with acquisition window PE consistently below 1 urad. The Kinematic and Complex dynamic algorithms perform significantly worse, both indicating PE contributions around 10-100 urad. These errors are still an order of magnitude below the mrad-level and thus both algorithms' predictions would be sufficiently accurate for signal acquisition purposes.

The results for links including LEO satellites are shown in Figure 5.7. Again, the Complex-dynamic OD-OP performs the best across the board. Although compared to the links with MEO satellites, the PE contributions now reach up to 10 urad, as seen in the Inter-shell LEO P-LEO I link case. Again, the Kinematic and Complex dynamic algorithms perform significantly worse, both indicating PE contributions between 10 and up to 10000 urad, depending on the link distance when the acquisition predictions start. This shows that there are indeed link conditions where only the most precise OD-OP algorithms provide accurate enough CPA knowledge. That is true when the link distance falls below 1500 km in the LEO P - LEO I or LEO I - LEO I link cases. This is to be expected, as the PE is more sensitive to host/target predicted position errors as link distances shorten. Another conclusion to draw is that the kinematic and basic-dynamic OD-OP algorithms do provide sufficiently accurate coarse pointing knowledge while the link distances are generally larger- above 2500 km. The PE contributions at these distances are below 0.5 mrad which could still be sufficiently small for the PE budget in link acquisition.

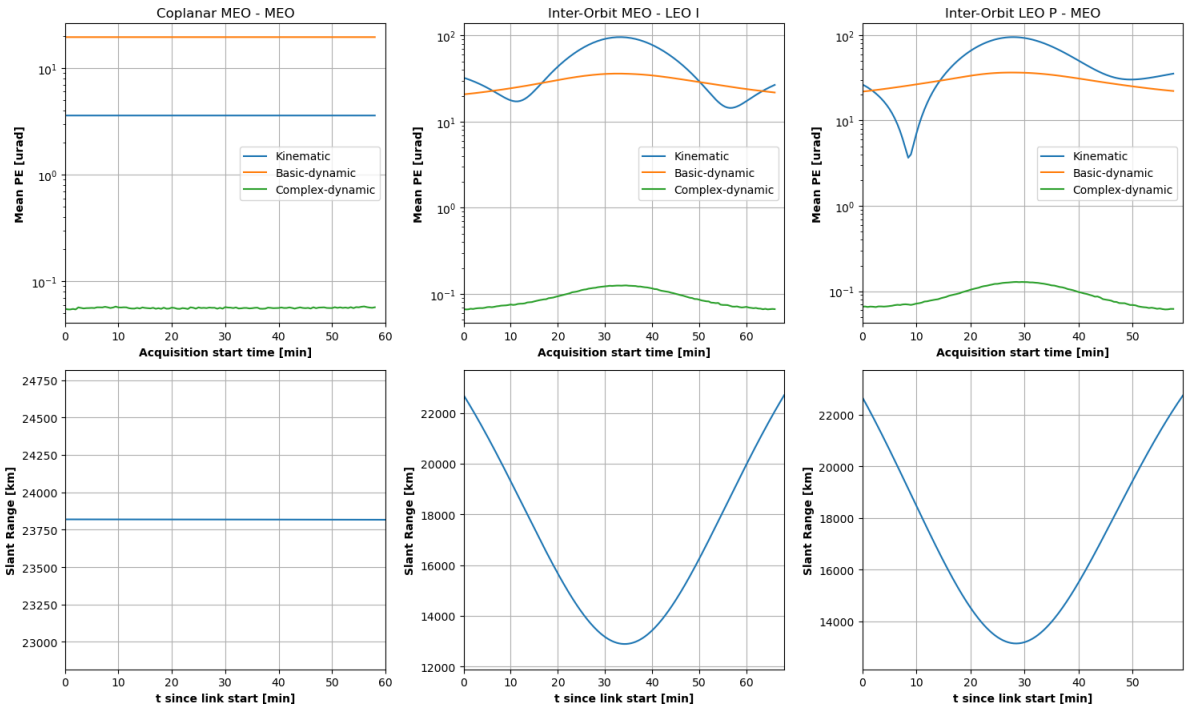

Figure 5.6: Mean PE for each OD-OP algorithm, evaluated at different prediction start times throughout the link availability window.

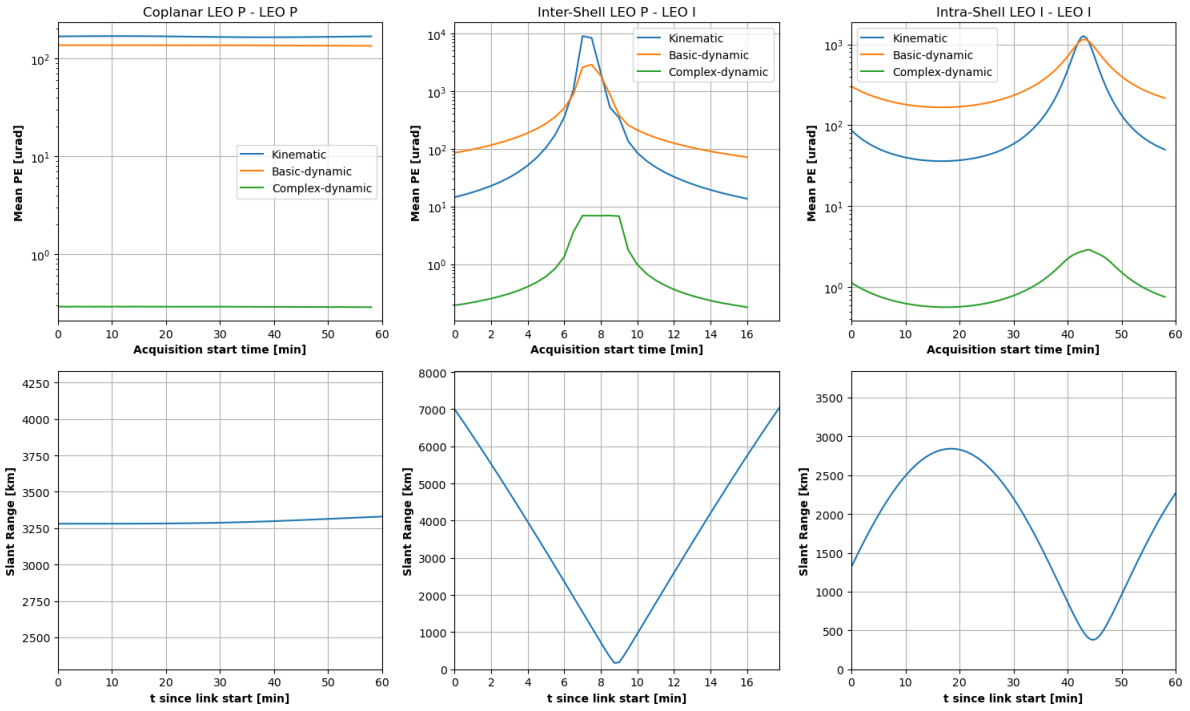

Figure 5.7: Mean PE for each OD-OP algorithm, evaluated at different prediction start times throughout the link availability window.

One surprising outcome to note is that the Kinematic OD-OP algorithm outperforms the Basic-dynamic option for multiple link-cases in these short-term predictions. This is true for the MEO-MEO and most of the Inter-shell LEO P - LEO I and intra-shell LEO I - LEO I links. This is counter-intuitive, as both the OD and the OP induced position errors are higher for the Kinematic algorithm, compared

to the basic-dynamic option. This indicates that the PE depends on more than just the norm of the position errors.

Looking deeper, the PE at multiple starting link distances, the host/target predicted position errors and the separate components of the predicted LOS errors are shown for the LEO P - LEO I link case in Figure 5.8. The PE can be seen at the early link start times, around 4 minutes with link distances at about 4000 km, where the basic dynamic algorithm outperforms the KA and close to the mid-link time, where the KA does better. Observing the host and target position errors, in the middle column, it can be seen that the kinematic option leads to equally poor predictions with errors above 1 km, whereas the basic-dynamic option leads to better predictions, with final errors at about 0.2 and 0.4 km. Interestingly, the host and target orbit prediction errors are different in the BDA and this is due to the initial errors also having a relatively large offset of about 10 m.

Observing the impact on the LOS error RSW components in the right column, it can be seen that outside of the radial LOS error component, they are larger for the KA. The behaviour of the predicted LOS RSW error components can provide some insight as to why the KA can lead to lower PE than BDA while having larger overall position errors. By far the larger error component for the KA is the along-track component. This component, depending on the link geometry can have the smallest impact on the LOS error component perpendicular to the true LOS. This perpendicular component directly leads to the PE contribution, so while the LOS error does grows in a direction that is more parallel to the true LOS, the direct PE contribution will be smaller than if the LOS error grows more in the perpendicular direction. In case of the BDA, all 3 components grow at similar rates, which is consistent with the its PE behaviour over all link cases, as its quite predictable and only increases with smaller link distances. In contrast, for the KA, this was not always the case, as in the more complex link geometries (MEO - LEO I, LEO P - MEO), the PE at times decreased for decreasing link distances. Therefore, due to the uneven increase in the predicted LOS RSW errors, the KA can outperform the BDA in short-term predictions in the case that the true LOS is mostly aligned with the along-track direction.

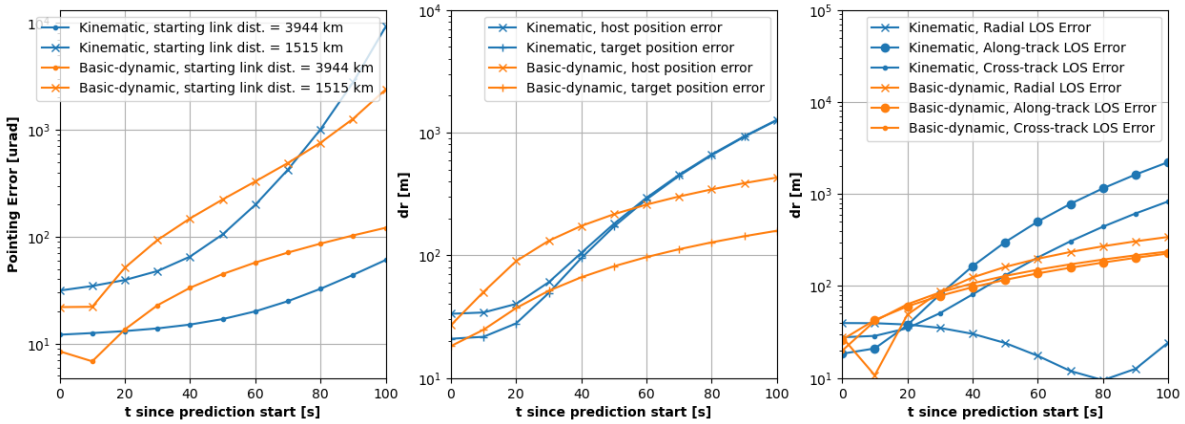

Figure 5.8: PE, host/target predicted position errors and the RSW errors components of the predicted LOS for the Kinematic and Basic-Dynamic algorithms in the Inter-shell LEO P-LEO I link case.

5.2.2. Longer Prediction Windows

Now the algorithms have been evaluated for acquisition window prediction lengths, it is also critical to analyze how the algorithms perform for longer prediction windows. In section 3.5, it was concluded that 10, 30 and 60 minute prediction windows are most critical when considering all possible communication window lengths. Thus, the PE contributions at these times will be looked into.

To do so, 100 samples of IC errors were taken for the host/target satellites and the resulting 3-sigma maximum PE was shown for each prediction window, link case and OD-OP algorithm. The results can be seen in Table 5.2. The Algorithm performance in the link cases involving MEO satellites are shown in the upper half, while strictly LEO link cases are shown in the bottom half of the table.

The CDA stands out as providing extremely precise coarse pointing knowledge in each link case. Even for 1 hour predictions, the maximum PE contribution remains below 50 urad for LEO and MEO link cases. Thus it can be concluded that the CDA algorithm can provide accurate enough coarse pointing knowledge and that its contributions will not exceed 50 urad in any link cases of the analyzed

LEO/MEO constellation, with the condition that the initial solution is of the precision quantified in the previous chapter.

In contrast, the BDA and KA lead to much higher PE contributions and only in limited cases provide precise enough LOS predictions for 10+ minute communication windows. Analyzing the upper half of the table, the KA and BDA can still provide sufficiently accurate coarse pointing knowledge, not exceeding 0.5 mrad for the MEO - MEO link. For the inter-orbit links, the KA has much higher PE contributions and this can be linked to the link geometry no longer being aligned with the along-track orbital direction, as was discussed in subsection 5.2.1. The BDA, in contrast, can support all of the MEO links, with the PE remaining below 0.5 mrad for 10 minute prediction windows. However, for the longer prediction windows of 30+ minutes, the PE contributions exceed 0.5 mrad and thus the coarse pointing knowledge is not sufficiently precise. Therefore, the KA can only reliably provide the coarse pointing knowledge to co-planar MEO links, whereas the BDA supports all MEO and MEO/LEO links for 10 minute prediction windows.

The situation for the BDA and KA becomes more grim when their performance for LEO links is observed in the bottom half of Table 5.2. The BDA provides coarse pointing knowledge with errors exceeding the required threshold by a factor of 5 in co-planar LEO P and cross-plane LEO I links in 10 minute prediction windows. In longer prediction windows, the errors already exceed the threshold by 1 order of magnitude or more. The KA leads to maximum errors at least 1 order of magnitude higher than the required threshold. Therefore, neither the KA, nor the BDA can reliably be used for links at LEO satellite link distances.

Table 5.2: 99.7th percentile of the maximum PE [urad] for the 10/30/60 min. predictions.

t pred.	**Copl. MEO - MEO**			**Inter-orb. MEO - LEO I**			**Inter-orb. LEO P - MEO**		
[min]	**KA**	**BDA**	**CDA**	**KA**	**BDA**	**CDA**	**KA**	**BDA**	**CDA**
10	400	300	0.2	7500	400	0.2	5400	400	0.2
30	9700	900	0.4	148100	2000	1.1	400500	1900	1.1
60	64000	1800	0.9	2153500	2500	1.2	1457400	3700	1.2
t pred.	**Copl. LEO P - LEO P**			**Inter-shell LEO P - LEO I**			**Intra-shell LEO I - LEO I**		
[min]	**KA**	**BDA**	**CDA**	**KA**	**BDA**	**CDA**	**KA**	**BDA**	**CDA**
10	31600	2200	1.2	1590800	43300	21.3	5100	2800	3
30	154200	7800	3.1	1590800	43300	21.3	24100	15500	6.3
60	1038300	14500	4.6	-	-	-	2330800	127900	39.9

The time behaviour of the PE for each algorithm/link case is visualized in Figure 5.9. This provides insight into how the PE behavior for the different algorithms and shows whether the resulting PE can still remain below the threshold depending on the IC errors.

As was seen in the tabulated outcomes, the CDA remains well below the PE threshold for the 60 minute prediction window in every case. The same can be seen in the plot, as none of the IC error samples lead to PE growth above 50 urad.

Comparing the KA and the BDA, several points can be made regarding the PE behaviour and the overall algorithm performance. Firstly, the KA can again be seen to outperform the BDA in the early stages of the LOS predictions, which was already discussed in subsection 5.2.1 and in general can only occur for short predictions when the true LOS is mostly in the along-track orbital direction. Another point is that the KA PE growth well exceeds the BDA PE for any longer prediction time, which is due to the extrapolator's poor ability to predict an orbit and once the LOS geometry changes, the prediction quality decreases dramatically. In fact, the KA can be seen to lead to equally large PE in all of the IC errors, which shows that the dominant PE contribution comes from the orbit prediction error growth and is far less dependent on the quality of the initial OD. The BDA performs differently compared to the KA in terms of the PE growth. The BDA performance strongly depends on the IC error. It can be seen that PE is spread out among the IC error samples, which shows that the BDA generally predicts the orbit much better than the KA, but the prediction quality decreases steadily for larger IC errors.

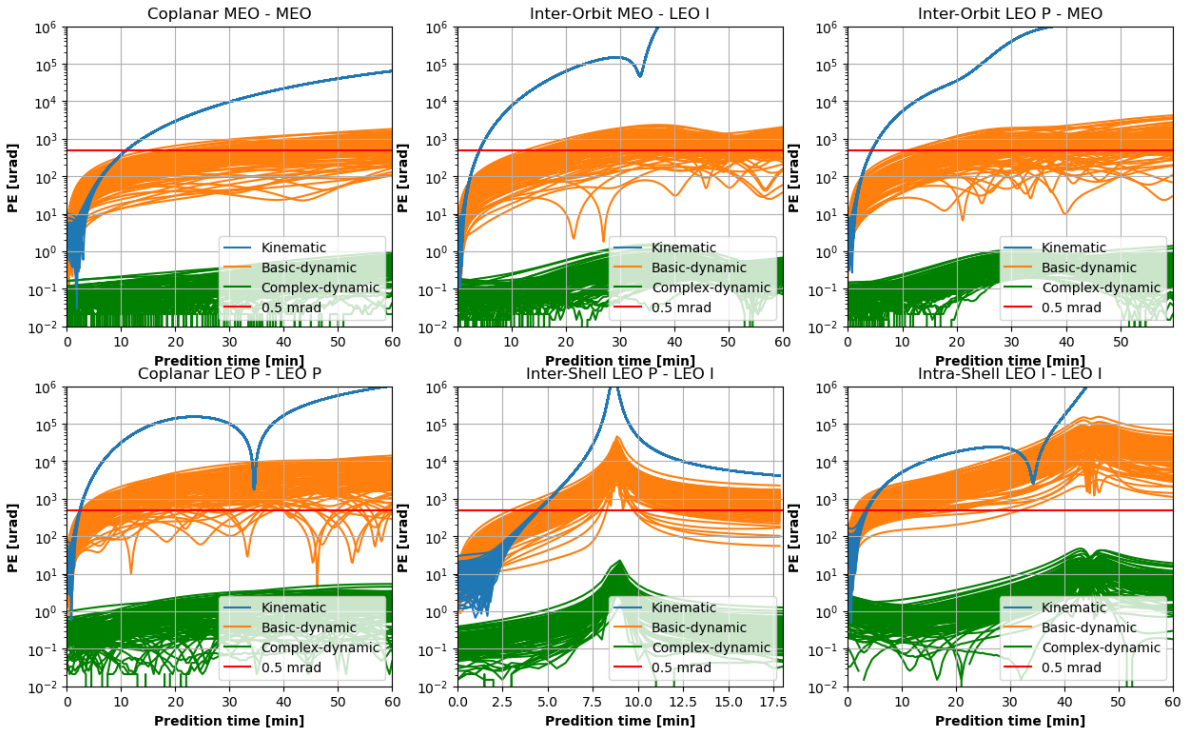

Figure 5.9: Pointing Errors growth for LOS predictions for 100 samples of IC errors for each OD-OP algorithm and link case, also showing the maximum allowed PE threshold.

Looking into the PE growth with respect to the 0.5 mrad threshold, the results in Figure 5.9 are a lot more positive for the BDA than what Table 5.2 indicated. Looking at the LEO link cases, the PE remains below 0.5 mrad for many of the IC error samples even at longer prediction windows. In the co-planar LEO P - LEO P case at the bottom left of Figure 5.9, up to 10 minutes of predictions, many of the IC error samples lead to PE still below the threshold. This is also true for the Intra-shell LEO I - LEO I link case. However, most of the PE are still above the threshold and thus the conclusion the algorithm cannot reliably provide precise enough coarse pointing knowledge remains valid.

5.3. OD-OP in LISL Conclusions

In this section, the conclusions relating to the originally formulated RQ3 will be summarized. As in the previous chapters, his is done to each sub-question, leading to an overall answer to the central research question regarding the expected OD-OP method performance in satellite laser communications.

3 a) *What is the PE contribution for increasingly complex integrated OD-OP algorithms in the LEO/MEO constellation during the critical communication windows?*

The PE contributions were consistently much larger for PR-based KA and BDA than the CP-based CDA. The CDA lead to a maximum 40 urad PE contribution in the 60 min window for intra-shell LEO I - LEO I links, whereas all other communication windows are link cases showed negligible error contributions below 6.5 urad.

The KA could only support co-planar MEO links for 10 minutes, with PE contributions of 0.4 mrad. The KA lead to PE contributions above 5 mrad for all other link at the 10 minute window. For any longer prediction windows, the performance degraded rapidly due to the quadratic-extrapolation based predictions poorly representing the true orbits.

The BDA could support all link cases involving MEO satellites for the 10 minute window and had about 5-10 times too large PE contributions in 10 minute LEO links. For the co-planar MEO links, the PE contributions were 0.3, 0.9 and 1.8 mrad for the 10, 30 and 60 minute prediction windows, respectively. In MEO-LEO I and LEO P - MEO links, the respective errors were 0.4 mrad for 10 minutes and 2+ mrad for 30 and 60 minute windows. In contrast, in LEO links, the 10 minute prediction PE contributions were 2.2 mrad for co-planar LEO P links and 2.8 mrad for intra-shell LEO I - LEO I links.

3 b) *What is the PE contribution for each OD-OP algorithm for the 100 second link-acquisition window throughout the available link communication window?*

The acquisition window PE contributions varied strongly between the OD-OP algorithms and appeared to be very dependent on the link geometry for the KA. While the CDA was consistently precise, never exceeded 10 urad contributions and only showed a slight dependency on the link distance, the BDA and KA performance were less intuitive. The BDA and KA lead to less than 100 urad PE contributions in MEO link cases, whereas LEO links lead to errors above 1000 urad during the close approaches.

Depending on the link case and link geometry, the KA sometimes outperformed the more complex BDA in these short-window predictions. In co-planar MEO cases, the KA was consistently better, leading to less than 10 urad PE contributions, whereas the BDA showed about 15 urad contributions. In MEO - LEO I links, the KA showed errors between 20 and 100 urad, whereas the LEO P - MEO case lead to 5-100 urad errors. In contrast, the BDA was more consistent, with errors between 20 and 30 urad for MEO - LEO I and LEO P - MEO. In co-planar LEO cases, both KA and BDA were at 150-170 urad PE contributions. In the LEO P - LEO I, BDA lead to 100-2000 urad PE contributions and KA to 15-10000 urad. Finally, in the intra-shell LEO I - LEO I link case, the KA showed error contributions in the 60-1000 urad and the BDA was consistently worse with 200-1000 urad contributions.

3 c) *How long can each integrated OD-OP algorithm support each type of link LISL without exceeding the maximum allowed PE contribution threshold?*

Considering the 0.5 mrad PE threshold, the KA could support MEO - MEO links up to 10 minutes, and MEO - LEO links up to 5 minutes. In LEO link cases, the KA PE contribution was below the threshold for 2-4 minutes and increased rapidly after 5 minutes.

The BDA showed a wider spread in performance as its OP quality was more dependent on the IC errors. In all MEO link cases, the 0.5 mrad threshold was crossed at 15 minutes but in some cases did not exceed 100 urad after 60 minutes. Its dependency on IC errors was also seen in LEO links. However, the PE contributions were reliably good enough for only about 2-4 minutes in each link case, as was the case for the KA. What differed was that the errors did not increase as rapidly as for the KA, which indicates that with some modifications, the BDA could potentially support longer links.

6

Conclusion and Recommendations

6.1. Conclusions

Analyzing the link availability in the LEO/MEO constellation for LCT's fitting CONDOR Mk2 and Mk3 limitations, it was found that LCT2 could consistently cover more and longer duration links. This was due to its longer longer maximum link range and wider range of covered elevation angles.

Regarding the communication windows, it was concluded that 10, 30 and 60 minute windows will be the most relevant considering the available link distribution for both terminals. A 10 minute window was found to cover over 50% of all LEO link cases for the Mk2, while the 30 minute window covered over 90% of all Mk2 link cases and most of LEO link cases for the Mk3. The 60 minute window was deemed necessary to cover the remaining link cases involving MEO satellites.

Testing GNSS-OD methods, several conclusions could be made. Firstly, the filter performance did not improve consistently for any filter when switching from theoretical to tuned KF settings. Using CHAMP data, the PEKF errors increased by 10%, EKF improved by about 30% SPUKF errors decreased by about 5% and the UKF performance was 30% worse. For the other used datasets, the results were also inconsistent, showing that the filter parameters were most likely not the reason for the filters' performance issues.

Testing the Improved-PEKF which uses a new Numerical root method showed no improvement in PEKF performance. The filter performed identically in terms of accuracy and required either the same or more computations to come to its conclusion. It was determined that this was due to the N-dimensional Newton-Raphson Predictor-Corrector numerical method performance. Although theoretically it was found to be more efficient than the classic NRM, when applied to GNSS-OD, it showed no improvement. It was thus concluded that the Improved-PEKF lead to no benefits compared to the original PEKF formulation.

EKF, PEKF, UKF and SPUKF were all implemented using SF pseudoranges and tested with GRACE-FO, CHAMP and Jason-3 flight data. In general, the novel filters did not appear promising over their classic formulation counterparts. PEKF performed similarly or worse than the EKF and the same applied for SPUKF compared to the UKF. It was concluded that in most cases, the best PR-KF options were EKF and UKF in terms of accuracy - with 3D RMS errors of about 60 m for CHAMP data, 8 m for GRACE-FO and 50 m for Jason-3. The novel filter performance indicated higher errors for CHAMP - 100; 140 m for CHAMP, mixed results for GRACE-FO: 23; 8 m and slightly improved results for Jason-3 - 47; 43.1 m 3D RMS errors for the PEKF and SPUKF, respectively. Considering the implementation and real-time application needs for the algorithms- the standard EKF was found optimal, as it generally had low errors, the smallest computational load and was the least complex to implement, test and tune.

After analyzing the link cases and the prediction window lengths, the Kinematic, Basic-Dynamic and Complex-Dynamic algorithms were benchmarked in terms of their PE contributions. It was found that during acquisition window predictions, all 3 algorithms could provide sufficiently accurate LOS predictions. However, with longer prediction windows, only the CDA was consistently below the PE threshold.

This showed that there are indeed link conditions where only the most precise OD-OP algorithms provide accurate enough CPA knowledge. That is true when the link distance falls below 1500 km in the LEO P - LEO I or LEO I - LEO I link cases. This is to be expected, as the PE is more sensitive to host/target predicted position errors as link distances shorten. Another conclusion to draw is that the kinematic and basic-dynamic ODOP algorithms do provide sufficiently accurate coarse pointing knowledge while the link distances are generally larger- above 2500 km. The PE contributions at these distances are below 0.5 mrad which could still be sufficiently small for the PE budget in link acquisition.

It was also found that the KA at times outperformed the BDA, especially during the shorter acquisition windows and when the LOS was found to be lined up with the orbital motion direction. This showed that PE not only depends on host/target position errors but the resulting predicted LOS error component behaviour and their relative geometry to the link direction. As the extrapolation LOS prediction error grows fastest along-track, in cases where the link geometry was favourable, its poor orbit predictions still resulted in relatively good LOS.

CP-based complex dynamic OD-OP algorithm provides sufficiently precise LOS predictions for every analyzed link case and prediction window. Even at 1 hour predictions, the maximum PE did not exceed 50 urad. Thus it can reliably provide coarse pointing knowledge for any of the analyzed link cases and prediction windows, as long as the OD errors remain in the expected ranges.

The Kinematic algorithm could only provide precise enough LOS predictions in MEO-MEO links for 10 minute prediction windows, having a PE contribution of less than 0.5 mrad. In all other analyzed link cases, the maximum PE exceeded the 0.5 mrad threshold by at least 1 order of magnitude. Therefore, in almost all link cases, the KA does not provide accurate enough coarse pointing knowledge for 10+ minute link windows.

The BDA did provide sufficiently precise LOS predictions in all MEO link cases when looking at 10 minute prediction windows. However, the PE exceeded the threshold in all other cases, with maximum PE reaching at least 1 mrad for longer predictions. In LEO link cases, the BDA again lead to maximum PE above the threshold, with even 10 minute LOS predictions having maximum PE above 2 mrad in the basic coplanar LEO-LEO link case. Therefore, the BDA can only reliably provide 10+ minute coarse pointing knowledge in MEO satellite link cases.

6.2. Future Recommendations

- For the implemented GNSS-OD algorithms, the GNSS observation techniques were potentially the biggest bottlenecks in the OD performance. A more advanced measurement selection technique, which consider Signal-Noise-Ratio, GPS satellite elevation and Geometric Dilution of Precision could lead to better results.
- Only pseudorange-based models were implemented during this research, it is recommended to also implement a carrier-phase based OD algorithm to test whether its performance is in-line with the expectations in literature. The benefit of having the analyzed CDA for OD-OP is immense, as very long-term predictions could be made with minimal PE contributions.
- When implementing CP-based OD algorithms, a necessity would be to robustly determine the quality of the current solution. Knowing whether the filter is currently performing nominally could be utilized to predict a precise orbit for an hour without the need for re-computation. But this would not be the case if a poor-quality solution was used for the orbit prediction.
- Adaptive Kalman Filters could also potentially provide benefits by removing the tuning requirements for the filters and responding to clusters of lower quality observations without much added complexity.
- DF measurements could also provide an improvement in the OD quality. Although DF are costlier, their benefits can be quantified in these use cases.
- The OD-OP algorithms can be further broken down to analyze the possible simplifications of the used ICRF-ITRF rotation models, numerical instigators and satellite state representations.
- The OD-OP algorithms had a major discrepancy in the initial OD, which could lead to the main factor in large OP errors for the BDA. It could be looked into if the CP-based OD methods could be better interfaced with a basic propagator to save on computational load, while still providing sufficient LOS prediction accuracy.
- Off-line ephemeris generation methods could potentially provide sufficiently accurate Line of Sight predictions by making orbit predictions based on accumulated tracking data.

References

[1] Physical Oceanography Distributed Active Archive Center (PODAAC). *GRACE-FO level-1b data, GRACEFO_L1B_ASCII_GRAV_JPL_RL04. Ver. 4*. Dataset accessed: 2022-04-11. 2019. URL: https://doi.org/10.5067/GFL1B-ASJ04.

[2] Accord. *ACC-GPS-NANO-NR*. 2022. URL: https://satsearch.co/products/accord-software-systems-acc-gps-nano-nr (visited on 11/16/2022).

[3] Murat Bagci and Chingiz Hajiyev. "Comparison of linear and nonlinear measurements based orbit estimation EKFs". In: Institute of Electrical and Electronics Engineers Inc., Aug. 2017, pp. 433–438. ISBN: 9781538616031. DOI: 10.1109/RAST.2017.8002999.

[4] Murat Bagci and Chingiz Hajiyev. "Integrated NRM/EKF for LEO satellite GPS based orbit determination". In: Institute of Electrical and Electronics Engineers Inc., Sept. 2016, pp. 462–467. ISBN: 9781467382922. DOI: 10.1109/MetroAeroSpace.2016.7573259.

[5] Sanat K Biswas et al. "Application of a Fast Unscented Kalman Filtering Method to Satellite Position Estimation using a Space-borne Multi-GNSS Receiver". In: 2015. URL: https://www.researchgate.net/publication/281725291.

[6] Dirk Brouwer. "Solution of the problem of artificial satellite theory without drag". In: *The Astronomical Journal* 64 (Nov. 1959), p. 378. ISSN: 00046256. DOI: 10.1086/107958.

[7] Dirk Brouwer and Gen-Ichiro Hori. "Theoretical evaluation of atmospheric drag effects in the motion of an artificial satellite". In: *The Astronomical Journal* 66 (June 1961), p. 193. ISSN: 00046256. DOI: 10.1086/108399.

[8] Alberto Carrasco-Casado et al. "LEO-to-Ground Optical Communications using SOTA (Small Optical TrAnsponder)–Payload Verification Results and Experiments on Space Quantum Communications". In: *Acta Astronautica* 139 (2017), pp. 377–384.

[9] Eun Jung Choi et al. "Onboard orbit determination using GPS observations based on the unscented Kalman filter". In: *Advances in Space Research* 46 (11 Dec. 2010), pp. 1440–1450. ISSN: 02731177. DOI: 10.1016/j.asr.2010.07.022.

[10] John L Crassidis and John L Junkins. *Optimal Estimation of Dynamic Systems*. CRC Press LLC, 2011, pp. 185–190. ISBN: 9781439839867. URL: http://ebookcentral.proquest.com/lib/delft/detail.action?docID=800953.

[11] Elecnor Deimos. *G3STAR GNSS Receiver or New Space*. 2022. URL: https://elecnor-deimos.com/wp-content/uploads/2022/02/AF01-Digital_DEIMOS_GN_Product-G3Star-1.pdf (visited on 11/16/2022).

[12] Ines Gaudel. "Operational Use of SILEX Optical Laser Link between SPOT4 and ARTEMIS Satellites". In: American Institute of Aeronautics and Astronautics (AIAA), May 2004. DOI: 10.2514/6.2004-480-279.

[13] Dirk Giggenbach et al. "Downlink communication experiments with OSIRISv1 laser terminal onboard Flying Laptop satellite." In: *Applied optics* 61.8 (Mar. 3, 2022), pp. 1938–. DOI: 10.1364/ao.446771. URL: https://lens.org/117-066-831-099-756.

[14] Eberhard Gill et al. "High-precision onboard orbit determination for small satellites-The GPS-based XNS on X-SAT Optimal Data Fusion for Relative Pose Estimation for Uncooperative Targets View project Joint Orbit and Attitud Relative Spacecraft Orbit and Attitude View project". In: 2004, pp. 47–52. URL: https://www.researchgate.net/publication/234269518.

[15] Xuewen Gong et al. "Precise onboard real-time orbit determination with a low-cost single-frequency GPS/BDS receiver". In: *Remote Sensing* 11 (11 June 2019). ISSN: 20724292. DOI: 10.3390/rs11111391.

[16] Vlad Grigore. “Unscented Kalman Filters for Attitude and Orbit Estimation of a Low Earth Orbit CubeSat”. Royal Institute of Technology, Jan. 2014.

[17] Roger C Hart et al. “Global Positioning System (GPS) Enhanced Orbit Determination Experiment (GEODE) on the Small Satellite Technology Initiative (SSTI) Lewis Spacecraft”. In: 1996, pp. 1303–1312.

[18] André Hauschild and Oliver Montenbruck. “Precise real-time navigation of LEO satellites using GNSS broadcast ephemerides”. In: *Navigation, Journal of the Institute of Navigation* 68 (2 June 2021), pp. 419–432. ISSN: 00281522. DOI: 10.1002/navi.416.

[19] F. Heine et al. “Optical inter-satellite communication operational”. In: 2010, pp. 1583–1587. ISBN: 9781424481804. DOI: 10.1109/MILCOM.2010.5680175.

[20] Hamid Hemmati. *Near-Earth Laser Communications*. 2009, pp. 1–403. ISBN: 9780824753818.

[21] B Hofmann-Wellenhof, Herbert Lichtenegger, and James Collins. *Global positioning system : theory and practice*. 2001.

[22] https://docs.tudat.space/en/latest/#. *TUDAT Space documentation*. 2023. URL: https://docs.tudat.space/en/latest/%5C# (visited on 01/01/2023).

[23] https://mynaric.com/news. *Mynaric announces another customer for recently released CONDOR Mk3*. 2021. URL: https://mynaric.com/news/mynaric-announces-another-customer-for-recently-released-condor-mk3/ (visited on 05/09/2022).

[24] https://mynaric.com/products. *CONDOR Mk2*. 2022. URL: https://mynaric.com/products/space/condor-mk2/ (visited on 05/09/2022).

[25] https://mynaric.com/products. *CONDOR Mk3*. 2022. URL: https://mynaric.com/products/space/condor-mk3/ (visited on 05/09/2022).

[26] *Jason-3 Products Handbook*. 2018.

[27] Takashi Jono et al. “Overview of the inter-orbit and the orbit-to-ground laser communication demonstration by OICETS”. In: vol. 6457. SPIE, Feb. 2007, p. 645702. ISBN: 0819465739. DOI: 10.1117/12.708864.

[28] Simon J. Julier and Jeffrey K. Uhlmann. “New extension of the Kalman filter to nonlinear systems”. In: vol. 3068. SPIE, July 1997, p. 182. ISBN: 0819424838. DOI: 10.1117/12.280797.

[29] Dah-Jing Jwo and Chun-Nan Lai. “Unscented Kalman filter with nonlinear dynamic process modeling for GPS navigation”. In: *GPS Solutions* 12 (Sept. 2008), pp. 249–260. DOI: 10.1007/s10291-007-0081-9.

[30] Elliott Kaplan and Christopher Hegarty. *Understanding GPS Principles and Applications Second Edition*. 2006.

[31] Sien-Chong Wu Kelley Case Gerhard Kruizinga. *GRACE Level 1B Data Product User Handbook*. 2010.

[32] H. Kunimori et al. “Down link optical communication experiment using micro satellite body pointing and collaboration with co-located science instrument”. In: 4 (Jan. 2013), pp. 3132–3136.

[33] Alfredo Locarini. “Design, development and testing of a GPS-based navigation sub-system for microsatellites missions”. PhD thesis. University of Bologna, 2018.

[34] Amandeep Mander and Sunil Bisnath. “GPS-based precise orbit determination of Low Earth Orbiters with limited resources”. In: *GPS Solutions* 17 (4 Oct. 2013), pp. 587–594. ISSN: 10805370. DOI: 10.1007/s10291-012-0303-7.

[35] M Markgraf et al. “Phoenix-XNS navigation system onboard the PROBA-2 spacecraft-first flight results”. In: 2010, pp. 60–68.

[36] Oliver Montenbruck and Eberhard Gill. *Satellite Orbits: Models, Methods and Applications*. 2000. URL: http://www.springende/phys/.

[37] Oliver Montenbruck and Remco Kroes. “In-flight performance analysis of the CHAMP BlackJack GPS Receiver”. In: *GPS Solutions* 7 (2 Aug. 2003), pp. 74–86. ISSN: 15211886. DOI: 10.1007/s10291-003-0055-5.

[38] Oliver Montenbruck and Pere Ramos-Bosch. “Precision real-time navigation of LEO satellites using global positioning system measurements”. In: *GPS Solutions* 12 (3 July 2008), pp. 187–198. ISSN: 10805370. DOI: 10.1007/s10291-007-0080-x.

[39] Oliver Montenbruck et al. “Autonomous and Precise Navigation of the PROBA-2 Spacecraft”. In: 2008, pp. 7086–7103.

[40] Oliver Montenbruck et al. “GPS orbit determination for micro-satellites - The PROBA-2 flight experience”. In: 2010. ISBN: 9781624101502. DOI: 10.2514/6.2010-8261.

[41] S. Müncheberg et al. “Development status and breadboard results of a laser communication terminal for large LEO constellations”. In: SPIE-Intl Soc Optical Eng, July 2019, p. 111. ISBN: 9781510630772. DOI: 10.1117/12.2536031.

[42] Daniel V. Murphy et al. “LLCD operations using the Lunar Lasercom Ground Terminal”. In: *Free-Space Laser Communication and Atmospheric Propagation XXVI*. Ed. by Hamid Hemmati and Don M. Boroson. Vol. 8971. International Society for Optics and Photonics. SPIE, 2014, pp. 250–256. DOI: 10.1117/12.2045509. URL: https://doi.org/10.1117/12.2045509.

[43] Mynaric. *The Technology Behind Laser Communication*. 2020. URL: https://mynaric.com/technology/overview/ (visited on 09/09/2022).

[44] Clement A Ogaja. *Introduction to GNSS Geodesy Foundations of Precise Positioning Using Global Navigation Satellite Systems*. Springer Nature Switzerland AG, 2022. ISBN: 978-3-030-91820-0. DOI: https://doi.org/10.1007/978-3-030-91821-7.

[45] OneWeb. *ONEWEB NON-GEOSTATIONARY SATELLITE SYSTEM (LEO) PHASE 2: AMENDED MODIFICATION TO AUTHORIZED SYSTEM*. http://licensing.fcc.gov/myibfs/forwardtopublictabaction.do?filenumber=SATMPL2021011200007. Technical Appendix. Accessed: 2022-05-27. 2021.

[46] M R Pearlman, J J Degnan, and J M Bosworth. “THE INTERNATIONAL LASER RANGING SERVICE ORIGIN AND ESTABLISHMENT OF THE ILRS”. In: *Adv. Space Res* 30 (2 2002), pp. 135–143. URL: www.elsevier.com/locatelasr.

[47] Hao Peng and Xiaoli Bai. “Exploring capability of support vector machine for improving satellite orbit prediction accuracy”. In: *Journal of Aerospace Information Systems* 15 (6 2018), pp. 366–381. ISSN: 23273097. DOI: 10.2514/1.I010616.

[48] Hao Peng and Xiaoli Bai. “Machine Learning Approach to Improve Satellite Orbit Prediction Accuracy Using Publicly Available Data”. In: *Journal of the Astronautical Sciences* 67 (2 June 2020), pp. 762–793. ISSN: 21950571. DOI: 10.1007/s40295-019-00158-3.

[49] J. M. Perdigues et al. “The ESA’s optical ground station for the EDRS-A LCT in-orbit test campaign: upgrades and test results”. In: SPIE-Intl Soc Optical Eng, Sept. 2017, p. 79. ISBN: 9781510616134. DOI: 10.1117/12.2296098.

[50] E. Perez, M. Bailly, and J. M. Pairot. “Pointing Acquisition And Tracking System For Silex Inter Satellite Optical Link”. In: vol. 1111. SPIE, Sept. 1989, p. 277. DOI: 10.1117/12.977988.

[51] Paula Cristiane Pinto et al. “Unscented Kalman FIlter Robustness Assessment for Orbit Determination Using GPS Signals”. In: *Advances in the Astronautical Sciences* 13 (2013). URL: https://www.researchgate.net/publication/261831579.

[52] Alexandru F. Popescu and Bernhard Furch. “Status of the European developments for laser intersatellite communications”. In: vol. 1866. SPIE, Aug. 1993, p. 10. ISBN: 0819410934. DOI: 10.1117/12.149239.

[53] Koenig Rolf et al. *GFZ CHAMP Rapid Science Orbits (version 1)., GFZ Data Services*. 2022.

[54] T. S. Rose et al. “Optical communications downlink from a low-earth orbiting 1.5U CubeSat”. In: *Optics Express* 27 (17 Aug. 2019), p. 24382. ISSN: 10944087. DOI: 10.1364/oe.27.024382.

[55] Nor asnilawati Salleh et al. “Enhancing simplified general perturbations-4 model for orbit propagation using deep learning: A review”. In: vol. Part F147956. Association for Computing Machinery, 2019, pp. 27–32. ISBN: 9781450365734. DOI: 10.1145/3316615.3316675.

[56] Paul C. Serra et al. “CubeSat laser infrared crosslinK mission status”. In: SPIE-Intl Soc Optical Eng, June 2021, p. 119. DOI: 10.1117/12.2599543.

[57] Simon P Shuster. “A Survey and Performance Analysis of Orbit Propagators for LEO, GEO and Highly Elliptical Orbit”. Master Thesis. Utah State University, 2017. URL: https://digitalcommons.usu.edu/etd/6510.

[58] Zoran Sodnik et al. “Optical satellite communications in Europe”. In: vol. 7587. SPIE, Feb. 2010, p. 758705. ISBN: 9780819479839. DOI: 10.1117/12.847075.

[59] Spacemanic. *Celeste - the GNSS Receiver*. 2022. URL: https://satsearch.co/products/spacemanic-celeste-the-gnss-receiver (visited on 11/16/2022).

[60] Spacex. *SPACEX NON-GEOSTATIONARY SATELLITE SYSTEM*. http://licensing.fcc.gov/myibfs/forwardtopublictabaction.do?filenumber=SESLIC2020102301173. Technical Appendix. Accessed: 2022-05-27. 2020.

[61] Xiucong Sun, Chao Han, and Pei Chen. “Real-time precise orbit determination of LEO satellites using a single-frequency GPS receiver: Preliminary results of Chinese SJ-9A satellite”. In: *Advances in Space Research* 60 (7 Oct. 2017), pp. 1478–1487. ISSN: 0273-1177. DOI: 10.1016/J.ASR.2017.06.052.

[62] D Svehla and M Rothacher. “Advances in Geosciences Kinematic and reduced-dynamic precise orbit determination of low earth orbiters”. In: 1 (June 2003), pp. 47–56. DOI: DOI:10.5194/adgeo-1-47-2003.

[63] Kuiper Systems. *Application of Kuiper Systems LLC for Authority to Launch and Operate a Non-Geostationary Satellite Orbit System in Ka-band Frequencies*. http://licensing.fcc.gov/myibfs/forwardtopublictabaction.do?filenumber=SATLOA2019070400057. Technical Appendix. Accessed: 2022-05-27. 2019.

[64] NewSpace Systems. *NSS GPS Receiver*. 2022. URL: https://www.cubesatshop.com/product/nss-gps-receiver/ (visited on 11/16/2022).

[65] Telesat. *Telesat Low Earth Orbit Non-Geostationary Satellite System*. http://licensing.fcc.gov/myibfs/forwardtopublictabaction.do?filenumber=SATMPL2020052600053. Technical Appendix. Accessed: 2022-05-27. 2020.

[66] Peter J.G. Teunissen and Oliver Montenbruck. *Springer Handbook of Global Navigation Satellite Systems*. 1st ed. 2017. ISBN: 978-3-319-42928-1. DOI: https://doi-org.tudelft.idm.oclc.org/10.1007/978-3-319-42928-1.

[67] Marcos Tostado, Salah Kamel, and Francisco Jurado. “Developed Newton-Raphson based Predictor-Corrector load flow approach with high convergence rate”. In: *International Journal of Electrical Power and Energy Systems* 105 (Feb. 2019), pp. 785–792. ISSN: 01420615. DOI: 10.1016/j.ijepes.2018.09.021.

[68] David A. Vallado, Wayne D. McClain, and Mahooti Meysam. *Fundamentals of Astrodynamics and Applications*. Fourth. Microcosm Press, 2013.

[69] Parkinson Bradford W. et al. *Single-Frequency Precise Orbit Determination*. American Institute of Aeronautics and Astronautics (AIAA), 1996, pp. 580–583. ISBN: 978-1-56347-107-0. URL: https://app.knovel.com/hotlink/khtml/id:kt00C9M7P2/global-positioning-system/single-frequency-precise.

[70] E. A. Wan and R. Van Der Merwe. “The unscented Kalman filter for nonlinear estimation”. In: Institute of Electrical and Electronics Engineers Inc., 2000, pp. 153–158. ISBN: 0780358007. DOI: 10.1109/ASSPCC.2000.882463.

[71] Fuhong Wang et al. “A novel method for precise onboard real-time orbit determination with a standalone GPS receiver”. In: *Sensors (Switzerland)* 15 (12 Dec. 2015), pp. 30403–30418. ISSN: 14248220. DOI: 10.3390/s151229805.

[72] Zhiyu Wang et al. “Comparison of the real-time precise orbit determination for LEO between kinematic and reduced-dynamic modes”. In: *Measurement: Journal of the International Measurement Confederation* 187 (Jan. 2022). ISSN: 02632241. DOI: 10.1016/j.measurement.2021.110224.

[73] James Richard Wertz. *Orbit Design and Constellation Management*. Vol. 13. 2001.

[74] Pascal Willis et al. “The International DORIS Service (IDS): Toward maturity”. In: *Advances in Space Research* 45 (12 June 2010), pp. 1408–1420. ISSN: 02731177. DOI: 10.1016/j.asr.2009.11.018.

[75] Sien-Chong Wu, Gerhard Kruizinga, and Willy Bertiger. *Algorithm Theoretical Basis Document for GRACE Level-1B Data Processing V1.2*. 2006.

[76] Jing Yi Zhang et al. “Inter-satellite laser link acquisition with dual-way scanning for Space Advanced Gravity Measurements mission”. In: *Review of Scientific Instruments* 89 (6 June 2018). ISSN: 10897623. DOI: 10.1063/1.5019433.